SURFACE-INITIATED POLYMETHYLENATION TO GROW SUPERHYDROPHOBIC BARRIER FILMS

By

Juan Carlos Tuberquia

Dissertation

Submitted to the Faculty of the

Graduate School of Vanderbilt University

In partial fulfillment of the requirements

for the degree of

DOCTOR OF PHILOSOPHY

in

Chemical Engineering

August, 2011

Nashville, Tennessee

Approved:

Professor G. Kane Jennings

Professor Paul E. Laibinis

Professor Eugene LeBoeuf

Professor M. Douglas LeVan

Professor Peter N. Pintauro

This work is especially dedicated
To my wonderful daughter, Juanita Sofia, her smile was the best part of this project,
To my beloved wife, Angela, her love was infinitely inspiring in this journey, and
To my family in Colombia, Marcos, Libia, Gustavo, and Luis for their incessant support and dedication

ACKNOWLEDGEMENTS

I would like to start thanking my advisor and professor, Dr. Kane Jennings, who has guided me in the exciting world of research with enthusiasm and patience. He has been a great source of inspiration and encouragement throughout this formation process. His guidance has made of my research a challenging and rewarding experience, and I am infinitely grateful for that. A Professor shapes lives through education and I hope in the future, I am able to impact other people's lives in the passionate and dedicated way that Professor Jennings has inspired mine. I am also especially grateful with my all my committee members, Dr. Paul Laibinis, Dr. Eugene LeBoeuf, Dr. Douglas LeVan and Dr. Peter Pintauro for their guidance and time. Their constructive ideas have guided this research into a more complete and significant piece work.

I thank all the professors in the Chemical and Biomolecular Engineering Department. Their experience and passion were an excellent source of information and a good model for my career development. I also would like to express my gratitude to Margarita Talavera, Mary Gilleran, Mark Holmes and Rae Uson. Their guidance and attention made this learning process a wonderful experience.

I thank all the group members in the Jennings's lab for their support and friendship. Dr. Brad Berron, Dr. Christopher Faulkner, Dr. Peter Ciesielski, Dr. Brandon Booth, Carlos Escobar, and my very good friend Steven Vilt. Our discussions were always constructive and their friendship is one of the most precious gifts I have ever had. I also would like to thank all the undergraduates that worked with me during this process, including Nabijan

Nizamidin, Jake Albert, Jason Hunter, Won S. Song, Kathryn Maxwell, and Alexander Rothman. Their ideas and hard work were vital contributions to this research. I thank all my friends at Vanderbilt. They have made my life here very enjoyable and memorable. I wish them all nothing but the best.

I would like to acknowledge Dr. Bridget Rogers for use of her ellipsometer and XPS, and Dr. David Cliffel for use of his the optical microscope.

This work is the result of the inspiration, joy, and expectations of very special people in my life. For this reason, I not only dedicate this effort to them, but express them my appreciation for their dedication and constant support. I am infinitely grateful with my wife, Angela, her love and patience inspired me along this adventure. Only when I walk with her, I am a better man. I would like to thank my daughter, Juanita Sofia, she is pure joy and has taken my life to a different level since her arrival. Finally, I also would like to thank my parents, Marco and Libia, and my brothers, Gustavo and Luis, their expectations were always my strength. This piece of work has been shaped by all of them. Every page and every sentence.

Finally, I would like to thank the National Science Foundation (CBET-0731168) for the financial support of this research project.

TABLE OF CONTENTS

LIST OF TABLES

LIST OF FIGURES

LIST OF SCHEMES

CHAPTER I

INTRODUCTION

Superhydrophobic Surfaces

The modification of surface properties has become an important focus in materials research and is fueled by the interesting and diverse ways of tailoring composition and functionality, modifying architecture, and optimizing surface characteristics to impact a target application. A specific research subject that has received much attention because of its technological significance is the study of the superhydrophobic (SH) behavior of surfaces and the creation of surface modification strategies to impart such behavior on a diverse number of substrates. SH surfaces take the hydrophobic behavior of low-surface-energy materials to the limit, until the point in which the rough surface is in limited contact with the liquid phase such that water interacts only at the top of the micron-scale features decorating these types of films (Scheme 1.1). This situation results in the presence of air beneath the liquid phase and the separation between the liquid and the base of the surface.

Scheme 1.1. SH interface in which water sits atop the surface roughness.

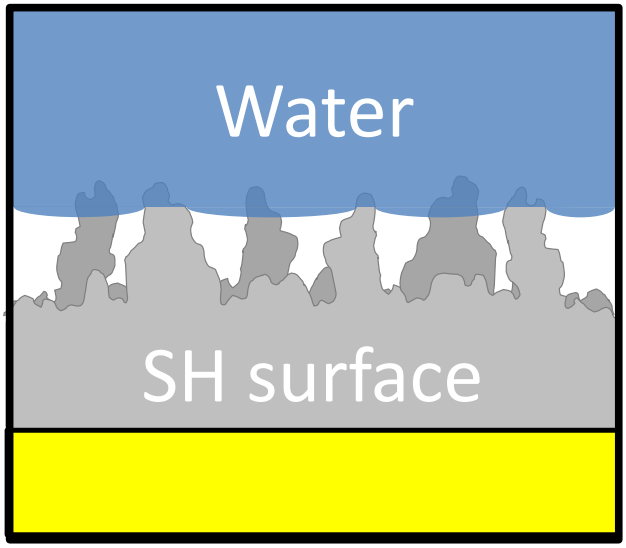

SH surfaces yield interesting and highly desirable surface properties from a technological point of view as a result of their particular interaction with water. These surfaces are inspired by the wetting properties of biological structures, especially plant leaves such as those of the Lotus (*Nelumbo nucifera*), and insects wings such as those of the cicada (*Cicada orni*).[1] Comparison studies of plant leaves made of hydrophobic or hydrophilic materials suggest that combinations of low-surface-energy materials and roughness are responsible for this SH behavior.[1] For this reason, a variety of fabrication techniques to create SH surfaces have been developed depending on how these two characteristics are imparted to a substrate. Single-step techniques use low-surface-energy materials to build micro- and/or nano-scale topographical features. Specific examples[2] include the formation of superhydrophobic surfaces by phase separation of polymers/solvent mixtures, the crystal growth of wax or Teflon, or by templating nanoscale features on polymer surfaces. On the other hand, multi-step techniques

generally use high-energy-surface materials to create the topographic features followed by their coating with low-surface-energy materials. Examples of these techniques include the topographic modification using lithographic techniques on silicon,[2] aggregation or assembly of composites,[2] electrodeposition of metals,[2] crystal growth of polymers [2] or inorganic materials,[2] or by templating nanoscale features on silicon.[2] Diversity in the preparation methods offers certain flexibility. However, in both techniques, the stability, durability and feasibility of depositing the low-surface-energy materials on the surface could be questionable since the hydrophobic materials may have weak affinity for the substrate. To overcome this potential drawback, approaches to fabricate superhydrophobic surfaces must present a strategy to grow robust low-surface-energy materials on a broad number of substrates, preferably in a single step.

The wetting properties of SH surfaces have been widely studied based on the behavior of drops contacting these type surfaces, more specifically as focused on the behavior of the triple contact line of the drop. This is an interesting approach that is of prime importance in applications in which water is in the form of drops such as micro-fluidics and guided motion applications and for self-cleaning properties. However, understanding the SH behavior based solely on this approach limits the potential of this property and narrows the span of applications that could take advantage of it. One of these potential applications is the use of SH surfaces as a protective interface against the transport of aqueous substances that could degrade or interact with an underlying substrate, such as in anticorrosion applications. At these conditions, the limited contact between the aqueous environment and the surface as well as the dielectric properties of the protective interface are vital and offer superior performance compared to smooth

protective interfaces. Other set of applications that would not be appropriately exploited if addressed using triple contact line principles are those in which the surface is immersed in an aqueous environment such as drag reduction and anti-biofouling applications. For these conditions, the triple contact line concept commonly used in the case of droplets is not present, and the fact that water is not contacting the surface in the form of a droplet, but of a plane, changes the nature of the interaction and requires a different approach from the one commonly employed. This scenario suggests the necessity to establish new standards that define the SH behavior based on concepts different from that of the triple contact line concept to take advantage of the full potential of SH surfaces.

Polyhomologation as a Versatile Synthetic Strategy to Create Superhydrophobic Surfaces

This thesis addresses the development of a new surface-initiatied polymerization (SIP) [3-6] strategy to fabricate superhydrophobic surfaces in a single step. SIP, also known as the "grafting from" method, is a technique that localizes polymerization centers or initiators at the surface, followed by exposure of the activated surface to an appropriate monomer solution. This strategy takes advantage of an actual chemical bond between the growing chain and the substrate that provides the system a remarkable stability as compared to surface-modification methods that exploit only physisorption. SIP strategies enable the preparation of robust bound coatings over objects of any shape with tailored structures, thicknesses,[7] grafting densities,[7,8] and compositions, including random and block copolymer films.[7-9] SIPs have been used to functionalize nanoparticles [7] and porous supports,[7] to prepare polymer brushes [10] and pH responsive films,[11] to provide barrier properties against etching [7] and aqueous redox probes,[12] and to alter wetting properties of surfaces.[13] However, inherent characteristics and conditions of existing

SIPs limit the number of substrates and initiators used, making necessary the development of new strategies to broaden their application based on major advances in the synthesis of polymers.[14] Here, I adapted the solution-phase polymerization approach of polyhomologation, developed by Shea and co-workers,[14-17] to a surface-initiated polymerization. This elegant solution-phase polymerization method produces homo- and co-polymers of polymethylene with low polydispersity indexes (1.04-1.17), using a tight control over the molecular weight by having the appropriate ratio of monomer to initiator and offering a rapid kinetics of polymerization.[14] We feel that polyhomologation is a flexible polymerization method that is adaptable to initiate polymerizations at a surface.

This thesis addresses the adaptation of polyhomologation into a surface-initiated polymerization strategy to grow polymethylene (PM) films from various substrates. Chapter IV describes the surface-initiated polymethylenation (SIPM) strategy that results in the formation of PM films after immobilization of borane on a vinyl-terminated monolayer and further exposure of the activated monolayer to a diazomethane (DM) solution in ether. In this chapter, we establish the nature of the polymerization and determine the physical and chemical properties of the film. Among these properties, we were particularly interested in the superhydrophobic behavior and the outstanding barrier properties exhibited by these PM films. For this reason, Chapter V presents the effect of superhydrophobicity on the dielectric properties of the film based on impedance measurements and the rationalization of such measurements using the Helmholtz theory. Using this approach, we established that SH films exhibit positive deviations from the inverse capacitance predicted by the Helmholtz theory, and we modeled the effect of the entrapped air at the PM/solution interface of SH films relative to smooth and non-

superhydrophobic (NSH) films using a composite factor (ψ). This chapter concludes with a convenient method to fully describe the conditions for superhydrophobicity in which the composite factor correlates with the wetting properties of the films.

Experimental results in Chapters IV and V demonstrate the remarkable sensitivity of impedance-based methods to assess the SH behavior of films in underwater conditions. To take advantage of this potential, Chapter VI discusses a strategy that allows the identification of the Cassie and the Wenzel states for underwater surfaces using impedance measurements. This technique is based on the controlled transition from the Cassie to the Wenzel state as a result of discrete reductions in the surface tension of the liquid phase. This chapter establishes the principles and theoretical concepts of the technique and concludes with an investigation as to how SH surfaces grown from SIPM recover their initial Cassie state after transitioning into the Wenzel.

Chapter VII expands the SIPM approach to polymeric substrates, more specifically to the case of liquid polyisoprene films. This chapter sets up both the characteristics and the protocol to create polyisoprene substrates and establishes the extension of SIPM to virtually any substrate that has incorporated olefin groups to impart superhydrophobicity. To conclude this thesis work, Chapter VIII presents the final conclusions of this research and recommends future work to develop other surface-initiated strategies to grow SH and superoleophobic films based on chemistries and chemical compositions different from the one outlined here.

References

(1) Bhushan, B.; Jung, Y. C. *Nanotechnology* **2006**, *17*, 2758-2772.

(2) Roach, P.; Shirtcliffe, N. J.; Newton, M. I. *Soft Matter* **2008**, *4*, 224-240.

(3) Seshadri, K.; Atre, S. V.; Tao, Y. T.; Lee, M. T.; Allara, D. L. *Journal of the American Chemical Society* **1997**, *119*, 4698-4711.

(4) Bai, D.; Jennings, G. K. *Journal of the American Chemical Society* **2005**, *127*, 3048-3056.

(5) Boyes, S. G.; Brittain, W. J.; Weng, X.; Cheng, S. Z. D. *Macromolecules* **2002**, *35*, 4960-4967.

(6) Prucker, O.; Ruhe, J. *Macromolecules* **1998**, *31*, 592-601.

(7) Jennings, G. K.; Brantley, E. L. *Advanced Materials* **2004**, *16*, 1983-1994.

(8) Ruckenstein, E.; Li, Z. F. *Advances in Colloid and Interface Science* **2005**, *113*, 43-63.

(9) Edmondson, S.; Osborne, V. L.; Huck, W. T. S. *Chemical Society Reviews* **2004**, *33*, 14-22.

(10) Zhao, B.; Brittain, W. J. *Macromolecules* **2000**, *33*, 342-348.

(11) Bai, D. S.; Elliott, S. M.; Jennings, G. K. *Chemistry of Materials* **2006**, *18*, 5167-5169.

(12) Bai, D. S.; Ibrahim, Z.; Jennings, G. K. *Journal of Physical Chemistry C* **2007**, *111*, 461-466.

(13) Oner, D.; McCarthy, T. J. *Langmuir* **2000**, *16*, 7777-7782.

(14) Shea, K. J.; Walker, J. W.; Zhu, H.; Paz, M.; Greaves, J. *Journal of the American Chemical Society* **1997**, *119*, 9049-9050.

(15) Shea, K. J.; Busch, B. B.; Paz, M. M. *Angewandte Chemie-International Edition* **1998**, *37*, 1391-1393.

(16) Shea, K. J.; Staiger, C. L.; Lee, S. Y. *Macromolecules* **1999**, *32*, 3157-3158.

(17) Busch, B. B.; Paz, M. M.; Shea, K. J.; Staiger, C. L.; Stoddard, J. M.; Walker, J. R.; Zhou, X. Z.; Zhu, H. D. *Journal of the American Chemical Society* **2002**, *124*, 3636-3646.

CHAPTER II

BACKGROUND

Superhydrophobic Surfaces

Superhydrophobic (SH) surfaces,[1] usually defined as those exhibiting advancing and receding contact angles of water that are greater than 150°, are often inspired by biological systems (e.g. lotus leaf) and have applications in self-cleaning surfaces,[2] water repellency,[2] interfacial slip,[3] directed droplet motion,[4] and anti-fouling interfaces.[5] To be most effective in these applications, such surfaces should be maintained in the "Cassie" regime, indicating that the water sits atop the surface roughness in contact with only a slight fraction of the surface, in contrast to the "Wenzel" regime where the water fills the grooves and is in direct contact with the rough surface (Figure 2.1).[1] Cassie surfaces are rough, often on multiple size scales, [6] enabling the entrapment of interfacial air between the surface and the contacting aqueous phase. The water molecules in contact with this air interlayer exhibit the diminished hydrogen bonding of water molecules at the surface of a droplet held in air,[7] and in many cases, the area fraction of contact between the water and a SH surface is < 5%. Thus, the air interlayer provides the vast majority of interfacial contact with the surface and liquid water, and as such, is responsible for the remarkable properties of SH surfaces.

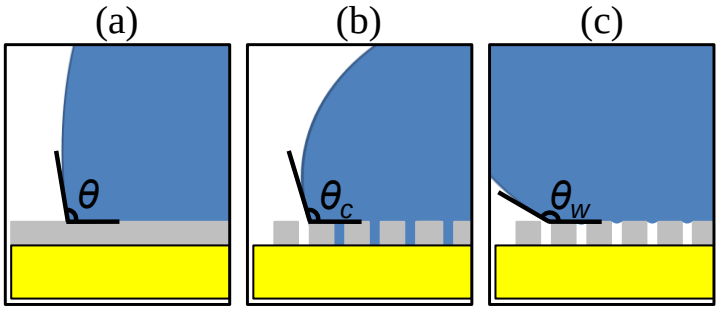

Figure 2.1. Contact angle definition depending on the topography of the surface: a) on a smooth PM film b) Wenzel contact angle c) Cassie contact angle

Polyhomologation and its Extension to Surfaces

This thesis shows the development of a synthetic platform to grow SH polymer films from a variety of substrates in a single step. To accomplish this purpose, we have adapted the solution-phase polyhomologation reaction, developed by Shea and co-workers,[8-11] into a surface-initiated polymerization to prepare SH polymethylene (PM) films. In their approach, Shea et al.[8-11] reacted a trialkyl borane initiator in solution with an appropriate ylide monomer, such as dimethylsulfoxonium methylide ($CH_2S(O)Me_2$), to produce end-functionalized polymethylene ($R(CH_2)_nX$ where R and X are various terminal groups). Scheme 2.1 shows the polyhomologation mechanism. In this mechanism, the three alkyl groups of the initiator have the same probability to undergo a 1,2 migration, resulting in a low polydispersity product that reacts with additional ylide to extend the chain length.[9] Oxidation with basic peroxide[10] or trimethylamine *N*-oxide dehydrate[12] produces an alcohol-terminated polymethylene that can be converted into various functional groups (X).[10] The terminal R-group at the opposite end of the chain is introduced by reacting an R-terminated olefin with diborane (B_2H_6) prior to react with the ylide in Scheme 2.1. Shea and co-workers have shown that many terminal groups are

compatible with this chemistry, including CH_3-,[10] $CH_3O(CH_2CH_2O)_n(CH_2)_3$-,[9] and $CH_3O(Phenyl)(CH_2)_2$- [10] groups. The primary advantages of polyhomologation[8,10] are the low polydispersity of the polymer (1.04-1.17), the rapid kinetics of polymerization, and the tight control over the molecular weight by varying the ratio of ylide to trialkylborane.

The adaptation of many innovations in polymer synthesis to surfaces has provided versatility in tailoring the composition (homopolymers and copolymers),[13,14] modifying the architecture (functionalization, hyperbranching),[14,15] and optimizing the properties (thickness, density, morphology)[16] of surface-bound polymer films. Some examples of this strategy include the adaptation of solution-phase free radical polymerization,[17,18] ATRP,[19] RAFT, ROMP,[20] anionic,[21] and cationic reactions into surface-initiated polymerizations.[22] In surface-initiated polymerizations (SIP) or "grafting from" methods,[23] an initiator is first immobilized on a surface followed by exposure of the activated surface to an appropriate monomer solution. Activation of the surface is typically attained by self-assembling adsorbates that have the initiator incorporated as the terminus, or by modifying a monolayer film to graft the initiator.[23] Advantages of using SIP include the preparation of robust, bound coatings over objects of any shape with tailored structure, thicknesses,[23] grafting densities,[23,24] and compositions, including random and block copolymer films.[23-25]

Scheme 2.1. Mechanism of reaction between a trialkylborane and dimethylsulfoxonium methylide to prepare polymethylene (PM) chains.

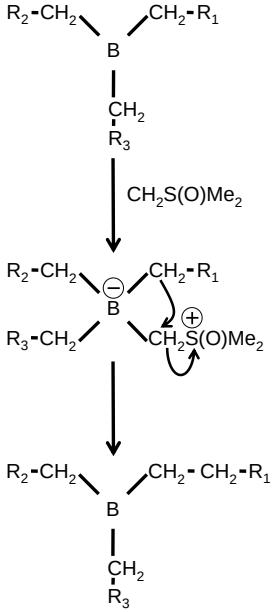

Characterization of the SH-Water Interface

Major attention has been devoted to the characterization and the fundamental understanding of superhydrophobicity. The entrapped air layer between the water/SH material interface has been spectroscopically investigated by neutron reflectivity[26] and sum frequency generation.[7] Doshi et al.[26] used neutron reflectivity to show that superhydrophobicity prevented the water filling of pores in an aerogel-like material and enabled estimation of the thickness of the interfacial air layer. Asanuma et al.[7] used sum frequency generation to investigate the interfacial structure of water on SH quartz. The spectra revealed a dominant "free OH" stretching peak that is normally observed only at water-air interfaces, providing evidence for a stable three-phase water/air/quartz interface. They conclude that the water molecules are predominately in contact with air

and not polymer, as is surmised from the Cassie state and reported from contact angles measurements.

The contact angle technique is a method widely used to characterize the wetting behavior of surfaces. Here, the contact angle represents a measure of the interactions between the liquid phase and the solid as a droplet advances, recedes, or is simply placed on the surface. The contact angle observed from each one of these events depends on the chemistry and topography of the surface as well as on the nature of the liquid drop,[27] and establishes, as indicated by their name, the advancing (θ_A), receding (θ_R) and equilibrium contact angles. While θ_A and θ_R, result from opposite events, they are not necessarily reverse processes since they require different activation energies to occur, depending on the surface.

To illustrate the advantages of contact angle (CA) measurements in the assessment of the SH behavior for droplets, we observe the CA behavior of water on different PM surfaces. In the case of a smooth surface the contact angle of PM is ~103°.[28] However, the introduction of roughness to the same material through methods such as crystallization [29,30] or plasma modifications [31] can boost the CA to values approaching 180°.[30] To rationalize the effect of film topography,[6,32,33] roughness has directly or indirectly been included in the Wenzel and the Cassie contact angle models. In the Wenzel model,[34-36] the water is assumed to wet the entire solid surface area, and the topography of the surface is accounted for by defining the roughness ratio (r).[6,34]

$$r = \frac{\text{actual area wetting the solid}}{\text{geometrical area}} \qquad (2.1)$$

The predicted or Wenzel contact angle can be related to the contact angle on a smooth PM surface (θ_{PM}) by

$$\cos\theta_W = r\cos\theta_{PM} \tag{2.2}$$

In the Cassie model,[6,27,37,38] the water is assumed to not completely wet the solid surface area, enabling the presence of entrapped air in the grooves under the drop. Therefore, the composite interface is comprised of liquid-solid, liquid-air, and solid-air interfaces. In the Cassie model, the resulting contact angle (θ_C) is estimated (Equation 2.3) as a contribution between the contact angle of the drop on a flat PM surface (θ_{PM} = 103°) and the contact angle of the liquid in air (θ_{Air} = 180°).

$$\cos\theta_C = \phi_{PM}\cos\theta_{PM} + \phi_{Air}\cos\theta_{Air} \tag{2.3}$$

$$\cos\theta_C = \phi_{PM}(\cos\theta_{PM} + 1) - 1 \tag{2.4}$$

$$\phi_{PM} + \phi_{Air} = 1 \tag{2.5}$$

where ϕ_{PM} and ϕ_{Air} are the fractions of the projected area of the surface for polymer and air, respectively. The Cassie and Wenzel models are conceived as different wetting regimes,[35,36] where the Cassie state is a meta-stable regime that, after time or the application of external perturbation, transitions into the more stable Wenzel regime. Bico et al. proposed that both states are delimited by a critical roughness (r_c), in which surfaces with roughness ratios lower than r_c favor the formation of drops in the Wenzel state.[35]

$$r_c = \frac{\phi_{PM} - 1}{\cos\theta_{PM}} + \phi_{PM} \qquad (2.6)$$

Besides the substantial increase in the contact angle (θ_A>150°), superhydrophobic films also require that differences between advancing (θ_A) and receding (θ_R) contact angles, known as hysteresis, be less than 10°.[6] Gao and McCarthy [33] showed that introduction of nano-scale roughness to an originally micro-scale-rough surface decreased the surface hysteresis from 20° to 0°, thus, influencing the behavior of water droplets on the surface and making them easily rebound from the surface.[39]

Characterization and fundamental understanding of superhydrophobicity based on CA measurements has been a vital approach to establish the wetting properties of these surfaces. However, understanding the SH behavior based solely on this approach limits its potential. For this reason, to expand the span of applications that could take advantage of the SH behavior, this thesis focuses on the characterization and rationalization of the barrier properties of SH surfaces. A common example in which these properties play an important role is in the protection of interfaces against transport of aqueous substances that could degrade or interact with an underlying substrate such as in anticorrosion applications. Only a few groups have reported SH coatings for corrosion protection. Chen and co-workers assembled n-tetradecanoic acid onto roughened copper[40] and aluminum[41] substrates to achieve surfaces with equilibrium contact angles of ~150°. Electrochemical characterizations suggest the films are multilayers, but this is not established by other characterization methods. Impedance results indicate 15- and 25-

fold enhancements in charge transfer resistance on aluminum[41] and copper,[40] respectively, as compared to non-SH controls. In a more recent manuscript, Chen and co-workers use mixtures of dodecanethiol and tetradecanoic acid to achieve contact angles of 160° with ~5° rolling angles.[42] However, the resistances of these films were below those reported previously. Liu et al.[43] used a different approach, namely that of perfluorooctyltrichlorosilane on zinc to achieve a maximum equilibrium contact angle of 151°. The film protected the zinc substrate for 29 days, but the contact angle decreased to 100° over that time. Contact angle hystereses or other analyses to assess air entrapment at the interface were not reported in any of these studies. To allow a thorough development of these types of applications, this thesis presents for the first time an analysis devoted to the quantification of the barrier properties for SH interfaces. I isolated any degradation effects from this system through the use of an inert polymer film and a noble metallic substrate, and established the barrier properties resulting from air entrapment at the interface as well as the design variables that could optimize the SH behavior.

Specific Focus in the Dissertation

I. Develop surface-initiated polyhomologation (SIPH) as a new way to grow polymethylene (PM) films from surfaces. Investigate the topography of these SIPH PM films and its influence on the wetting and barrier properties.

II. Investigate the effect of air entrapment at superhydrophobic surfaces on the resistance against ion transfer and the dielectric properties of the polymer films. Determine the correlation between the barrier properties and the wetting behavior exhibited by SH films.

III. Develop an impedance-based strategy to differentiate the Cassie and the Wenzel wetting states for films in underwater environments.

IV. Extend this surface-initiated platform to grow SH films from polymeric substrates, more specifically for the case of liquid polyisoprene films.

References

(1) Nosonovsky, M.; Bhushan, B. *Current Opinion in Colloid & Interface Science* **2009**, *14*, 270-280.

(2) Wu, Z. P.; Xu, Q. F.; Wang, J. N.; Ma, J. *Journal of Materials Science & Technology* **2010**, *26*, 20-26.

(3) Rothstein, J. P. *Annual Review of Fluid Mechanics* **2010**, *42*, 89-109.

(4) Fang, G. P.; Li, W.; Wang, X. F.; Qiao, G. J. *Langmuir* **2008**, *24*, 11651-11660.

(5) Nimittrakoolchai, O. U.; Supothina, S. *Journal of the European Ceramic Society* **2008**, *28*, 947-952.

(6) Zhu, L. B.; Xiu, Y. H.; Xu, J. W.; Tamirisa, P. A.; Hess, D. W.; Wong, C. P. *Langmuir* **2005**, *21*, 11208-11212.

(7) Asanuma, H.; Noguchi, H.; Uosaki, K.; Yu, H. Z. *Journal of Physical Chemistry C* **2009**, *113*, 21155-21161.

(8) Busch, B. B.; Staiger, C. L.; Stoddard, J. M.; Shea, K. J. *Macromolecules* **2002**, *35*, 8330-8337.

(9) Shea, K. J.; Staiger, C. L.; Lee, S. Y. *Macromolecules* **1999**, *32*, 3157-3158.

(10) Shea, K. J.; Walker, J. W.; Zhu, H.; Paz, M.; Greaves, J. *Journal of the American Chemical Society* **1997**, *119*, 9049-9050.

(11) Busch, B. B.; Paz, M. M.; Shea, K. J.; Staiger, C. L.; Stoddard, J. M.; Walker, J. R.; Zhou, X. Z.; Zhu, H. D. *Journal of the American Chemical Society* **2002**, *124*, 3636-3646.

(12) Wagner, C. E.; Rodriguez, A. A.; Shea, K. J. *Macromolecules* **2005**, *38*, 7286-7291.

(13) Bai, D.; Jennings, G. K. *Journal of the American Chemical Society* **2005**, *127*, 3048-3056.

(14) Bai, D. S.; Ibrahim, Z.; Jennings, G. K. *Journal of Physical Chemistry C* **2007**, *111*, 461-466.

(15) Zhao, M. Q.; Zhou, Y. F.; Bruening, M. L.; Bergbreiter, D. E.; Crooks, R. M. *Langmuir* **1997**, *13*, 1388-1391.

(16) Huang, W. X.; Kim, J. B.; Bruening, M. L.; Baker, G. L. *Macromolecules* **2002**, *35*, 1175-1179.

(17) Prucker, O.; Ruhe, J. *Macromolecules* **1998**, *31*, 602-613.

(18) Prucker, O.; Ruhe, J. *Macromolecules* **1998**, *31*, 592-601.

(19) Boyes, S. G.; Brittain, W. J.; Weng, X.; Cheng, S. Z. D. *Macromolecules* **2002**, *35*, 4960-4967.

(20) Weck, M.; Jackiw, J. J.; Rossi, R. R.; Weiss, P. S.; Grubbs, R. H. *Journal of the American Chemical Society* **1999**, *121*, 4088-4089.

(21) Jordan, R.; Ulman, A.; Kang, J. F.; Rafailovich, M. H.; Sokolov, J. *Journal of the American Chemical Society* **1999**, *121*, 1016-1022.

(22) Jordan, R.; Ulman, A. *Journal of the American Chemical Society* **1998**, *120*, 243-247.

(23) Jennings, G. K.; Brantley, E. L. *Advanced Materials* **2004**, *16*, 1983-1994.

(24) Ruckenstein, E.; Li, Z. F. *Advances in Colloid and Interface Science* **2005**, *113*, 43-63.

(25) Edmondson, S.; Osborne, V. L.; Huck, W. T. S. *Chemical Society Reviews* **2004**, *33*, 14-22.

(26) Doshi, D. A.; Shah, P. B.; Singh, S.; Branson, E. D.; Malanoski, A. P.; Watkins, E. B.; Majewski, J.; van Swol, F.; Brinker, C. J. *Langmuir* **2005**, *21*, 7805-7811.

(27) Gao, L. C.; McCarthy, T. J. *Langmuir* **2006**, *22*, 6234-6237.

(28) Seshadri, K.; Atre, S. V.; Tao, Y. T.; Lee, M. T.; Allara, D. L. *Journal of the American Chemical Society* **1997**, *119*, 4698-4711.

(29) Lu, X. Y.; Tan, S. X.; Zhao, N.; Yang, S. G.; Xu, J. *Journal of Colloid and Interface Science* **2007**, *311*, 186-193.

(30) Lu, X. Y.; Zhang, C. C.; Han, Y. C. *Macromolecular Rapid Communications* **2004**, *25*, 1606-1610.

(31) Fresnais, J.; Chapel, J. P.; Poncin-Epaillard, F. *Surface and Coatings Technology* **2006**, *200*, 5296-5305.

(32) Nosonovsky, M. *Langmuir* **2007**, *23*, 3157-3161.

(33) Gao, L. C.; McCarthy, T. J. *Langmuir* **2006**, *22*, 2966-2967.

(34) Ulman, A. *Characterization of Organic Thin Films*; Butterworth-Heinemann: Boston 1994.

(35) Bico, J.; Thiele, U.; Quéré, D. *Colloids and Surfaces A: Physicochemical and Engineering Aspects* **2002**, *206*, 41-46.

(36) Marmur, A. *Langmuir* **2003**, *19*, 8343-8348.

(37) Roach, P.; Shirtcliffe, N. J.; Newton, M. I. *Soft Matter* **2008**, *4*, 224-240.

(38) Bhushan, B.; Jung, Y. C. *Nanotechnology* **2006**, *17*, 2758-2772.

(39) Chen, W.; Fadeev, A. Y.; Hsieh, M. C.; Oner, D.; Youngblood, J.; McCarthy, T. J. *Langmuir* **1999**, *15*, 3395-3399.

(40) Chen, S. G.; Chen, Y.; Lei, Y. H.; Yin, Y. S. *Electrochemistry Communications* **2009**, *11*, 1675-1679.

(41) Yin, Y. S.; Liu, T.; Chen, S. G.; Cheng, S. *Applied Surface Science* **2008**, *255*, 2978-2984.

(42) Chen, Y.; Chen, S. G.; Yu, F.; Sun, W. W.; Zhu, H. Y.; Yin, Y. S. *Surface and Interface Analysis* **2009**, *41*, 872-877.

(43) Liu, H. Q.; Szunerits, S.; Xu, W. G.; Boukherroub, R. *Acs Applied Materials & Interfaces* **2009**, *1*, 1150-1153.

CHAPTER III

EXPERIMENTAL METHODS

Experimental Procedures

Materials

Ethanol (ACS/USP grade) was used as received from AAPER. Thiolacetic acid (98%) and 1,2,4 trichlorobenzene (99%) were obtained from Acros Organics. Anhydrous lithium perchlorate (95%) was purchased from Alfa Aesar. Sodium hydroxide (ACS grade), potassium hydroxide (ACS grade), hexane (HPLC grade), hydrochloric acid (36.5-38%), and concentrated sulfuric acid (95-98%) were used as received from EMD Chemicals. 5-Hexenyltrichlorosilane and n-octadecyltrichlorosilane were purchased from Gelest, Inc. and United Chemical Technologies, respectively, and used as received. Acetone (ACS grade), benzoic acid (ACS grade), ethyl acetate (HPLC grade), methanol (HPLC grade), toluene (ACS grade), hydrogen peroxide (30%, ACS grade), and chromatographic silica gel (60-100 mesh) were used as received from Fisher Scientific. Sodium methoxide (>97%) was obtained from Fluka. Nitrogen and oxygen were obtained from J&M Cylinder Gas Inc. and Airgas, Inc., respectively. 11-Bromo-1-undecene (95%), 1-octene (98%), 1-octadecanethiol, borane-tetrahydrofuran (THF) complex solution (1.0 M), Diazald (N-methyl-N-nitroso-p-toluenesulfonamide, 99%), anhydrous diethyl ether (>99%), phenolphthalein (ACS grade), copper sulfate (98%), silver sulfate (99.999%), *cis*-polyisoprene (Mw ~38,000 by GPC, made from natural

rubber), and anhydrous tetrahydrofuran (>99.9%) were acquired from Sigma-Aldrich. Deionized water (16.7 MΩ•cm) was purified using a Modu-Pure system and used for electrochemical characterizations and rinsing. Gold shot (99.99%) and chromium-coated tungsten filaments were purchased from J&J Materials and R. D. Mathis, respectively. Silicon wafers (100) were obtained from Montco Silicon, rinsed with water and ethanol, and dried in a stream of nitrogen. Polished gold-coated QCM quartz crystals (5 MHz) were obtained from Inficon and precleaned in piranha solution (7:3 H_2SO_4:H_2O_2(aq) by volume) for 2 h before use.

Preparation of Diazomethane (DM).

DM was carefully synthesized according to literature to produce a 16 mM solution in diethyl ether.[4] According to each experiment, the original DM solution was diluted in ether to the targeted concentration and stored at -17°C. The concentration of DM was determined by titration with benzoic acid.[4] Caution: Diazomethane is toxic and potentially explosive, and should be handled carefully.[4]

Synthesis of Undec-10-ene-1-thiol.

The thiol was synthesized from the corresponding bromide by sequentially using the thioacetate method[5] and acidic solvolysis conditions.[6] Under a nitrogen atmosphere 11-bromo-1-undecene (1.543 g) and thiolacetic acid (0.529 g) were added to 61 mL of methanol in a stirred flask. The system reacted for 10 h under reflux, and thin layer chromatography (TLC) with hexane as solvent was used to determine the end of the reaction. After the bromide completely reacted, hydrochloric acid was added to the

system under N_2 atmosphere and reacted for 12 h. Depletion of the acetate was determined by TLC using a solution of hexane/ethyl acetate (30/1) as solvent. At the end of the reaction, the product was dissolved in hexane, washed with water, and dried by addition of calcium chloride, followed by decantation of the organic phase. To purify the thiol, the organic phase was concentrated under reduced pressure and then separated using column chromatography with a solution of hexane/ethyl acetate (30/1). Finally, the thiol was concentrated using a rotovapor.

Preparation of Silver- and Copper-modified Gold Substrates.

Silicon (100) wafers were rinsed with water and ethanol and dried in a stream of N_2 prior to placement in a metal atom evaporator and reducing the pressure to 4×10^{-6} Torr with a diffusion pump. Then, chromium (100 Å) and gold (1250 Å) were evaporated in sequence onto silicon at rates of 1-2 Å s^{-1}. After bringing the chamber to atmospheric pressure and removing the gold-coated silicon wafers, 1.2 cm x 4 cm gold samples were cut from the wafer, rinsed with ethanol, and dried with N_2 before use.

To alter the kinetics of the spontaneous decomposition of DM on gold and produce NSH PM films of comparable thickness to the SH films prepared through SIPM, the surface of gold was atomically modified by underpotential deposition (UPD) of copper prior to DM exposure. Copper-modified gold substrates with a fractional coverage of 0.6 (60%)[7] were prepared by electrochemically cycling the gold-coated silicon samples (working electrodes) in a 0.1 M H_2SO_4(aq) solution containing 1 mM $CuSO_4$, using a CMS300 potentiostat (Gamry Instruments) connected to a personal computer. The working electrode was removed from the cell under a controlled potential

on the cathodic scan at 100 mV. Upon emersion from the electrochemical cell, the UPD-modified substrates were rinsed with ethanol, dried with nitrogen, and quickly exposed to conditions for polymerization.

To inhibit the spontaneous decomposition of DM on gold, the surface of gold was atomically modified by underpotential deposition (UPD) of silver prior to DM exposure. Silver-modified gold (Ag/Au) substrates with a fractional coverage of 0.9 (90%)[8] were prepared by electrochemically cycling 1.2 cm x 4 cm gold-coated silicon samples (working electrodes) in a 0.1 M H_2SO_4(aq) solution containing 0.6 mM Ag_2SO_4, using the CMS300 potentiostat (Gamry Instruments). The working electrode was emersed under a controlled potential on the cathodic scan at 60 mV. Upon emersion from the electrochemical cell, the UPD-modified substrates were rinsed with water and ethanol, dried with nitrogen, and quickly exposed to conditions for SAM formation.

Vinyl-terminated self assembled monolayers (SAM) on modified gold substrates were prepared by immersing the samples for 12 h in a 1 mM undec-10-ene-1-thiol solution in ethanol. After removal from the thiol solution, the samples were rinsed with ethanol and dried with nitrogen. To prepare methy-terminated monolayers, a similar protocol was implemented using a 1 mM solution of 1-octadecanethiol in ethanol.

Preparation of Silicon Substrates.

Silicon (Si) substrates were cut from silicon wafers into 1.2 cm x 4 cm samples, sonicated in ethanol for 30 min, and dried in a stream of nitrogen. Then, the samples were exposed to piranha solution (14 mL H_2SO_4: 6 mL H_2O_2) for 45 min to remove adventitious carbon and generate a hydroxylated surface. The samples were rinsed 4

times by submersion in water and once in ethanol and dried thoroughly in a stream of N_2.[9] Monolayers were formed on silicon surfaces by immersing the samples in a 1 mM solution of 5-hexenyltrichlorosilane solution or n-octadecyltrichlorosilane in anhydrous toluene for 5 h to obtain vinyl- and methyl-terminated monolayers, respectively. Upon removal from solution, the samples were rinsed in toluene and dried in a stream of N_2.

Preparation of Polyisoprene Substrates.

Methyl-terminated monolayers on Si and Au were dip-coated in a 1 mM solution of cis-polyisoprene in hexane for 1 min after immersion at constant velocity of 18 mm/min. After the immersion time, the samples were withdrawn from the solution at a constant rate of 18 mm/min followed by drainage of the excess of polymer by immersion and withdrawing of the sample in hexane at a constant velocity of 45 mm/min. The excess of solvent was evaporated from the sample after exposure to laboratory conditions and before performing surface-initiated polymerization.

Preparation of Polymer Films.

Vinyl-containing films on Au, Ag/Au, Cu/Au and Si were placed under nitrogen in a septum-capped vial by 3 cycles of evacuation followed by N_2 backfilling. A 0.1 M solution of borane in THF was added to the vial via cannula. After 2 h of reaction, the borane solution was evacuated from the system and the samples were rinsed 3 times with anhydrous THF via cannula. To grow PM films from *cis*-polyisoprene films on Si and Au, a similar protocol was implemented using a hydroboration time of 15 min. Finally, the samples were immersed in a DM solution at -17 °C for various times, and upon

removal from the DM solution, they were vigorously rinsed with trichlorobenzene and ethanol, and dried in a stream of nitrogen. PM films were classified as SH if they exhibited advancing contact angle values[10] greater than $150°$, hysteresis parameters ($H = \cos\theta_R - \cos\theta_A$)[11,12] lower than 0.14 and a dimensionless composite factor (ψ) greater than ~1.5. Smooth NSH PM films were prepared by immersing copper-modified gold substrates in the same DM solution as NSH films for various times, and upon removal from the solution, they were rinsed with ethanol and dried in a stream of nitrogen.

Oxidation of Hydroborated Films.

Hydroborated films on Au and Ag/Au were preoxidized[13] by exposing freshly prepared films to O_2-saturated THF for 1 h and water for 30 min (HBO), followed by rinsing the monolayers with ethanol and water and drying them with a stream of nitrogen. Hydroborated monolayers on Si were oxidized by exposing the surfaces to a 0.2 N solution of NaOH in H_2O_2 (30%). The system reacted for 12 h under inert atmosphere, and the resulting monolayers were rinsed with ethanol and water, and dried under a stream of nitrogen.[14]

Characterization Methods

Ellipsometry

Ellipsometry is a technique that allows the measurement of thicknesses between 0.1 nm and 100 μm, depending on the spectral range used and the homogeneity of the

films.[15] This technique takes advantage of the change in polarity suffered by an incident beam from linear polarized light into elliptically polarized light when reflected from a sample surface. Changes in polarity result from alterations in the intensity and phase of the parallel and perpendicular components, therefore, enabling characterization of the system.[16] Both ellipsometric parameters: phase (Δ) and amplitude (Ψ) of the reflected light are collected by a detector and connected to the coefficient of reflection ρ using the fundamental equation of ellipsometry

$$\rho = \tan\psi e^{i}\Delta \tag{3.1}$$

ρ contains information about the properties of the sample and is defined as the complex ratio of the Fresnel coefficient of reflection for the parallel (r_p) and perpendicular (r_s) components of the incident-plane-polarized electrical field vector

$$\rho = \frac{r_p}{r_s} \tag{3.2}$$

To represent a film on the surface, model layers are used to fit theory to the measured data. In the case of polymer films, a generic two-term Cauchy layer model was used for this purpose

$$n(\lambda) = A + \frac{B}{\lambda^2} + \frac{C}{\lambda^4} \tag{3.3}$$

Here, λ is the wavelength and the terms on the right are optimized according to a minimization of the mean square error to fit to the experimental spectra and enable estimation of both the refractive index, *n*, and thickness of the film.[17] Data were collected at one angle (75°) and over an extensive wavelength range (250 – 1000 nm) to ensure more accurate fits of theoretical models to the data. The theoretical model layers used in this technique are not appropriate for describing highly rough films; thus, different techniques such as profilometry and quartz crystal microbalance (QCM) were necessary to quantify thicknesses for SH films.

Thicknesses of films grown from non-hydroborated surfaces were measured with a J.A. Woollam XLS-100 variable angle spectroscopic ellipsometer. At a 75° angle of incidence, 100 revolutions/measurement were taken across a range of wavelength (200-1000 nm) for each sample. WVASE 32 Version 3.374 software was used to model and calculate the thickness of the films. For films on Au and Ag/Au, fresh and uncoated substrates served as a baseline for thickness measurements and were used to determine the optical constants of the substrate. The film thickness was estimated as the average of three measurements at different points across the substrate, using the Cauchy model with the coefficients set at A = 1.5 and B = C = 0. Reported errors represent the averages and standard deviations, respectively, from at least two independently prepared films.

Profilometry

Profilometry was used to determine the thickness of PM films in the ~150 nm to 5 μm range. The tip design enables characterization of surface aspect ratios as high as 10:1. Based on the contact stylus profilometry technique, thicknesses were measured by

profiling the surface with a stylus tip and translating its vertical displacement into a transducer's voltage output that enables the determination of the thickness after appropriate calibration.[18]

Profilometry measurements were performed in a Veeco Dektak 150 profiler, using 49 μN of force and the hills and valleys detection mode. The thickness was estimated by manually scratching[19] the surface, scanning 500-1000 μm across the scratch with the profilometer, and plane-fitting the scan results using the instrument software. Reported errors represent the averages and standard deviations of at least two independently prepared films.

Quartz Crystal Microbalance (QCM)

Quartz crystal microbalance (QCM) was used to estimate the thickness of PM films. This technique is based on the piezoelectric properties of quartz, which enables building a resonator by placing an appropriately cut quartz crystal in an oscillator circuit.[20] Such a circuit oscillates at a fundamental frequency (f_0 = 5 MHz) that shifts (Δf) due to mass loading (Δm) of the target molecules.

QCM measurements were performed with a PM-700 series plating monitor (Maxtek, Inc.) to estimate the film thicknesses on polymethylenated surfaces. Polished, gold-coated quartz crystals (5 MHz, Maxtek) were cleaned with piranha solution (7:3 H_2SO_4:H_2O_2(aq) by volume) before use. Ag-modified gold crystals were prepared by upd as described above. Upon emersion from the electrochemical cell, the Ag/Au crystal was rinsed with water and ethanol, dried with N_2, and quickly mounted in the QCM probe. After determining the QCM reference frequency, the crystal was removed from

the probe and was then immediately immersed into the undec-10-ene-1-thiol solution and subsequently polymerized as described above. The change in the characteristic resonant frequency (Δf) of the crystal was determined after polymerization, and from this value, the change in mass (Δm) was calculated using Sauerbrey's equation[21]:

$$\Delta m = -\frac{A(\rho_q \mu_q)^{1/2} \Delta f}{2 f_0^2} \tag{3.4}$$

where f_0 is the original crystal oscillation frequency (5 MHz), A is the surface area of the crystal gold electrode (1.327 cm^2), and ρ_q and μ_q are the crystal density (2,648 kg/m^3) and the crystal elastic shear modulus (2.947×10^{10} kg m^{-1} s^{-2}),[20] respectively. The average thickness of the PM films can be estimated by dividing Δm with A and ρ, where ρ is the film density, assumed to be the same as that of bulk PM (0.92 g/cm^3).[22]

Reflectance Absorption Infrared Spectroscopy (RAIRS)

Reflectance absorption infrared spectroscopy (RAIRS) is a non-destructive, vibrational spectroscopic technique used to establish the film composition and to determine the structural information of organic films. This technique uses the radiation of an incident beam to excite the molecular dipoles of the molecules on the surface. At specific frequencies, excitation of the dipole moment occurs for particular moieties (-CH_2, -CH_3, -CO_2H), resulting in bands in the infrared spectrum. To provide structural information of a film, this technique establishes the orientation of the various modes present in a film as a result of the proportionality existent between the intensity of the

peaks for a particular mode and the square of the component of its dynamic dipole moment normal to the surface[23]

$$I \propto \cos^2 \theta_{mz} \tag{3.5}$$

In this equation, I is the spectral intensity and θ_{mz} represents the average angle between the surface normal (z) and the transition dipole moment (m) for a specific mode. This relationship indicates that the band intensity exhibits its highest value when the transition dipole moment is normal to the surface ($\theta_{mz} \rightarrow 0°$), and its minimum when the transition dipole moments are parallel to the surface ($\theta_{mz} \rightarrow 90°$).[24] These fundamental aspects of the technique indicate that molecular groups within the polymer film absorb the IR radiation to yield absorbance peaks in the spectrum with intensities that depend on the concentration of those groups within the films and the orientations of their transition dipole moments relative to the electric field.[17] For proper reference and assignment, Table 3.1 lists the peak position of the modes commonly present in the organic films shown in this thesis. Further discussion about the IR spectra will be addressed as necessary.

PM-IRRAS spectra for SAMs were collected using a Bruker PMA-50 attachment to a Bruker Tensor 26 infrared spectrometer equipped with a liquid-nitrogen cooled mercury-cadmium-telluride (MCT) detector and a Hinds Instruments PEM-90 photoelastic modulator. The source beam used a half-wavelength ($\lambda/2$) retardation modulated at a frequency of 50 kHz and set at 80° incident to the sample surface. Spectra

for SAMs on gold substrates were collected over 5 min (380 scans) at a resolution of 4 cm^{-1}.

RAIR spectra for PM films on Au and Ag/Au substrates were collected with a Varian Excalibur FTS-3000 infrared spectrometer using p-polarized light incident 80° from the surface normal. The instrument was run in single reflection mode using a universal sampling accessory and a nitrogen-cooled, narrow-band MCT detector. A background spectrum was collected on Au and Ag/Au previously exposed to deuterated *n*-dodecanethiol ($C_{12}D_{25}SH$). After the reference sample was exposed to ambient air, a second spectrum was collected to be subtracted from the spectrum of all films to eliminate peaks due to ambient humidity. Each spectrum was collected over 200 scans with a spectral resolution of 2 cm^{-1}.

Table 3.1. Positions of the absorbance peaks for the modes present in the organic films shown in this thesis.[1-3]

Peak position (cm-1)	Mode	Description
3040	=CH	Moderate bands for the =CH stretching
2964-2907	CH_3	Strong bands for the CH_3 stretching
2920-2850	CH_2	Strong bands for the CH_2 stretching
1667	C=C	Moderate bands for the C=C stretching
1470-1460	CH_2	Moderate bands for the CH_2 bending
1379-1324	CH_3	Moderate bands for the CH_3 bending
1263	B-O	B-O stretching
1250	CH_2	Moderate bands for the CH_2 twisting
1131	C-C	Moderate bands for the C-C stretching
1095	CH_2	Moderate bands for the CH_2 twisting
1040	CH_3	Moderate bands for the CH_3 rocking
833	=CH	Strong bands for the =CH out-of-plane
730-720	C-H	Weak bands for the C-H rocking

X-ray photoelectron spectroscopy (XPS)

X-ray photoelectron spectroscopy is a technique that measures the kinetic energy and number of escaping electrons from a surface as the material is irradiated with x-rays in ultra high vacuum conditions. In these conditions, the composition, chemical state, and electronic state of the material are determined for the outermost ~10 nm of the interface.[25] Experimental results are reported in counts per second as a function of

binding energy. In this context, the binding energy (E_B) and the kinetic energy (E_K) are related by the following relationship

$$E_K = h\nu - E_B - \Phi \tag{3.6}$$

where $h\nu$ is the energy of the incident photons and Φ is the work function of the spectrometer.[25]

The XPS analysis was performed using a PHI 5000 VersaProbe spectrometer. Samples were irradiated with a 25 W monochromatic Al Kα X-ray (1486.7 eV) with a 100 μm spot size. Photoelectrons were collected from a 45° takeoff angle with respect to the surface normal into a spherical capacitor analyzer operated in constant pass energy mode. Both an electron neutralizer of 1.1 eV and an Ar^+ ion neutralizer of 10 eV were used on all samples to counteract any charging effects. Survey spectra were collected over a binding energy range from 0-1300 eV at a pass energy of 187.7 eV. High resolution spectra were collected at a pass energy of 58.7 eV. All spectra were collected over a 400 by 400 μm area. Data were analyzed using CasaXPS data analysis software to calculate the atomic percentages using the peak area and elemental sensitivity factors.[26]

Electrochemical Impedance Spectroscopy (EIS)

Electrochemical impedance spectroscopy (EIS) measures the resistance experienced by redox probes that are driven by an electric field to the working electrode in an electrochemical cell.[16] In our system, the circuit consists of a film-coated metal as the working electrode in contact with a conductive aqueous solution, along with a gold-

coated silicon counter electrode and an Ag/AgCl/saturated KCl reference electrode. During an EIS experiment, the current flow in the system is recorded while the potential of the working electrode changes with a sinusoidal perturbation of varying frequency. To determine the impedance (Z) of the film, the applied potential, *E(t)*, and the resulting current, *I(t)*, at time t are recorded and related using the following equation[27]:

$$Z = \frac{E(t)}{I(t)} = \frac{E_0 \cos(\omega t)}{I_0 \cos(\omega t - \phi)} = Z_0 \frac{\cos(\omega t)}{\cos(\omega t - \phi)} \qquad (3.7)$$

where E_0 is the amplitude of the potential, ω is the radial frequency (equals $2\pi f$ where f is the frequency in Hz), I_0 is the amplitude of the current, ϕ is the phase shift of the output signal, and Z_0 is the magnitude of the impedance. From Equation 3.7, the impedance of a system can be characterized by a magnitude and a phase shift.

The magnitude of Z is given by

$$|Z|^2 = (Z_{\mathrm{Re}})^2 + (Z_{im})^2 \qquad (3.8)$$

where

$$Z_{\mathrm{Re}} = R \qquad (3.9)$$

and

$$Z_{\mathrm{Im}} = \frac{1}{j\omega C} \tag{3.10}$$

where R is resistance, C is capacitance, and j^2=-1.

A popular presentation method for impedance data is the Bode plot in which log |Z| and phase angle are plotted as a function of log frequency. When a coating behaves as an ideal capacitor, the Bode magnitude plot shows a straight line with a slope of -1, and the phase angle is -90°. When the film behaves as a resistor, |Z| is insensitive to frequency, and the resistance due to solution and charge transfer are denoted as flat lines at low and high frequency, respectively, while the phase angle is 0°.

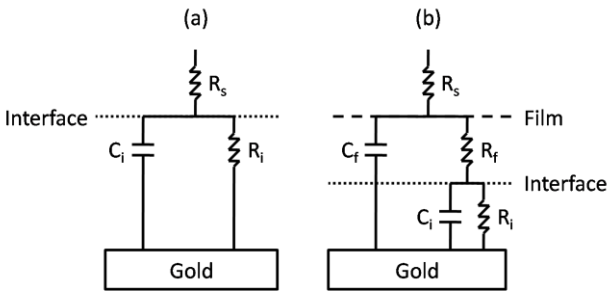

Figure 3.1. Equivalent circuit models used to represent impedance spectra for organic films.

The impedance data can be fitted by an equivalent circuit model composed of capacitors and resistors. Figure 3.1a presents the simple Randle's circuit model, which often enables describing the impedance of a bare metal or a SAM-coated metals.[28] In this model, the solution resistance (R_s) is in series with the interfacial impedance, defined as the parallel contribution of the interfacial capacitance (C_i) and resistance (R_i), which are

modulated if a SAM is present. This model can also account for mass transfer limitations using a Warburg impedance (Z_w) in the circuit. Figure 3.1b presents the general case of a metal surface covered by a polymer film,[29,30] where both the film and the organic/metal interface contribute to the total impedance. This model may be simplified based on the relative values of each circuit component. For example, if the resistance of the film (R_f) is much larger than the interfacial impedance, the spectrum will only exhibit a single time constant that is representative of the film and is analogous to the Randle's model. Here, EIS was used to determine the electrochemical properties (capacitance and resistance) of PM films and SAMs on metal electrodes.

EIS was performed with a Gamry Instruments CMS300 impedance system interfaced to a personal computer. The working electrode was mounted in a Flat Cell (EG&G) in which 1.0 cm^2 of the sample was selectively exposed to an aqueous solution of 1 mM $K_3Fe(CN)_6$, 1 mM $K_4Fe(CN)_6 \bullet 3H_2O$, and 0.1 M Na_2SO_4. Measurements were obtained using a Ag/AgCl, saturated KCl electrode as reference and an evaporated gold on silicon substrate as counter electrode. Data were collected between 10^{-1} and 10^4 Hz.

Scanning Electron Microscopy (SEM)

SEM provides high resolution images (~1 nm limitation) of the topography as well as the composition of surfaces and was used here to distinguish the morphologies of PM films grown from different surfaces. Surfaces are bombarded with electrons with a specified energy. Secondary and backscattered electrons are collected to form an image of the surface. Secondary electrons are electrons ejected from the sample due to inelastic collisions with source electrons, most from within the first few nanometers of the

material. These secondary electrons usually have less than 50 eV of energy. Backscattered electrons are source electrons that collide with nuclei with little loss of energy and are reflected "back". Backscattered electrons usually have energies greater than 50 eV.[31,32] The energy of backscattered electrons is proportional to the size of the nuclei with which they interact; therefore, the brightness of the image can be correlated to composition of the sample surface. SEM images were obtained using a Raith e-Line electron beam lithography (EBL) system equipped with a thermal-assisted field emission gun at 10 keV.

Atomic Force Microscopy (AFM)

Atomic force microscopy (AFM) is a scanning probe technique used to image the topography of a surface. To measure the topography of a surface, AFM relies on the detection of the deflections of a tiny cantilever holding a sharp tip when scanning the surface. Currently, cantilevers are made of Si, Si_3N_4, or SiO_2 [33] and tips are made of Si_3N_4 or SiO_2.[34] Attractive and repulsive forces are measured when a tip approaches the sample surface. However, repulsive forces that are extremely short range in nature are responsible for atomic resolution.[33]

When scanning the surface, the AFM can use the partial influence of the repulsive force from the sample to vibrate (tapping mode) or remain static and make contact with the sample surface (contact mode).[33] To eliminate potential damage to the surface due to lateral forces (i.e. scraping) across the sample and improve lateral resolution, soft polymeric materials are usually operated in tapping mode.

AFM images were obtained with either a JEOL 5200 scanning probe microscope (SPM) or a Digital Instruments Nanoscan III atomic force microscope (AFM) under an ambient laboratory environment. Areas of 1.5-10 μm were scanned in tapping mode with a silicon nitride tip (~100 kHz frequency), and the images were plane-fitted and filtered to remove noise using the instrument software.

Contact Angle

Contact angles are a semiquantitative assessment of the surface energy of the outer half nanometer of an organic film. To measure a contact angle, a ~5 μL probe fluid drop is placed on top of a surface using a syringe. The needle of the syringe remains inside the probe fluid droplet as the advancing and receding contact angle measurements are taken. Water (H_2O) and hexadecane (HD) are generally used as contacting liquids to indicate the relative hydrophilicity/hydrophobicity and oleophilicity/oleophobicity of a surface. H_2O will exhibit high contact angles if any hydrophobic material is present at the surface whereas HD has a greater sensitivity to specific chemical groups, especially in distinguishing hydrocarbon groups from fluorocarbon groups.[35] A more complete description of contact angles, including hysteresis and models to describe roughness, was presented in Chapter II.

Advancing and receding contact angles were measured with a Rame-Hart goniometer on static ~5 μL drops. A syringe was used to apply DI water, in which the needle of the syringe remained inside the probe fluid droplet as the advancing and receding contact angle measurements were taken. Reported errors represent the averages and standard deviations, respectively, from at least four independently prepared films.

Force Tensiometer

Force tensiometry is an accurate technique to measure the interfacial tension of liquids. Here, we use it to estimate the surface tension of water-ethanol solutions at various concentrations. In this technique, a solid is in contact with the liquid of interest to favor the formation of a meniscus, and the surface tension is correlated to the force exerted by the meniscus as the Wilhelmy plate is withdrawn from the liquid phase. In this thesis, the surface tension of various water-ethanol solutions were measured with a Sigma 70X model 1000 IUP tensiometer by KSV Instruments LTD. Measurements used a platinum plate and the Wilhelmy method to estimate the surface tension as an average from at least seven independent measurements.

References

(1) Silverstein, R.; Webster, F. *Spectrometric identification of organic compounds*; Sixth ed.; John Wiley and Sons, Inc.: New York, 1998.

(2) Tuberquia, J. C.; Nizamidin, N.; Harl, R. R.; Albert, J.; Hunter, J.; Rogers, B. R.; Jennings, G. K. *Journal of the American Chemical Society* **2010**, *132*, 5725-5734.

(3) Colthup, N.; Daly, L.; Wiberley, S. *Introduction to infrared and Raman spectroscopy*; 3 ed.; Academic Press: Boston, 1990.

(4) Black, H. *Aldrichimica Acta* **1983, 3-10**, *15* 3-10.

(5) Wardell, J. L. *The Chemistry of the Thiol Group: Preparation of Thiols*; John Wiley & Sons: London, 1974; Vol. 1.

(6) Graupe, M.; Koini, T.; Wang, V. Y.; Nassif, G. M.; Colorado, R.; Villazana, R. J.; Dong, H.; Miura, Y. F.; Shmakova, O. E.; Lee, T. R. *Journal of Fluorine Chemistry* **1999**, *93*, 107-115.

(7) Guo, W. F.; Jennings, G. K. *Langmuir* **2002**, *18*, 3123-3126.

(8) Jennings, G. K.; Laibinis, P. E. *Langmuir* **1996**, *12*, 6173-6175.

(9) Cione, A. M.; Mazyar, O. A.; Booth, B. D.; McCabe, C.; Jennings, G. K. *Journal of Physical Chemistry C* **2009**, *113*, 2384-2392.

(10) Dorrer, C.; Ruhe, J. *Soft Matter* **2009**, *5*, 51-61.

(11) Chen, W.; Fadeev, A. Y.; Hsieh, M. C.; Oner, D.; Youngblood, J.; McCarthy, T. J. *Langmuir* **1999**, *15*, 3395-3399.

(12) Boulange-Petermann, L.; Gabet, C.; Baroux, B. *Journal of Adhesion Science and Technology* **2006**, *20*, 1463-1474.

(13) Brown, H. C.; Midland, M. M. *Tetrahedron* **1987**, *43*, 4059-4070.

(14) Netzer, L.; Sagiv, J. *Journal of the American Chemical Society* **1983**, *105*, 674-676.

(15) Gruska, B.; Roseler, A. *Surface and Thin Film Analysis Priciple, Instrumentation, and Applications*; Wiley-VCH Weinheim, 2002.

(16) Bard, A.; Faulkner, L. *Electrochemical Methods*; 2nd ed.; Jhon Wiley and sons, 2001.

(17) Woollam, J. A.; Bungay, C.; Hilfiker, J.; Tiwald, T. *Nuclear Instruments & Methods in Physics Research Section B-Beam Interactions with Materials and Atoms* **2003**, *208*, 35-39.

(18) Wood, J. W.; Redin, R. D. *Review of Scientific Instruments* **1993**, *64*, 2405-2406.

(19) Manaka, T.; Ohta, H.; Iwamoto, M.; Fukuzawa, M. *Colloids and Surfaces A: Physicochemical and Engineering Aspects* **2005**, *257-258*, 287-290.

(20) Caruso, F.; Rodda, E.; Furlong, D. N. *Journal of Colloid and Interface Science* **1996**, *178*, 104-115.

(21) Fu, T. Z.; Stimming, U.; Durning, C. J. *Macromolecules* **1993**, *26*, 3271-3281.

(22) Seshadri, K.; Atre, S. V.; Tao, Y. T.; Lee, M. T.; Allara, D. L. *Journal of the American Chemical Society* **1997**, *119*, 4698-4711.

(23) Nuzzo, R. G.; Dubois, L. H.; Allara, D. L. *Journal of the American Chemical Society* **1990**, *112*, 558-569.

(24) Greenler, R. G. *Journal of Chemical Physics* **1966**, *44*, 310-&.

(25) Briggs, D.; Seah, M. P. *Practical Surface Analysis*; John Wiley & Sons Ltd.: Chichester, England, 1983.

(26) *Ulvac-PHI, Inc. (2007). Operator's PHI Multipak software manual, version 8.2C.* ; Ulvac-PHI, Inc.: Chigasaki City, Kanagawa Prefecture, Japan

(27) Gamry Instrument, I. *CMS 100 Electrochemical Measurement System Software Installation Manual* Warminster, 1998.

(28) Jennings, G. K.; Munro, J. C.; Yong, T. H.; Laibinis, P. E. *Langmuir* **1998**, *14*, 6130-6139.

(29) Bai, D. S.; Ibrahim, Z.; Jennings, G. K. *Journal of Physical Chemistry C* **2007**, *111*, 461-466.

(30) Brantley, E. L.; Holmes, T. C.; Jennings, G. K. *Journal of Physical Chemistry B* **2004**, *108*, 16077-16084.

(31) Bindell, J. B. *Scanning Electron Microscopy, in Encyclopedia of Materials Characterization: Surfaces, Interfaces, Thin Films*; Butterworth-Heinemann: Stoneham, 1992.

(32) Goldstein, J. I.; al., e. *Scanning Microscopy and X-Ray Microanalysis*; Plenum Press: New York, 1981.

(33) Seo, Y.; Jhe, W. *Reports on Progress in Physics* **2008**, *71*, 23.

(34) Friedbacher, G. *Scanning Probe Microscopy*; Wiley-VCH: Weinheim, 2002.

(35) Bantz, M. R.; Brantley, E. L.; Weinstein, R. D.; Moriarty, J.; Jennings, G. K. *Journal of Physical Chemistry B* **2004**, *108*, 9787-9794.

CHAPTER IV

SURFACE-INITIATED POLYMERIZATION OF SUPERHYDROPHOBIC POLYMETHYLENE

Introduction

Many innovations in polymer synthesis have been extended to surfaces to create versatile methods for tailoring composition (homopolymers and copolymers),[1,2] modifying architecture (functionalization, hyperbranching),[2,3] and optimizing properties (thickness, density, morphology)[4] of surface-bound polymer films. Some examples of this strategy include the adaptation of solution-phase free radical polymerization,[5,6] ATRP,[7] ROMP,[8] anionic,[9] and cationic[10] reactions into surface-initiated polymerizations. In surface-initiated polymerization (SIP) or "grafting from" methods,[11] an initiator is first immobilized on a surface followed by exposure of the activated surface to an appropriate monomer solution. Activation of the surface is typically attained by self-assembling adsorbates that have the initiator incorporated as the terminus, or by modifying a monolayer film to graft the initiator.[11] A completely different SIP approach takes advantage of the catalytic properties of some metal surfaces, since they induce spontaneous polymerization upon exposure to reactive precursors. As an example of this latter method, diazomethane (DM) spontaneously decomposes at gold surfaces to produce linear polymethylene (PM).[12,13] Advantages of using SIP include the preparation of robust, bound coatings over objects of any shape with tailored structure, thicknesses,[11] grafting densities,[11,14] and compositions, including random and block copolymer

films.[11,14,15] Here, we adapt the synthetic approach of polyhomologation, developed by Shea and co-workers,[16-19] to prepare SI polymethylene (PM) films with thicknesses exceeding 1 μm on silicon and gold supports.

In this chapter, we develop a surface-initiated polymethylenation (SIPM) to grow polymethylene (PM) films from borane-modified gold or silicon surfaces by exposure to dilute diazomethane (DM) in ether at -17°C. Scheme 4.1 presents the strategy to polymerize from immobilized trialkylborane sites on gold and silicon substrates. First, we prepare a vinyl-terminated monolayer onto the substrate.[20] Then, the initiator is immobilized on the surface by hydroborating the vinyl termini in a solution of borane (BH_3) in tetrahydrofuran (THF) under inert atmosphere. Immersion of the functionalized surface into a dilute DM solution enables polymerization from the borane centers, yielding a PM film.[21,22] Exposure of unmodified gold surfaces to diazomethane (DM) also produces a PM film due to spontaneous polymerization at gold surface sites.[13] To account for the effect of the trialkylborane initiation sites on the gold surface in the process, we predeposited a silver monolayer on the gold surface to greatly inhibit the spontaneous growth of PM films.[12,23]

Scheme 4.1. Strategy for the polymethylenation of diazomethane at heterogeneous borane sites on gold with and without a monolayer of silver, and silicon surfaces. A vinyl-terminated monolayer is exposed to a 0.1 M solution of borane in THF, followed by exposure to a DM solution in ether at -17 °C. The silver layer on gold prevents the spontaneous polymerization of DM into PM that is observed on gold.

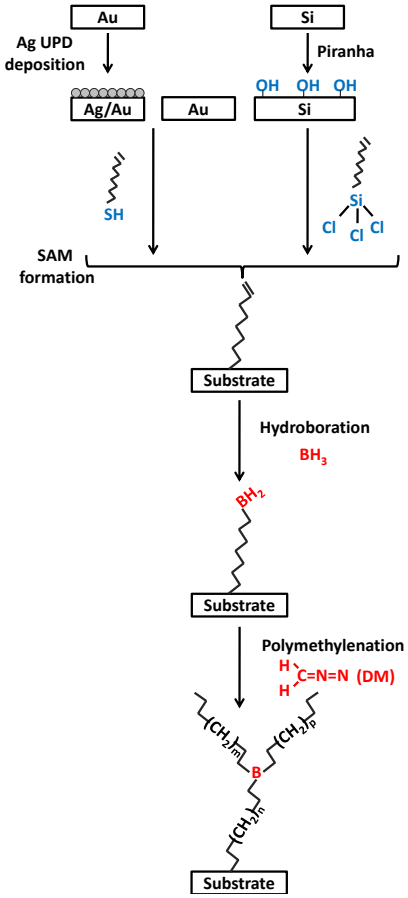

The spontaneous growth of ultrathin PM films on gold has been the subject of previous studies[1,13,23] that take advantage of the low cost, chemically inert character, and low dielectric constant of PM[24] to prepare ultrathin polymer films and overcome limitations of PM processability due to poor solubility in organic solvents[25] and poor adhesion to metal substrates[26] that limit spin coating and solution casting. Seshadri et al. grew ~50 nm PM films by exposing gold surfaces to a DM solution in ether. Our

group[12,23] developed approaches to enhance or prevent PM growth by atomically modifying gold surfaces with copper or silver, respectively. Different surfaces[27-29] also favor DM decomposition to form PM. However, polymerization by these routes relies on the inherent catalytic properties of the substrate. Using SIPM, we intend to expand the initiation capabilities of boranes to non-catalytic surfaces, thus, diversifying the number of substrates from which PM films can be grown.

In this thesis, I report the first surface-initiated polymethylenation for the growth of PM films from gold and silicon surfaces. This surface reaction is rapid in comparison to many surface-initiated polymerizations, producing PM films thicker than 500 nm after 2 min of reaction and 3 μm after 24 h of reaction. Extremely high contact angles (>160°) and low hystereses (~2°) indicate that PM films exhibit superhydrophobic behavior due to their low surface energy and their combination of micron- and nano-scale morphology. Thus, this approach changes a smooth substrate into a rough, superhydrophobic surface through a single polymerization step. Due to the presence of entrapped air at the water/polymer interface, these superhydrophobic films present large resistances against the transport of aqueous redox probes that are on the order of $1x10^{10}$ $\Omega \cdot cm^2$.

Results and Discussion

Characterization of Surface Borane

Hydroboration of olefins in solution results in trialkylboranes, except in the case of sterically hindered olefins in which hydroboration yields dialkylboranes or monoalkylboranes.[30,31] Here, we exposed a dense vinyl-terminated monolayer to a

solution of borane in THF. The immobilization of the chains within the monolayer prevents the formation of trialkylboranes, and further, the formation of dialkylboranes that would require chain termini to be within ~3 Å based on the C-B bond length[32] and the geometry of the binding, is unlikely on average, given the ~5 Å center-to-center distance between chains in an alkanethiolate monolayer.[33] Therefore, we deduce that the exposure of a vinyl-terminated monolayer to borane results predominately in a monoalkylborane and a $–BH_2$ terminus. However, characterization of the monoalkylborane SAM is challenging because our primary surface characterization methods (PM-IRRAS, XPS, etc.) require the surfaces to be exposed to air, and alkyl boranes are known to react rapidly with oxygen in the air to yield a variety of oxidized species.[34-36] Our approach was to pre-oxidize[37] the surface prior to characterization. Therein, we exposed a freshly hydroborated vinyl-terminated monolayer on gold to O_2-saturated THF for 1 h and water for 30 min (denoted as HBO) before exposure to air for subsequent characterization with PM-IRRAS and XPS.

Figure 4.1 shows the IR and the XPS spectra of an HBO surface and a vinyl-terminated SAM (C=C/Au) that were each exposed to the same oxidizing conditions. The IR spectrum of the vinyl-terminated SAM displays the C-H out-of-plane deformation (912 cm^{-1}) and the out-of-plane deformation of the C=C (993 cm^{-1}) groups characteristic of the vinylic bond.[20,38,39] The spectrum for the HBO monolayer shows a disappearance of the C=C modes, consistent with hydroboration of the vinyl functionality at the surface of the monolayer, and the appearance of a peak at 1264 cm^{-1} that we assign to symmetric B-O stretching,[40,41] suggesting the subsequent oxidation of $B-H_2$ bonds to $B-(OH)_2$ (boronic acid).[30,32,36,37] Orientation of the B-OH groups at the outer surface would result

in a dominant symmetric B-O stretch, based on surface selection rules,[42] as compared to the more commonly observed asymmetric B-O stretch[43,44] that we do not observe here. Higher reactivity of the H-B bond towards O_2 as compared to the B-C bond could result from the confinement of the latter within the SAM that lower its exposure and increases the steric hindrance towards oxidation.[45,46]

To provide an estimate of boron surface coverage on the HBO monolayer, we used x-ray photoelectron spectroscopy (XPS). Figure 4.1b shows the C(1s) and O(1s) high resolution spectra for the HBO monolayer, the vinyl-terminated monolayer, and a hydroxyl-terminated monolayer (OH/Au) prepared from $HS(CH_2)_{11}OH$ on Au. These spectra show that all monolayers exhibit the characteristic C(1s) peak for aliphatic hydrocarbons at 284.7 eV. The spectrum for the hydroxyl-terminated monolayer exhibits a shoulder at 286.8 eV corresponding to the outermost carbon that is covalently bound to the oxygen of the hydroxyl group.[47] The atomic concentration ratio of these two peaks is 10:1 consistent with the chain length of the hydroxyl monolayer. Appearance of a single and sharp peak for the HBO monolayer indicates the absence of the C-O bond, suggesting that the oxygen present in the system is not bonded to carbon, but most likely to boron. Direct detection of boron was not observed due to its low atomic concentration ($\leq$ 1 B:11 C) and small sensitivity factor, ~20% of that for oxygen.[48] Instead, we used the presence of oxygen in the spectra as indirect evidence of oxidized boron functionality. Importantly, high resolution spectra of the O (1s) region indicate the presence of oxygen on the HBO surface but not on the vinyl-terminated control. Based on a comparison of the atomic ratios of O to C in both the HBO and OH-terminated monolayers, we estimate that the oxygen level on the HBO surface is 70 ± 9% of that on a dense HO-terminated

SAM. Since boronic acids dehydrate in vacuum to form boroxine glasses with a stoichiometry of one oxygen per boron,[49] we assume that our oxidized species has one oxygen per boron per chain, yielding an estimate of boron surface coverage as 70 ± 9% from XPS. As further evidence of the presence of boron, exposure of the HBO surface on silicon to diazomethane in ether results in a PM film (vide infra) that is ~35% as thick as a film grown from an unoxidized HB monolayer, consistent with the presence of boron functionality within the monolayer after oxidation since a non-hydroborated vinyl monolayer yields no polymer.

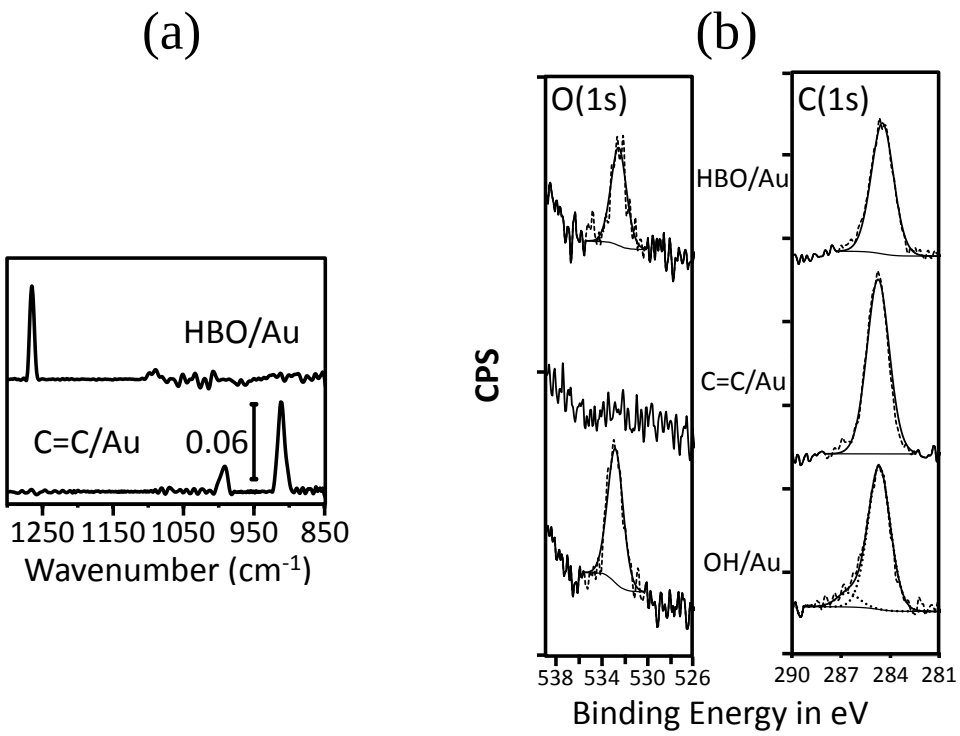

Figure 4.1. a) PM-IRRAS spectrum of a hydroborated SAM after its oxidation with pure oxygen (HBO) for 1 h and immersion in water for 30 min. For comparison a spectrum for a vinyl-terminated SAM exposed to the same conditions (C=C/Au) is also displayed. Modulation was focused in the lower (1129 cm^{-1}) region of the spectra. b) XPS spectra for a hydroborated (HBO) and a vinyl-terminated (C=C/Au) SAM after exposure to oxidation conditions. Spectrum of a hydroxyl-terminated monolayer (OH/Au) is presented for comparison. The suvey XPS spectra (not shown) confirm the presence of Au, C, O and S on all surfaces except for the absence of O on the vinyl-terminated monolayer. Spectra have been offset for clarity.

On silicon substrates, the abundance of oxygen in the native oxide layer hindered our ability to use XPS to detect oxygen levels in the monolayer as an estimate of boron coverage. Instead, we incorporated the approach of Wasserman et al.[50] to completely oxidize the surface boranes to hydroxyl groups by exposure to a 0.2 N solution of NaOH in H_2O_2 (30%) for 12 h under inert atmosphere.[51] Wasserman et al.[50] used this approach to estimate the conversion of vinyl groups to hydroxyl functionality. We observed that this harsh oxidation destroys thiolate SAMs but does not damage the more robust

siloxane-linked monolayers on silicon. Exposure of the H_2B-termini to the oxidizing conditions resulted in an advancing water contact angle (θ_{HB}) of 53°, whereas a vinyl-terminated control was not affected by the conditions as the contact angle ($\theta_{C=C}$) remained 95°. Calculations of yield were performed using the Cassie Equation,[50]

$$\cos\theta_{HB} = \phi_{C=C}\cos\theta_{C=C} + \phi_{OH}\cos\theta_{OH} \qquad (4.1)$$

where $\phi_{C=C}$ and ϕ_{OH} are the surface area fractions of the vinyl- and hidroxyl-terminations in contact with water, respectively. Assuming θ_{OH} = ~0°, the final monolayer exhibits a higher surface energy as compared to the initial vinyl-terminated monolayer, and indicates that ~35% of the surface area presents the vinyl termini ($\phi_{C=C}$) and 65% represents hydroxyl termini (ϕ_{OH}) from the direct conversion of surface boranes. This result on silicon is in good agreement with XPS results on gold and suggests that after hydroboration, ~65% of the vinyl-termini are converted to H_2B- terminations through the hydroboration step.

Effect of Substrate

To investigate the effect of hydroboration on the surface-initiated growth of PM, we measured the thicknesses of PM films grown from hydroborated surfaces and control substrates upon exposure to a 13 mM solution of DM in ether at -17°C for 24 h. Table 4.1 shows the results of the thickness measurements for PM films grown from six surfaces, including two hydroborated SAMs, one on gold (HB+Au) and another on

Ag/Au UPD (HB+Ag/Au); two vinyl-terminated SAMs not exposed to borane (SAM+Au, SAM+Ag/Au), as well as bare Au and Ag/Au surfaces. In principle, ellipsometric measurements were performed on all the films, assuming that they are uniform and isotropic and have the same refractive index as polyethylene (n = 1.5).[25] All the control films could be fit with a Cauchy model to determine their thickness, but PM films grown from hydroborated SAMs could not be fit with this simple model, perhaps due to their rough morphology (vide infra). To assess the rough morphology of the surface, we used an effective medium approximation[52] model that combined the optical constants for PM and air. However, this approach did not provide a good fitting of the experimental data. This characteristic behavior suggests that PM films grown from SIPM are distinct in comparison to the control films. To provide a measure of thickness for these rougher PM films, we performed profilometry and ex situ quartz crystal microgravimetry (QCM) measurements.[13]

Table 4.1. Thickness measurements for PM films grown from the indicated surfaces upon exposure to a 13 mM solution of DM in ether at -17 °C for 24 h.

	Ellipsometry	QCM	Profilometry
Substrate	nm	nm	nm
HB+Au	-	3608	3500 +/- 200
SAM+Au	363 +/- 12	238	344 +/- 15
HB+Ag/Au	-	3006	-
SAM+Ag/Au	1 +/- 0.1	-	-
Ag/Au	6 +/- 3	-	-
Au	224 +/- 1	182	277 +/- 5
HB+Si	-	-	1667 +/- 190
SAM+Si	1 +/- 0.2	-	-

To verify the validity of profilometry and QCM, we first compared the results for a PM film on Au with those from ellipsometry to determine if the techniques are in relative agreement. Comparison of the thickness values for PM growth on Au and SAM+Au surfaces obtained by QCM, ellipsometry, and profilometry shows that QCM-estimated thicknesses are ~25% lower than the average of the three techniques. However, the fact that, in all cases, PM films grown from SAM+Au present much higher thicknesses as compared to those grown from Au indicates that the techniques certainly agree with respect to the overall trend.

Table 4.1 shows that SIPM allows the growth of films that are 10- to 1000- fold thicker than films grown from non-hydroborated substrates. In fact, the ~3 μm-thick films produced by SIPM are among the thickest films yet reported by surface-initiated routes. From the evaluation of the non-hydroborated surfaces, we notice that silver deposition on gold surfaces (Ag/Au and SAM+Ag/Au) inhibits PM formation, as previously described by our group.[12,23] This inhibition indicates that the PM film grown on the HB+Ag/Au surface results from SIPM. In the case of the HB+Au surface, SIPM produces a film about 10 times thicker than the thickest non-hydroborated PM film (SAM+Au), supporting the dominance of SIPM toward film growth when both SIPM and surface-catalyzed[13] modes are present.

Table 4.1 also shows the thicknesses obtained after exposure of DM at the above conditions to a silicon substrate modified by 5-hexenyltrichlorosilane (SAM+Si) and one that was further modified by borane (HB+Si). While PM does not grow on SAM-modified silicon, as evidenced by a thickness that is approximately that of the SAM, it does grow from HB+Si to achieve a thickness that is 55% of that for SIPM from

HB+Ag/Au after 24 h of polymerization. We did observe that HB+Si requires longer times of polymerization to obtain comparable thicknesses to those obtained for shorter times on HB+Ag/Au and HB+Au. The slower polymerization on silicon could result from a greater extent of oxidation of this monolayer during transfer of the substrate into the DM solution for polymerization. As the 6-carbon vinyl-terminated monolayer on silicon is thinner and less crystalline than the 11-carbon monolayer on Au and Ag/Au,[53] the C-B bond within the monolayer on silicon is more exposed, and thus, more susceptible to attack by oxygen. Insertion of oxygen into the C-B bond would result in a lower number of C-B bonds that enable the polymerization. Appreciable differences in the reactivity of various boranes towards DM was reported by Davies et al.[21] in which the polymerization of PM by alkylboranes is faster as compared to that of oxidized states: $R_3B > (RBO)_3 > (R_2B)_2O > RB(OR)_2 > (RO)_3B$. Nonetheless, growth of PM films from HB+Si demonstrates the ability to extend SIPM to other vinyl-terminated substrates. For PM films grown from HB+Ag/Au and HB+Au surfaces, discrepancies in their thicknesses result from the catalytic activity of Au towards DM, resulting in slightly thicker films.

Effect of Concentration and Time

Figure 4.2 shows the effect of the time of polymerization and the concentration of DM on the PM film thickness on HB+Ag/Au substrates. Figure 4.2a shows the variation of film thickness measured by profilometry at various times of polymerization after exposure to a 15 mM solution of DM at -17° C. The films achieve thicknesses of ~1 μm after 10 min of reaction, presenting rapid kinetics as compared to other SI routes.[12,13]

The growth rate slows as the reaction proceeds, suggesting occlusion of monomers to the active borane sites. Figure 4.2b shows the effect of DM concentration on the growth of PM films after 24 h of exposure to DM solutions with concentrations between 0.2 to 15 mM at -17 °C. Film thickness increases sharply with concentration from 0 to 1 mM with a moderate dependence for higher concentrations. Figure 4.2b shows that films with thicknesses greater than 1 μm can be grown in 24 h if the concentration of DM is greater than 1 mM.

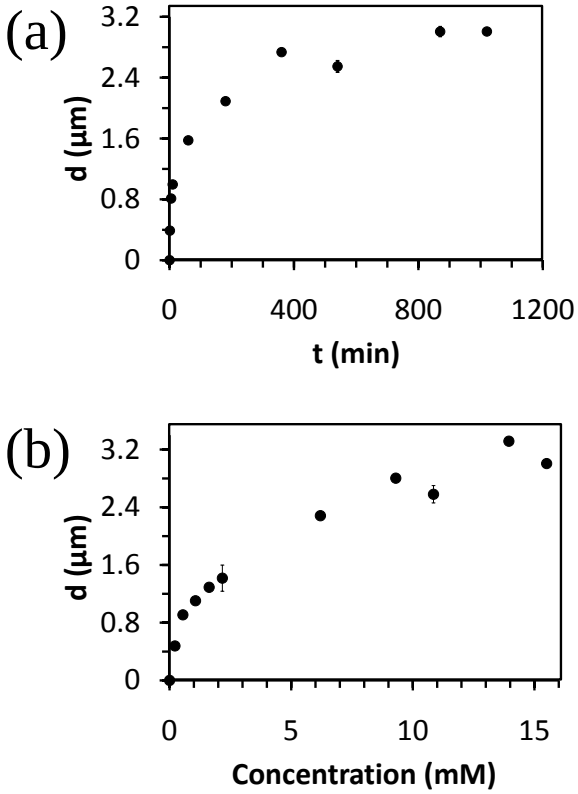

Figure 4.2. Thickness of PM films grown from HB+Ag/Au surfaces as affected by (a) time of polymerization after exposure to a 15 mM solution of DM at -17° C and (b) DM concentration (0.2 to 15 mM) after 24 h of reaction at -17° C. The data points and error bars represent the averages and standard deviations, respectively, of measurements obtained on two samples prepared independently.

Film Composition and Structure

We used RAIRS to assess the composition and structure of polymer films grown by SIPM and enable comparison with PM films formed by spontaneous polymerization (controls) that have been characterized previously.[13,23] We first exposed a HB+Au surface to an 8.5 mM solution of DM in ether for 1 h. RAIR spectra of the film (Figure 4.3) show the relevant regions of PM: CH_2 stretching[38,39] (ν_{as} = 2918 cm^{-1}, ν_s = 2850 cm^{-1}), CH_2 bending[12,13,54] (ν_{as} = 1473 cm^{-1}, ν_s = 1463 cm^{-1}), and CH_2 rocking modes[12,13,54,55] (split: ν_{as} = 730 cm^{-1} and ν_s = 720 cm^{-1}). The position of these modes are consistent with crystalline PM chains, and the absence of methyl modes in the IR spectra at 2960 and 2880 cm^{-1} indicates the linear character of the PM chains.[1]

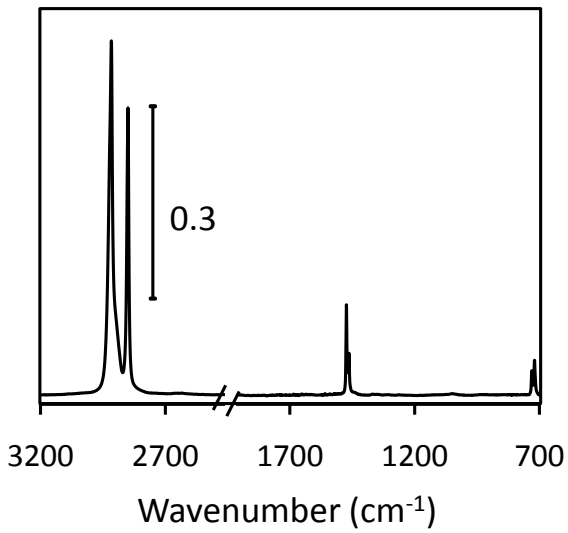

Figure 4.3. RAIR spectrum for a PM film after 1 h of polymerization in a 8.5 mM solution of DM in ether for 1 h.

To further evaluate the structure of PM films, we exposed the same six substrates listed in Table 4.1 to a 13 mM solution of DM in ether for 24 h and collected RAIR spectra. Figure 4.4 shows the relevant regions of the RAIR spectra for CH_2 bending[12,13,54] and CH_2 rocking modes.[12,13,54,55] Comparison of the RAIR peak absorbance (Figure 4.4a) for the various surfaces supports thickness measurements and shows that SIPM enables the formation of PM films. Figure 4.4 also provides information on the structure and conformation of PM films on HB+Au and HB+Ag/Au surfaces.

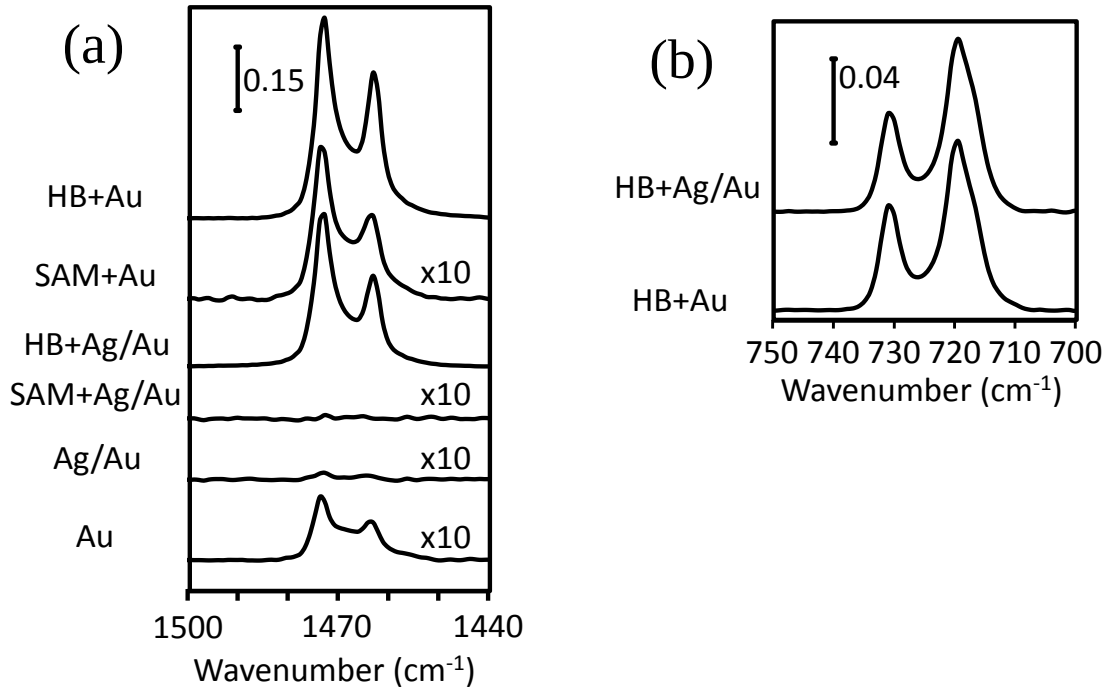

Figure 4.4. RAIR spectra for PM films grown by exposure to a 13 mM solution of DM in ether for 24 h. (a) CH bending region of PM films grown from the same six substrates listed in Table 4.1, with four of the spectra multiplied by 10 to enable comparison with spectra for thicker PM films grown from HB+Au and HB+Ag/Au (b) CH rocking region for PM films grown from Ag/Au and Au surfaces. The spectra have been offset vertically for clarity.

Figure 4.4a shows the CH bending region for PM films on HB+Ag/Au and HB+Au. The split character of the peak into asymmetric (ν_{as} =1473 cm^{-1}) and symmetric (ν_s =1463 cm^{-1}) modes indicates that there are two types of chain configurations in the unit subcell,[56] a prime characteristic of orthorhombic chain packing. In agreement with the orthorhombic conformation, the CH rocking mode also splits into in-phase and out-of-phase modes[13] at 731 and 719 cm^{-1} (Figure 4.4b), respectively. If we assume that the orthorhombic conformation is the only crystalline structure present and the rest of the chains have no conformational order,[13] we can estimate an orthorhombic crystalline content of ~70% for the HB+Au and HB+Au/Ag surfaces. This calculation uses the theoretical consideration for paraffins where the ratio of the rocking intensities I_{720} / I_{730} = 1.233.[55] Spectra (not shown) obtained after exposure of a HB+Si surface to a 13 mM solution of DM in ether at -17°C for 24 h are similar to those shown in Figure 4.4.

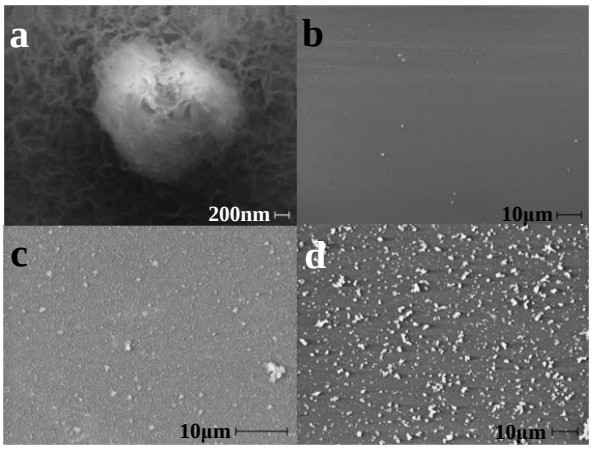

Figure 4.5. Scanning electron microscopy of PM films grown from HB+Si (a,b), HB+Ag/Au (c), and HB+Au (d) upon exposure to a 13 mM solution of DM in ether at -17 °C for 24 h.

Surface Topography

Figure 4.5 shows scanning electron microscopy (SEM) images to reveal the distinctive topographical features for PM films grown from HB+Si, HB+Au, and HB+Ag/Au surfaces after 24 h of reaction in a 13 mM solution of DM in ether at -17°C. Figure 4.5a presents a PM film grown from HB+Si showing nanometer scale ridges and valleys and a micron-scale cluster that is characteristic of PM films grown from SIPM. Comparison of PM films grown from HB+Si, HB+Ag/Au, and HB+Au surfaces (Figures 4.5b, c and d) show that the main topographical difference of the three substrates is related to the concentration of the micron-scale clusters, with films grown from HB+Si providing the least concentrated clusters on the surface and those on HB+Au the most concentrated clusters. To confirm that PM clusters result from the SIPM, we compared SEM images for films with no additional treatment after extraction from the DM solution and films that were vigorously rinsed with trichlorobenzene and ethanol after polymerization. Rinsing the films removed some large agglomerates (>5 μm in diameter), but the ~1 μm PM clusters remained firmly attached to the surface. These clusters survive AFM scanning (see Figure 4.6), and their mountain-like morphology (Figure 4.5a or 4.6a) suggests they are produced from the surface-initiated polymerization.

Finally, to more accurately determine the dimensions of the topographical features of PM films via SIPM, Figure 4.6 presents an atomic force microscopy (AFM) 3D representation of the HB+Au surface after 24 h of reaction in a 13 mM solution of DM in ether at -17 °C. Figure 4.6a shows that the PM film contains micro-scale features as high as ~1 μm rising above a base with nano-scale features. For the latter type of

features, Figure 4.6b presents a clearer representation to verify that the differences in height are below 200 nm. Both SEM and AFM images of the PM films show that its topography is rough on multiple scales and as shown below in this article, the rich topographic characteristics of the surface yield extreme behavior when the surface is in contact with water.

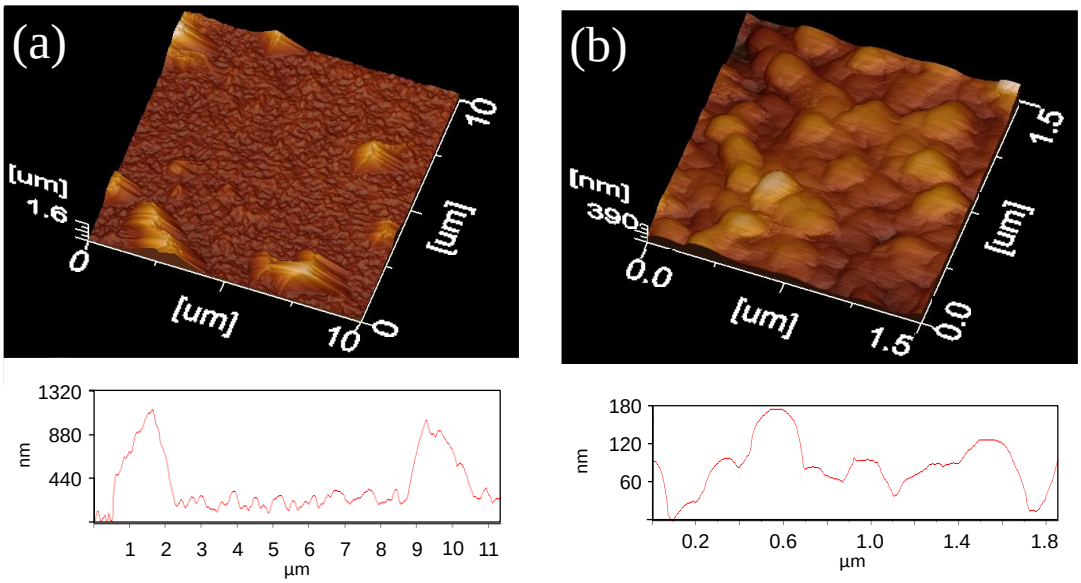

Figure 4.6. Tapping mode AFM images that show (a) micro-scale and (b) nano-scale features of PM films prepared by exposure of HB+Au to a 13 mM solution of DM in ether at -17 °C for 24 h. (b) was acquired using a higher definition scan within the area of (a). Line scans represent the topographical features for a diagonal line across the image from the bottom left to the top right in the image.

Surface Wettability

Table 4.2 shows the advancing (θ_A) and receding (θ_R) water contact angles for the same PM films grown for 24 h on HB+Au, HB+Ag/Au, and HB+Si and used in SEM characterizations. PM films on all substrates present advancing contact angles greater than 160°, and differences between θ_A and θ_R, known as hysteresis, of 2°, 13°, and 39°

for the HB+Au, HB+Ag/Au, and HB+Si surfaces, respectively. In the case of PM films grown from HB+Au, the film presents the characteristics of a superhydrophobic film (θ_A >150°, $\theta_A - \theta_R$ <10°)[57,58] and enables impinging water drops to easily rebound from the surface without suffering noticeable shape deformation. HB+Ag/Au and HB+Si surfaces also present superhydrophobic behavior after 72 and 120 h of reaction, respectively, consistent with an increase in the number of micro-scale features as polymerization proceeds.

Table 4.2. Water contact angles for PM films grown from HB+Au, HB+Ag/Au and HB+Si surfaces after 24 h of polymerization in a 13 mM solution of DM in ether at -17 °C for 24 h.

Substrate	θ_A (°)	θ_R (°)
HB+Au	167 +/- 2	165 +/- 1
HB+Au/Ag	162 +/- 3	149 +/- 6
HB+Si	160 +/- 2	121 +/- 3

The behavior of the advancing contact angle (θ_A) for PM films grown from SIPM represents a substantial difference as compared to smooth PM surfaces (~103°).[13] Several authors[57,59,60] have shown that the film topography is responsible for the elevation of contact angles and the diminution of hysteresis, and surface roughness has been directly or indirectly included in the Wenzel and the Cassie contact angle models. Here, to analyze the wetting behavior of PM films grown by SIPM, we classify them depending on whether they follow the Cassie or the Wenzel state. Films in the Cassie state exhibit large contact angles and low hystereses,[57,58] which is the case for contact angles on PM films grown from HB+Au and HB+Ag/Au surfaces. For PM films grown from HB+Si,

we observe that θ_A is similar to contact angles for PM films grown from HB+Au and HB+Ag/Au surfaces, and hence, the water drops advance in the Cassie state for all three films. For the case of θ_R for PM films grown from HB+Si, we first use Equation 2.6 to calculate an r_c value of 2.9, assuming that $\phi_{PM} << 1$.[58] Then, we calculate the roughness ratio of the surface as 2.3 with Equation 2.2, which, as compared[61] to r_c, suggests that after advancing in the Cassie state the drop collapses into the Wenzel state upon receding. After using Equation 2.4 and the θ_R for PM films grown from HB+Au and HB+Ag/Au surfaces, we estimate that less than 5% and 19%, respectively, of the area of the drop at the interface is in contact with PM.

The surface topography of the films influences the behavior of water droplets on the surface. Gao and McCarthy[60] showed that introduction of nano-scale roughness to an originally microscale-rough surface decreased the surface hysteresis from 20° to ~0°. Here, we observe from SEM images that an increase in the concentration of micro-scale features (HB+Au> HB+Ag/Au> Si+Au) decreases hysteresis (HB+Au< HB+Ag/Au< Si+Au), thus, increasing the stability of the drop in the Cassie state[57] and enabling the drops to easily rebound from the surface.[62] PM films grown from SIPM exhibit superhydrophobic behavior after times of polymerization that enable the growth of a sufficient number of micron-scale features that provides stability of the drops in the Cassie state, with times ranging from 24, 72 and 120 h for HB+Au, HB+Ag/Au, and HB+Si surfaces, respectively. In summary, these results suggest that SIPM enables the preparation of PM films with high contact angles (>150°) due to the pervasive presence of nano-scale ridges/valleys and that an increase of the isolated micro-scale features decreases hysteresis, enabling the preparation of superhydrophobic PM films.

Scheme 4.2. Equivalent circuit model used to represent electrochemical impedance spectra for PM films. Components of the circuit: R_s: resistance of the solution, C_i: capacitance of the interface, R_i: resistance of the interface, C_f: capacitance of the film, R_f: resistance of the film.

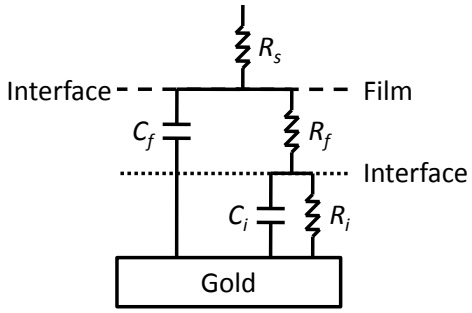

Barrier Properties

The remarkable hydrophobic character of SIPM films due to the presence of air at the polymer/water interface opens the door to a diverse number of applications in which minimizing the contact between water and a substrate is critical. One of those applications is the protection of substrates using polymer coatings where the protective coating serves as a barrier to substances that can react and degrade the substrate interface. To investigate the effect that trapped air at the polymer/water interface has on the barrier properties against redox probes, we characterized PM films with electrochemical impedance spectroscopy (EIS) in the presence of 1 mM $K_3Fe(CN)_6$, 1 mM $K_4Fe(CN)_6 \cdot 3H_2O$, and 0.1 M Na_2SO_4(aq). EIS enables a comparison of the effective thickness and blocking properties of SIPM films (HB+Ag/Au, HB+Au) in relation to smoother PM films grown from non-polymethylenated surfaces (Au, Ag/Au, SAM+Ag/Au, SAM+Au) after 24 h of exposure to a 13 mM solution of DM at -17°C. Comparison of the barrier properties depends on the ability to fit any resultant impedance

spectrum to an equivalent circuit model composed of capacitors and resistors. Scheme 4.2 presents the general circuit model of a metal surface covered by a polymer film.[2,63] In this model, both the film and the organic/metal interface contribute to the total impedance. This model may be simplified based on the relative values of each circuit component. For example, if the resistance of the film (R_f) is much larger than the interfacial impedance (defined as the parallel contribution of the interfacial capacitance (C_i) and resistance (R_i)), the spectrum will only exhibit a single time constant that is representative of the film (Randles model). Figure 4.7 shows the Bode plot and the phase angle behavior of the experimental results with fits by a Randles[63] equivalent circuit model as solid lines. Table 4.3 lists the capacitance and resistance of the films that were quantified by fits to experimental data.

EIS results show that after exposure to DM, Ag/Au surfaces (Ag/Au, SAM+Ag/Au) exhibit Warburg behavior (W) characteristic of uncoated metallic surfaces, indicating that little if any PM is grown on the surface.[64] In the case of Au surfaces (Au, SAM+ Au), their exposure to DM enables the growth of PM films having impedances that follow the Randles model and that exhibit well defined resistances at low frequencies as the redox probes begin to penetrate the film. In contrast, films grown from the SIPM process show no signs of a resistive plateau ($R_f > 1\times10^{10}$ $\Omega\bullet cm^2$) at low frequencies but a linear increase of the log impedance with decreasing log frequency, with a slope of -1, reflecting ultrahigh impedance against the transfer of redox probes. The phase angle (ϕ) behavior in Figure 4.7b shows the balance between purely capacitive ($\phi = -\pi/2$) and purely resistive ($\phi = 0$) behavior and the higher sensitivity of ϕ versus $|Z|$ to measure breakdowns in the protection by the film.[65] The results agree with those of Figure 4.7a

and more importantly, the fact that the superhydrophobic film grown from HB+Au displays a purely capacitive behavior ($\phi = -\pi/2$) for all frequencies indicates perfect barrier performance. The PM film grown from HB+Ag/Au (θ_A/θ_R=162°/149°) shows a slight increase in ϕ at low frequency, consistent with the onset of penetration by redox probes and highlighting the role of superhydrophobicity in the ability of the film to perfectly block redox probes from the substrate.

Tremendous differences in barrier properties between PM films grown from SIPM versus spontaneous DM polymerization could, at first sight, be attributed to differences in thickness. However, to determine the effect of superhydrophobicity on the barrier properties of PM films grown on Au from SIPM, we collected the impedance spectrum of a PM film under superhydrophobic and non-superhydrophobic conditions. To achieve superhydrophobic conditions, we used the aqueous redox solution mentioned above. For non-superhydrophobic conditions, we collected a new spectrum after decreasing the surface tension of the previous solution by adding sodium dodecyl sulfate (SDS, 2 × CMC = 16 mM).[66] Figure 4.8 shows a Bode magnitude plot of the resulting spectra and their fits as solid lines for a PM film grown from SIPM and as a control, a self-assembled monolayer (SAM) prepared from n-octadecanethiol both with and without surfactant. We selected a SAM as a control due to its molecularly smooth surface and inability to entrap much air at the organic/aqueous interface.

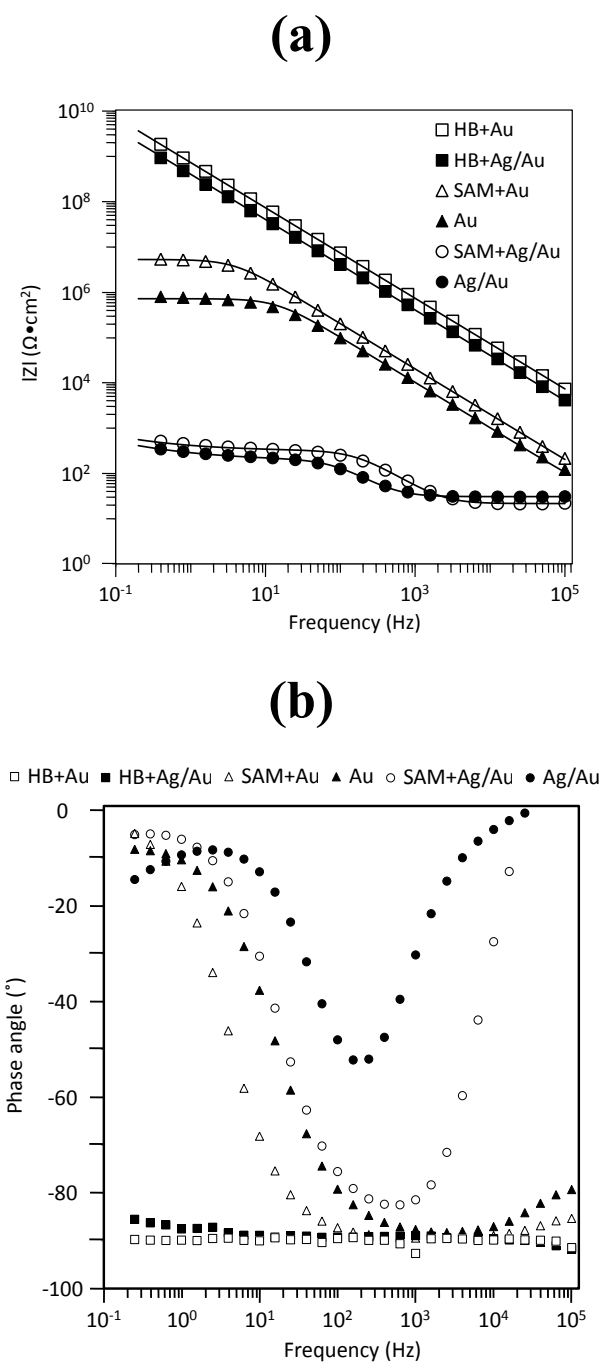

Figure 4.7. Electrochemical impedance spectra (a) and phase angle behavior (b) for PM films grown by exposure of various surfaces to a 13 mM solution of DM in ether at -17 °C for 24 h. Surfaces include two hydroborated SAMs, one on gold (HB+Au) and another on Ag/Au UPD (HB+Ag/Au), two vinyl-terminated SAMs not exposed to borane (SAM+Au, SAM+Ag/Au), as well as a Au and a Ag/Au surfaces. 1 mM solutions of $K_3Fe(CN)_6$ and $K_4Fe(CN)_6$ were used as soluble probes in a 0.1 M $NaSO_4$(aq) solution.

Table 4.3. Film resistance (R_f), capacitance (C_f) and thicknesses (d) for PM films grown from the indicated surfaces upon exposure to a 13 mM solution of DM in ether at -17 °C for 24 h.

	Ag/Au	SAM+Ag/Au	Au	SAM+Au	HB+Ag/Au	HB+Au
d (nm)[a]	6	1	228	315	3006	3554
R_f (Ω)	-	-	7.2×10^5	5.3×10^6	$>1 \times 10^{10}$	$>1 \times 10^{10}$
C_f (F)	-	-	1.6×10^{-8}	7.8×10^{-9}	3.9×10^{-10}	2.2×10^{-10}
R_i(Ω)	1.7×10^2	3.0×10^2	-	-	-	-
C_i (F)	1.1×10^{-5}	3.3×10^{-6}	-	-	-	-
W ($s^{1/2}/\Omega$)	3.6×10^{-3}	3.1×10^{-3}	-	-	-	-

[a] Average thickness calculated from the values of Table 4.1.

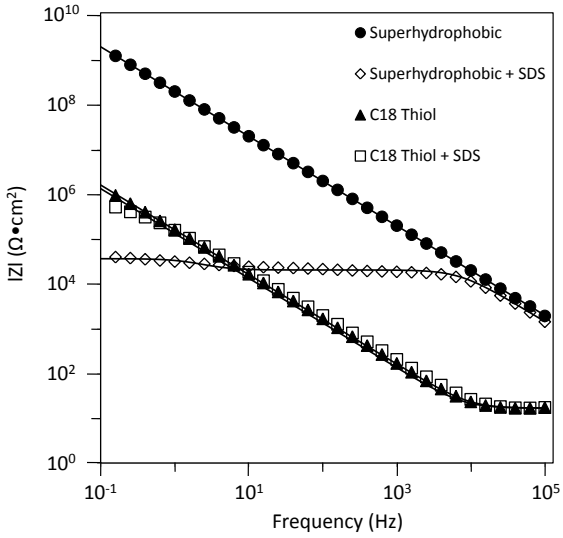

Figure 4.8. Change in the electrochemical impedance spectra for a superhydrophobic PM film (1.6 μm thick) grown from HB+Au after addition of SDS (~16 mM) to the aqueous solution of 1 mM $K_3Fe(CN)_6$ and $K_4Fe(CN)_6$ and 0.1 M $NaSO_4$. A self-assembled monolayer (SAM) on Au prepared from n-octadecanethiol both with and without surfactant served as a control.

The superhydrophobic PM film behaves as an ideal capacitor that provides a defined separation of charge between the solution and the metal substrate due to the combined presence of air and PM as dielectric materials. However, addition of the surfactant breaks the superhydrophobic behavior,[66,67] favoring the displacement of the air in the grooves of the interface by the aqueous solution with reduced surface tension. This effect on the wetting properties (θ_{SDS} = 75 ± 5° static contact angle of a ~16 mM SDS (aq) solution on PM) results from the alteration of the interfacial tension of water after the surfactant molecules adsorb at the liquid-solid and liquid-gas interfaces.[68] The dramatic 10^5 Ω•cm^2 fold difference between these spectra at low frequencies (10^{-1} Hz) represents the magnitude of the superhydrophobic effect in maximizing the barrier properties. These results agree with those reported by Yin[69,70] and Liu[71], in which high water contact angles (~150°) of a surface coating correlated with reduced degradation of the metal substrate in the presence of corrosive environments. Here, however, for the first time, we have quantified the effect that superhydrophobicity has on the barrier properties as compared to non-superhydrophobic films of the same characteristics. In relation to the electrochemical behavior of SDS, Wang et al.[72] showed that organization of SDS at the interface decreases the passage of current in a cyclic voltammogram for a methyl-terminated SAM. To determine the implications of having SDS in solution, and as a manner of control, Figure 4.8 shows how the resultant spectra of a densely packed SAM before and after exposure to the surfactant exhibit little change in the electrochemical properties, suggesting that the substantial decrease in the barrier properties of the superhydrophobic film is not due to any electrochemical effect of the surfactant, but rather to the penetration of the solution through the grooves of the film.

This argument is supported by the fact that the resistance for the PM film in the presence of SDS is lower than the resistance offered by the densely packed SAM that is only 2.5 nm thick. These results suggest that the PM film contains a topology that enables either the entrapment of air or the penetration of aqueous solution into the film when it is exposed to solutions of high or low surface tensions, respectively.

Conclusion

We have developed a new strategy to produce polymethylene films on gold and silicon surfaces by immobilizing borane on a vinyl-terminated monolayer, followed by its exposure to a DM solution in ether. This approach enables the control of film thickness by varying the time of polymerization or the DM concentration to produce PM films with superhydrophobic behavior and outstanding barrier properties. This methodology of creating a superhydrophobic surface from an originally smooth surface has the versatility to be further extended to many other vinyl-terminated surfaces.

PM films grown from SIPM present a micron- and nano-scale morphology that is responsible for their superhydrophobic behavior. This morphology leads to entrapped air at the polymer/aqueous interface, which elevates both advancing and receding contact angles, and enhances aqueous-phase barrier properties by orders of magnitude. This remarkable improvement in the barrier properties, combined with the precise control over film properties and the ability to generate superhydrophobic films, could open the door to a broad number of applications in which highly blocking surface coatings are required.

References

(1) Bai, D.; Jennings, G. K. *Journal of the American Chemical Society* **2005**, *127*, 3048-3056.

(2) Bai, D. S.; Ibrahim, Z.; Jennings, G. K. *Journal of Physical Chemistry C* **2007**, *111*, 461-466.

(3) Zhao, M. Q.; Zhou, Y. F.; Bruening, M. L.; Bergbreiter, D. E.; Crooks, R. M. *Langmuir* **1997**, *13*, 1388-1391.

(4) Huang, W. X.; Kim, J. B.; Bruening, M. L.; Baker, G. L. *Macromolecules* **2002**, *35*, 1175-1179.

(5) Prucker, O.; Ruhe, J. *Macromolecules* **1998**, *31*, 602-613.

(6) Prucker, O.; Ruhe, J. *Macromolecules* **1998**, *31*, 592-601.

(7) Boyes, S. G.; Brittain, W. J.; Weng, X.; Cheng, S. Z. D. *Macromolecules* **2002**, *35*, 4960-4967.

(8) Weck, M.; Jackiw, J. J.; Rossi, R. R.; Weiss, P. S.; Grubbs, R. H. *Journal of the American Chemical Society* **1999**, *121*, 4088-4089.

(9) Jordan, R.; Ulman, A.; Kang, J. F.; Rafailovich, M. H.; Sokolov, J. *Journal of the American Chemical Society* **1999**, *121*, 1016-1022.

(10) Jordan, R.; Ulman, A. *Journal of the American Chemical Society* **1998**, *120*, 243-247.

(11) Jennings, G. K.; Brantley, E. L. *Advanced Materials* **2004**, *16*, 1983-1994.

(12) Guo, W. F.; Jennings, G. K. *Langmuir* **2002**, *18*, 3123-3126.

(13) Seshadri, K.; Atre, S. V.; Tao, Y. T.; Lee, M. T.; Allara, D. L. *Journal of the American Chemical Society* **1997**, *119*, 4698-4711.

(14) Ruckenstein, E.; Li, Z. F. *Advances in Colloid and Interface Science* **2005**, *113*, 43-63.

(15) Edmondson, S.; Osborne, V. L.; Huck, W. T. S. *Chemical Society Reviews* **2004**, *33*, 14-22.

(16) Shea, K. J.; Staiger, C. L.; Lee, S. Y. *Macromolecules* **1999**, *32*, 3157-3158.

(17) Shea, K. J.; Walker, J. W.; Zhu, H.; Paz, M.; Greaves, J. *Journal of the American Chemical Society* **1997**, *119*, 9049-9050.

(18) Busch, B. B.; Paz, M. M.; Shea, K. J.; Staiger, C. L.; Stoddard, J. M.; Walker, J. R.; Zhou, X. Z.; Zhu, H. D. *Journal of the American Chemical Society* **2002**, *124*, 3636-3646.

(19) Busch, B. B.; Staiger, C. L.; Stoddard, J. M.; Shea, K. J. *Macromolecules* **2002**, *35*, 8330-8337.

(20) Peanasky, J. S.; McCarley, R. L. *Langmuir* **1998**, *14*, 113-123.

(21) Davies, A. G.; Hare, D. G.; Khan, O. R.; Sikora, J. *Journal of the American Chemical Society* **1963**, 4461-4471.

(22) Davies, A. G.; Hare, D. G.; Khan, O. R.; Sikora, J. *Proceedings of the Chemical Society* **1961**, 172.

(23) Guo, W. F.; Jennings, G. K. *Advanced Materials* **2003**, *15*, 588-591.

(24) James, M. *Polymer Data Handbook* Oxford University Press: New York, 1999.

(25) Brandrup, J.; Immergut, E. H.; Grulke, E. A.; Abe, A.; Bloch, D. R. *Polymer Handbook*; 4th ed.; Wiley & Sons: New York, 1999.

(26) Kong, J.-S.; Lee, D.-J.; Kim, H.-D. *Journal of Applied Polymer Science* **2001**, *82*, 1677-1690.

(27) Lie, L. H.; Patole, S. N.; Hart, E. R.; Houlton, A.; Horrocks, B. R. *The Journal of Physical Chemistry B* **2002**, *106*, 113-120.

(28) Kubota, H.; Morawetz, H. *Journal of Polymer Science Part A-1: Polymer Chemistry* **1967**, *5*, 585-591.

(29) Bart, J. C.; Cariati, F.; Erre, L.; Gessa, C.; Micera, G.; Piu, P. *Clays and Clay Minerals* **1979**, *27*, 429-432.

(30) Brown, H. *Boranes in Organic Chemistry*; Cornell University Press: Ithaca, 1972.

(31) Brown, H. C.; Rao, B. C. S. *Journal of the American Chemical Society* **1959**, *81*, 6428-6434.

(32) Onak, T. *Organoborane Chemistry*; Academic Press: New York, 1975.

(33) Ulman, A. *Chemical Reviews* **1996**, *96*, 1533-1554.

(34) Mirviss, S. B. *Journal of the American Chemical Society* **1961**, *83*, 3051-3056.

(35) Mirviss, S. B. *Journal of Organic Chemistry* **1967**, *32*, 1713-&.

(36) Davies, A. G. *Journal of Chemical Research-S* **2008**, 361-375.

(37) Brown, H. C.; Midland, M. M. *Tetrahedron* **1987**, *43*, 4059-4070.

(38) Snyder, R. G.; Strauss, H. L.; Elliger, C. A. *Journal of Physical Chemistry* **1982**, *86*, 5145-5150.

(39) Sulc, R.; Zhou, X. Z.; Shea, K. J. *Macromolecules* **2006**, *39*, 4948-4952.

(40) Shurvell, H. F.; Faniran, J. A. *Canadian Journal of Chemistry* **1968**, *46*, 2082.

(41) Faniran, J. A.; Shurvell, H. F. *Canadian Journal of Chemistry* **1968**, *46*, 2089-&.

(42) Bradshaw, A. M.; Richardson, N. V. *Pure and Applied Chemistry* **1996**, *68*, 457-467.

(43) Barriet, D.; Yam, C. M.; Shmakova, O. E.; Jamison, A. C.; Lee, T. R. *Langmuir* **2007**, *23*, 8866-8875.

(44) Brewer, S. H.; Allen, A. M.; Lappi, S. E.; Chasse, T. L.; Briggman, K. A.; Gorman, C. B.; Franzen, S. *Langmuir* **2004**, *20*, 5512-5520.

(45) Brown, H. C.; Dodson, V. H. *Journal of the American Chemical Society* **1957**, *79*, 2302-2306.

(46) Mikhailov, B. M.; Bubnov, Y. *Organoboron Compounds in Organic Synthesis*; Harwood Academic: New York, 1984.

(47) Bain, C. D.; Troughton, E. B.; Tao, Y. T.; Evall, J.; Whitesides, G. M.; Nuzzo, R. G. *Journal of the American Chemical Society* **1989**, *111*, 321-335.

(48) *Ulvac-PHI, Inc. (2007). Operator's PHI Multipak software manual, version 8.2C.* ; Ulvac-PHI, Inc.: Chigasaki City, Kanagawa Prefecture, Japan

(49) Carey, R. I.; Folkers, J. P.; Whitesides, G. M. *Langmuir* **1994**, *10*, 2228-2234.

(50) Wasserman, S. R.; Tao, Y. T.; Whitesides, G. M. *Langmuir* **1989**, *5*, 1074-1087.

(51) Faucheux, N.; Schweiss, R.; Lutzow, K.; Werner, C.; Groth, T. *Biomaterials* **2004**, *25*, 2721-2730.

(52) *Guide to using WVASE32 Software for spectroscopic ellipsometry data acquisition and analysis, Revised January 1, 2001 Version 3.335*; J.A. Woollam Co., Inc. .

(53) Brunner, H.; Vallant, T.; Mayer, U.; Hoffmann, H. *Surface Science* **1996**, *368*, 279-291.

(54) Colthup, N.; Daly, L.; Wiberley, S. *Introduction to infrared and Raman spectroscopy*; 3 ed.; Academic Press: Boston, 1990.

(55) Snyder, R. G. *Journal of Chemical Physics* **1979**, *71*, 3229-3235.

(56) Snyder, R. G. *Journal of Molecular Spectroscopy* **1961**, *7*, 116-144.

(57) Zhu, L. B.; Xiu, Y. H.; Xu, J. W.; Tamirisa, P. A.; Hess, D. W.; Wong, C. P. *Langmuir* **2005**, *21*, 11208-11212.

(58) Callies, M.; Quere, D. *Soft Matter* **2005**, *1*, 55-61.

(59) Nosonovsky, M. *Langmuir* **2007**, *23*, 3157-3161.

(60) Gao, L. C.; McCarthy, T. J. *Langmuir* **2006**, *22*, 2966-2967.

(61) Bittoun, E.; Marmur, A. *Journal of Adhesion Science and Technology* **2009**, *23*, 401-411.

(62) Chen, W.; Fadeev, A. Y.; Hsieh, M. C.; Oner, D.; Youngblood, J.; McCarthy, T. J. *Langmuir* **1999**, *15*, 3395-3399.

(63) Brantley, E. L.; Holmes, T. C.; Jennings, G. K. *Journal of Physical Chemistry B* **2004**, *108*, 16077-16084.

(64) Brantley, E. L.; Jennings, G. K. *Macromolecules* **2004**, *37*, 1476-1483.

(65) Bard, A.; Faulkner, L. *Electrochemical Methods*; 2nd ed.; Jhon Wiley and sons, 2001.

(66) Mohammadi, R.; Wassink, J.; Amirfazli, A. *Langmuir* **2004**, *20*, 9657-9662.

(67) Ferrari, M.; Ravera, F.; Rao, S.; Liggieri, L. *Applied Physics Letters* **2006**, *89*.

(68) Feng-Ming, C.; Yu-Jane, S.; Hui, C.; Heng-Kwong, T. *Applied Physics Letters* **2007**, *91*, 094108.

(69) Liu, T.; Chen, S.; Cheng, S.; Tian, J.; Chang, X.; Yin, Y. *Electrochimica Acta* **2007**, *52*, 8003-8007.

(70) Yin, Y. S.; Liu, T.; Chen, S. G.; Cheng, S. *Applied Surface Science* **2008**, *255*, 2978-2984.

(71) Liu, H. Q.; Szunerits, S.; Xu, W. G.; Boukherroub, R. *Acs Applied Materials & Interfaces* **2009**, *1*, 1150-1153.

(72) Wang, J.; Zeng, B.; Fang, C.; Zhou, X. *Journal of Electroanalytical Chemistry* **2000**, *484*, 88-92.

CHAPTER V

EFFECT OF SUPERHYDROPHOBICITY ON THE BARRIER PROPERTIES OF POLYMETHYLENE FILMS

Introduction

Polymer coatings are essential in the protection of substrates against environmental conditions that degrade them and limit their performance. Effective blocking of the surface depends on the characteristics of the film such as its thickness,[1,2] adhesion to the substrate,[3] presence of additives,[1] and its permeability towards water, ions and certain gases.[1] From all these variables, the most common way to enhance the barrier properties of the coating is by increasing the thickness of the film, meaning that the unwanted species present in the outer environment would have to diffuse over greater distances to reach the underlying substrate. Recently, superhydrophobic (SH) surfaces (θ_A >150°, $\theta_A - \theta_R$ <10°)[4,5] have been used to not only combine the barrier properties of dielectric materials but also exploit their rich topographic characteristics to minimize the contact area between the outer aqueous solution and the polymer film, resulting in the entrapment of air between the aqueous and polymer phases. Using this strategy, films that exhibit high water contact angles (θ_A > 150°) on metal substrates such as copper, aluminum, titanium or zinc have exhibited reductions in the corrosion current density[6-12] on the order of two to four orders of magnitude when compared to the unmodified metal, as well as increases in the impedance of the system by two orders of magnitude.[6,7] These results show the tremendous potential of this strategy to offer protection to the underlying

substrate. However, these studies do not report the receding contact angle (θ_R) of the surfaces, one of the wetting characteristics of the film that defines whether the film is truly in the SH state. In addition, these studies reference the behavior of the protective polymer film to that of the bare substrate, a comparison that could be attributed solely to the low dielectric constant of the coating and not to the effect that the topography of the film has on its wetting properties. Employment of SH films in various areas, including the enhancement of barrier properties, has remarkable potential; thus, a diverse array of approaches[13-17] has been developed to fabricate SH films using a variety of materials on a broad number of substrates. However, to date, a quantification of the effect that the entrapped air has on the barrier properties exhibited by SH films has not been explored.

Here, we have studied the effect that entrapped air at the interface of a SH surface has on the enhancement of the barrier properties against the transport of aqueous redox probes. For this purpose, we exploit the SIPM described in Chapter IV to grow SH polymethylene (PM) films and use EIS to assess the barrier properties of the films. Due to the reduced contact area between the solution and the polymer film (~5% of the projected area of the surface, based on Equation 2.4), results from electrochemical impedance spectroscopy (EIS) show that these films present a capacitance comparable to that offered by either a smooth PM film that is 80% thicker, or a smooth film of a material with the same thickness and an effective dielectric constant (ε) of ~1.3. This result represents a tremendous enhancement in the barrier properties relative to a smooth PM film (ε_{PM} = 2.3)[18,19] since, instead of ε increasing towards the dielectric constant of water (ε_{Water} = 80)[20,21] as a common organic film would behave in the presence of an

aqueous solution,[22] ε of the film tends to that of air (ε_{Air} = 1).[23] As an integral tool to quantify the effect of entrapped air on the dielectric properties of SH films, we have used the Hemholtz theory to model the interface of a SH surface as a system of capacitors that account for both the entrapment of air and the effective separation between the solution and the substrate.

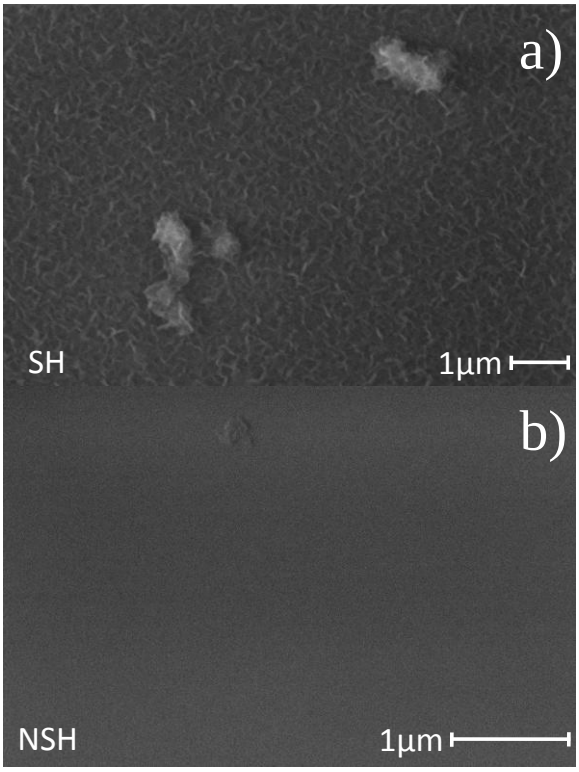

Figure 5.1. Scanning electron microscopy (SEM) images of a) SH and b) NSH PM films that are both 1.8 ± 0.1 µm in thickness and exhibit the properties summarized in Table 5.1.

Results and Discussion

Superhydrophobic vs Non-superhydrophobic PM Films

To determine the effect of superhydrophobicity on the barrier properties, we compared SH PM films to relatively smooth PM films of similar thickness that exhibit non-superhydrophobic (NSH) behavior. Fabrication of SH films results from the surface-initiated polymethylenation[24] (SIPM) approach developed in the previous chapter, in which exposure of immobilized borane groups to a solution of a DM in ether leads to the growth of PM films as thick as 3.6 μm after 24 h of reaction. To fabricate relatively smooth NSH PM films, we took advantage of the spontaneous decomposition of DM on catalytic surfaces, such as that of gold.[25] Film thickness using this approach reaches an asymptotic thickness in the order of a couple hundred of nanometers.[26] However, to obtain thicker films that are of comparable thickness to the SH PM films (< 1 μm), we altered the kinetics of film growth by atomically modifying the surface of gold by underpotential deposition (UPD) of copper prior to DM exposure.[26,27] Polymerization of SH and smooth NSH PM films were performed upon exposure to a 13 mM solution of DM in ether at -17 °C for 24 and 110 h, respectively. To characterize the SH and smooth NSH PM films, we measured both their wetting behavior in terms of the advancing (θ_A) and receding (θ_R) contact angles, as well as their distinctive topographical features using scanning electron microscopy (SEM) and atomic force microscopy (AFM).

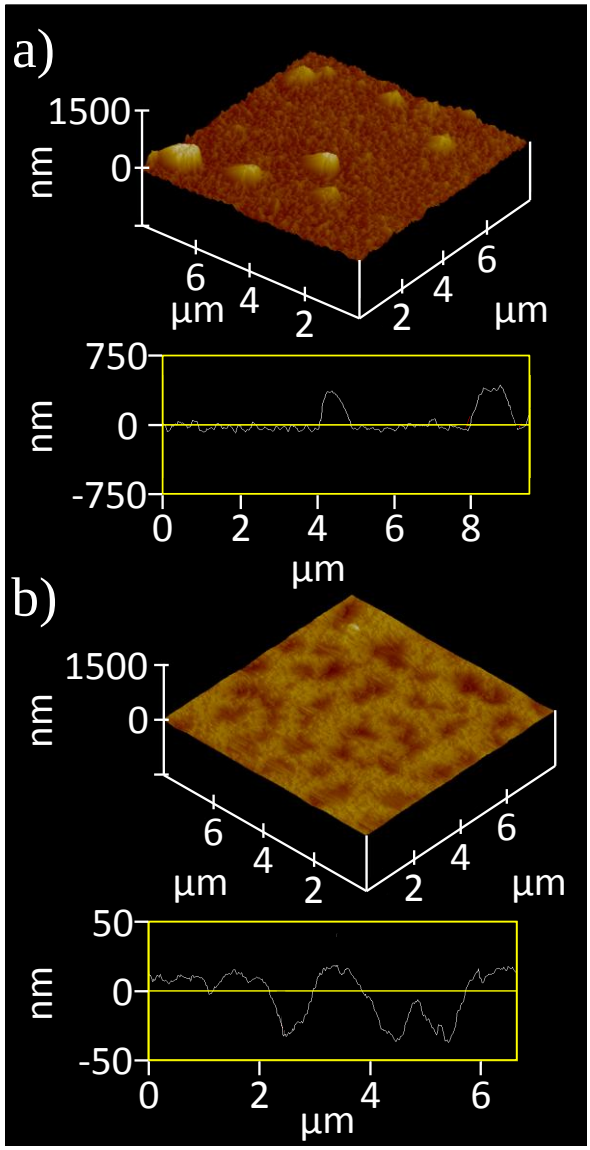

Figure 5.2. Atomic force microscopy (AFM) images of a) SH and b) NSH PM films that are both 1.8 ± 0.1 µm in thickness and exhibit the properties summarized in Table 5.1.

Table 5.1 shows that SH and NSH films exhibit different wetting properties, although the chemical composition of the films is the same[24,25] and their thicknesses are similar (1.8 ± 0.1). The NSH film investigated here exhibits higher advancing contact angles as compared to the reported values for smooth PM surfaces (103°),[25] suggesting

that this surface is in the Wenzel regime where the contacting water follows the contour of the PM surface, elevating the CA according to Equation 2.2. In contrast, the SH film, as reflected by its large advancing contact angle and low hysteresis,[5,15] behaves according to the Cassie regime where the contacting water drop is in contact with PM and air.[28] For the results presented in this study, the SH state is defined based not only on the wetting, but also on the electrochemical properties of the film that indicate the entrapment of air at the polymer/air interface, as will be discussed further in this manuscript.

Table 5.1. Contact angles, film resistance (R_f), capacitance (C_f), and thicknesses (d) for SH and NSH PM films that are both 1.8 ± 0.1 μm in thickness.

Film	$\theta_A(°)$	$\theta_R(°)$	$\cos\theta_R - \cos\theta_A$	$d(\mu m)$	R_f $(\Omega \bullet cm^2)$	C_f (F/cm^2)
SH	160 ± 1	152 ± 2	0.06	1.7	$>1 \times 10^9$	6.55×10^{-10}
NSH	111 ± 2	75 ± 2	0.62	1.9	1.89×10^6	2.28×10^{-9}

These remarkable differences in the wetting behavior between SH and NSH PM films are attributed to substantial differences in the topography of each surface as shown by SEM and AFM images in Figure 5.1 and Figure 5.2, respectively. SH films exhibit a rich surface topography with steep nanometer scale ridges and valleys (100-200 nm in depth), as well as micron-scale clusters[24] responsible for their high contact angles and low hysteresis parameters. In contrast, NSH films present shallow valleys (<60 nm in depth) and lack distinct features that increase the roughness of the surface. Distinct nano-

and micron-scale topographical features present in SH films function as pillars to support water and provide the surface with SH behavior.

Scheme 5.1. Randles model used to represent electrochemical impedance spectra for PM films. Components of the circuit: R_s : resistance of the solution, C_f : capacitance of the film, R_f : resistance of the film.

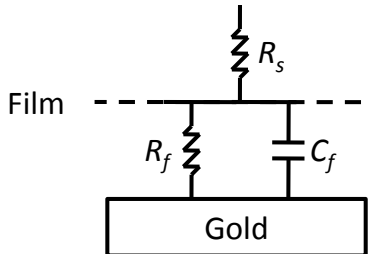

Effect of Superhydrophobicity on the Barrier Properties

To investigate the effect that the entrapped air at the polymer/solution interface has on the barrier properties, we characterized both NSH and SH PM films using electrochemical impedance spectroscopy (EIS). Analysis of the barrier properties results from modeling the impedance spectrum as an equivalent circuit model [24,29,30] composed of capacitive (C_f) and resistive (R_f) components. Scheme 5.1 shows the simplified circuit model of a metal surface covered by a polymer film,[29,30] in which the resistance offered by the film (R_f) is much larger than that offered by the organic metal interface (defined as the parallel contribution of the interfacial capacitance and resistance). Figure 5.3 compares, in the form of a Bode plot, the spectra collected for both SH and NSH PM films of similar thickness when exposed to a solution of 1 mM $K_3Fe(CN)_6$ and 1 mM $K_4Fe(CN)_6$ as redox probes in 0.1 M $NaSO_4$(aq). Fits of the experimental spectra are

shown as solid lines in Figure 5.3, and Table 5.1 lists the capacitance and resistance values calculated from fitting the equivalent circuit model.

EIS results show that the entrapped air at the polymer/solution interface of a SH film provides a remarkable enhancement of the barrier properties as compared to a NSH film. Figure 5.3 shows that both NSH and SH films are properly represented by a single-time-constant model.[30] In the case of the NSH film, the electrochemical behavior of the film shows a clear capacitive region at high to moderate frequencies where the film acts as a dielectric, and a resistive region at moderate to low frequencies to indicate the level of resistance (10^6 $\Omega \cdot cm^2$) against the transfer of redox probes. In contrast, the electrochemical behavior of the SH film behaves not only as a pure capacitor[24,31] in the entire frequency window shown in Figure 5.3, but also, the impedance of the film is at least three times greater than that exhibited by the NSH film throughout the entire frequency range.

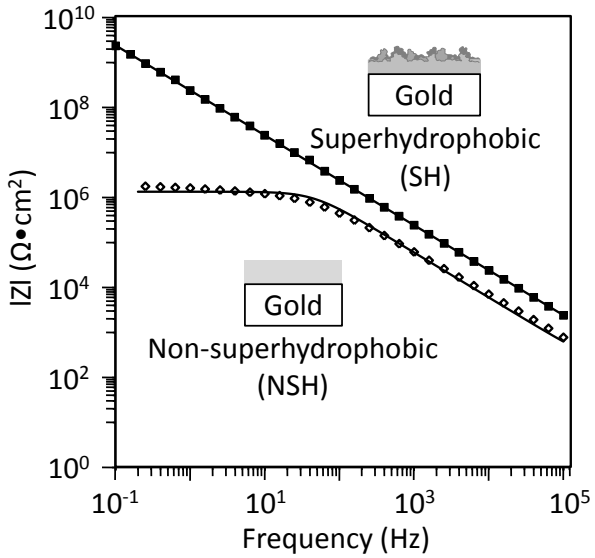

Figure 5.3. Electrochemical impedance spectra for a SH and a NSH PM films (1.8 ± 0.1 μm thick) in the presence of a solution of 1 mM $K_3Fe(CN)_6$ and 1 mM $K_4Fe(CN)_6$ as redox probes and 0.1 M $NaSO_4$ (aq). Lines represent fits of the spectra based on the model equivalent circuit in Scheme 5.1.

Examination of the capacitance exhibited by SH and NSH films (Table 5.1) in the context of the Helmholtz theory (vide infra) shows that their dielectric constants (ε) differ from that of PM ($\varepsilon = 2.3$). For NSH films, the ε (5.0) is higher than that of PM, suggesting incorporation of water (ε_{water} = 80),[20-22,32] into the film, [33,34] and for SH films, its ε (1.29) is much lower than that of PM, suggesting the incorporation of air ($\varepsilon_{Air} = 1$)[23] into the film. In addition to this result, Chapter IV[24] shows that after breaking the SH character of a PM film with the addition of surfactant to the EIS solution,[35,36] the film displays both a dramatic reduction of ~5 orders of magnitude in the impedance behavior at low frequencies and the behavior that is characteristic of a metal surface covered by a permeable polymer film.[22,30] These results suggest that the entrapped air at the polymer/solution interface of a SH film has a direct impact in the enhancement of the

barrier properties of the SH film by increasing the capacitive and resistive impedances of the film. Finally, we highlight that even under the EIS experimental conditions, that is 1 cm^2 of the SH film exposed to the aqueous solution, the film exhibits remarkable barrier properties against the transport of aqueous redox probes. The significance of this condition is that the effect of superhydrophobicity is maintained for an immersed area of the film whose radius is twice the capillary length of water (λ_C = 2.7 mm),[4] which is considered the upper size limit of a contacting droplet to neglect gravity effects that pull the droplet into a film of liquid.[4,37,38]

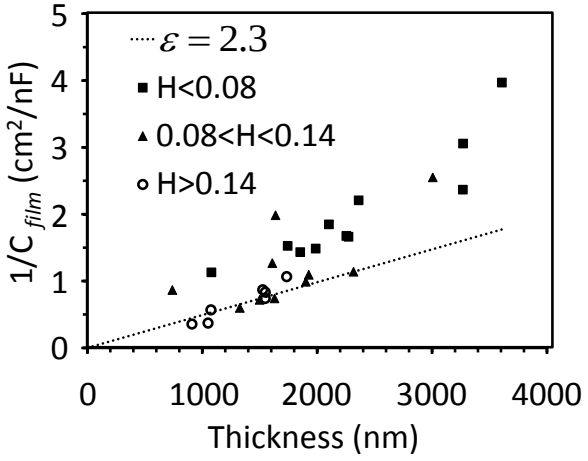

Figure 5.4. Variation of the inverse of capacitance for PM films with $\theta_A > 150°$ grown from SIPM with respect to their measured thicknesses. Experimental values are further classified depending on the hysteresis parameter of each film into $H < 0.08$, $0.08 < H < 0.14$, and $H > 0.14$ where $H = \cos\theta_R - \cos\theta_A$. The dashed line represents the expected dependency based on Helmholtz theory and assuming a ε of 2.3 for PM.

Analysis of the Capacitance in Terms of the Helmholtz Theory

SH PM films have proven to provide remarkable enhancement in barrier properties as compared to NSH films (Figure 5.3). To further analyze the effect of

superhydrophobicity on the dielectric properties, we modeled the PM film in the EIS experiment as an ideal capacitor using Helmholtz theory[33,39-42]

$$\frac{1}{C_{film}} = \frac{d_{effective}}{\varepsilon_0 \varepsilon_{effective}} \tag{5.1}$$

where C_{film} is the capacitance of the PM film per unit area, $\varepsilon_{effective}$ is the effective dielectric constant of the film, ε_0 is the dielectric constant of vacuum, and $d_{effective}$ the effective thickness of the film, defined as the separation distance between the electrolyte solution and the metal substrate. Applicability of the Helmholtz theory to this system is based on the assumption that the excess of charge on the metal substrate is at the polymer/metal interface and that the counter-charge in solution resides at the polymer/solution interface.[43] Figure 5.4 plots the experimental values for the inverse of capacitance ($1/C_{film}$) as a function of the measured thickness (d_{film}) for PM films with θ_A > 150° grown from SIPM after reacting in DM solutions with concentrations ranging from 0.2 – 15 mM and times ranging from 10 min to 36 h at -17 °C. Experimental results are also categorized in terms of the hysteresis parameter ($H = \cos\theta_R - \cos\theta_A$)[44,45] into three groups: $H < 0.08$, $0.08 < H < 0.14$, and $H > 0.14$. Without regard of the concentration, time of reaction or the hysteresis parameter, all the films exhibit a rough topology similar to that shown in Figure 5.1a and 5.2a. The dashed line is the expected behavior of $1/C_{PM}$ for a PM film based on the Helmholtz theory:

$$\frac{1}{C_{PM}} = \frac{d_{film}}{\varepsilon_0 \varepsilon_{PM}} \tag{5.2}$$

assuming a dielectric constant (ε_{PM}) of 2.3 that has been shown by others to represent HDPE (or chemically equivalent PM).[18,19]

Results in Figure 5.4 show that $1/C_{film}$ increases with the thickness of the film[39,40] and that a correlation exists between the hysteresis parameter and the ability to follow the predicted Helmholtz behavior for a PM film with $\varepsilon_{PM} = 2.3$. In the case of $H < 0.08$, the behavior of $1/C_{film}$ positively deviates at least 50% from the theoretical line, suggesting that the spatial distribution of micron-scale features, as well as the relative amount of both air and PM at the interface play an important role in the enhancement of the dielectric properties of the film. In the opposite case, films with $H > 0.14$ present a capacitive behavior that follows the Helmholtz predictions for a PM films with $\varepsilon_{PM} = 2.3$. Films with $0.08 < H < 0.14$ are in a transition regime in which they could exhibit deviations from the predicted $1/C$ for PM films according to the Helmholtz theory. According to this behavior, the entrapment of air at the polymer/water interface characteristic of the SH state will be defined not only by the wetting properties of the film ($\theta_A > 150°$,[4] $H < 0.14$), but also by the dielectric properties of the film such that $1/C$ is least 50% greater than the theoretical values calculated using d_{film} and $\varepsilon_{PM} = 2.3$. Otherwise, the films will be considered as NSH. Deviations of the dielectric and wetting properties from the behavior exhibited by smooth PM films illustrates the necessity to appropriately account for the presence of air at the interface when using SH films as barrier coatings.

To rationalize the different behavior exhibited by SH films from the theoretical values, we account for the trapped air at the polymer/water interface and for the presence

of micron-scale topographical features on SH films that could influence the effective separation as well as the effective dielectric constant of the medium between the solution and the substrate. Modeling the effect of superhydrophobicity on the dielectric properties is based on the assumption that, in these types of films, air is trapped in the grooves formed by micron-scale features located at the polymer/water interface as demonstrated by reflectometric[46] and spectroscopic[47] techniques. Here, we suggest that the air/PM composite interface of a SH surface exhibits both a lower dielectric constant ($\varepsilon_{effective}$) and greater metal/electrolyte separation distance ($d_{effective}$) (vide infra) as compared to a smooth PM film (ε_{PM}) of thickness d_{film}. This structural disposition of the film would result in capacitances for SH films lower than those for films that follow the theoretical predictions, in agreement with the results in Figure 5.4. We highlight the heterogeneous distribution of both the air and the PM in the film according to the nature of the SH phenomena and its distinct effect on ε, as compared to a possible random or homogeneous incorporation of the air into the film.[32,34,48] To address the role of superhydrophobicity on the capacitance, we envision the surface as a heterogeneous PM/air composite interface (Figure 5.5), assuming no swelling or solubilization of the polymer, and describing it as a circuit of capacitive elements representing the effect of air and PM. A similar approach was proposed by Conway and Pell[49,50] to represent the electrochemical behavior of a porous capacitor, in which an *RC* circuit described the double-layer capacitance and the electrolyte resistance inside the pores. In the case of a SH surface, we divide the film into a bulk (C_b) capacitor and an interfacial (C_i)

capacitor in series and use a mass fraction (ω_j) to reference the total mass per unit area of polymer within each component.

$$\omega_i + \omega_b = 1 \tag{5.3}$$

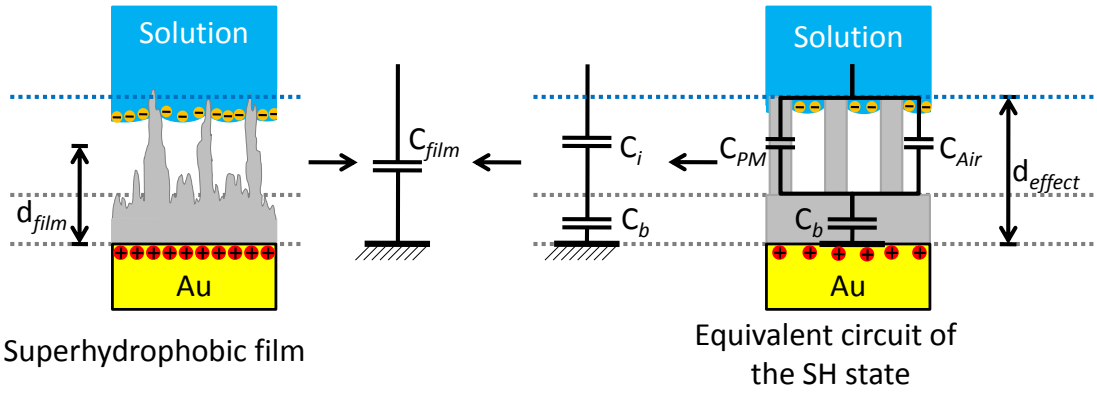

Figure 5.5. Capacitance model for SH PM films. A rough PM film is first divided into the components C_i and C_b in series. Then, the micro-scale features in C_i that provide SH behavior to the film are modeled as polymeric posts, thus, dividing the solid-liquid interface into two different circuit components in parallel (C_{PM}, C_{Air}). Finally, the equivalent circuit (C_{PM}, C_{Air} and C_b) is condensed into a single capacitance component C_{film}.

To vary the roughness of the film, we allow the interfacial region of PM (C_i) to acquire different configurations, thus, varying the topography of the film and enabling the formation of the air/PM composite at the interface. For illustrative purposes, Figure 5.5 shows the specific example in which the C_i is remodeled to form square-shaped posts. This reorganization divides C_i into two different circuit components in parallel, one component accounting for the micron-scale features of polymer at the interface (C_{PM}) and the other, for the air trapped between the solution and C_b (C_{Air}). The geometrical

configuration of PM and air at the interface is defined using a volume fraction that, in the case of posts of any shape, reduces into an area fraction of air (χ_{Air}) and PM (χ_{PM})

$$\chi_{PM} + \chi_{Air} = 1 \tag{5.4}$$

After defining the geometry of each capacitive component of the circuit in terms of mass (ω_j) and area parameters (χ_k), we determine the equivalent dielectric constant for the interfacial region (ε_i), as a parallel contribution of the dielectric constant for air ($\varepsilon_{Air} = 1$) and PM ($\varepsilon_p = \varepsilon_{PM}$)

$$\varepsilon_i = \varepsilon_{PM}\chi_{PM} + \varepsilon_{Air}\chi_{Air} \tag{5.5}$$

and the total dielectric constant of the film ($\varepsilon_{effective}$) as the series contribution of the bulk PM region (ε_{PM}) and the equivalent dielectric constant of the interface (ε_i) (see Appendix A):

$$\frac{1}{\varepsilon_{effective}} = f_i\left(\frac{1}{\varepsilon_i}\right) + f_b\left(\frac{1}{\varepsilon_{PM}}\right) \tag{5.6}$$

$$f_i = \frac{\omega_i}{\omega_i + \omega_b\chi_{PM}} \tag{5.7}$$

$$f_i + f_b = 1 \tag{5.8}$$

where f_i and f_b are corrected expressions for the interfacial and bulk mass fractions, respectively, that account for the topographical configuration of the SH film (χ_{PM}). In the case of the effective separation of the electrolyte from the substrate, a mass balance of PM at the interface correlates the effective and the average thickness of the film

$$\frac{d_{effective}}{d_{film}} = \omega_b + \frac{\omega_i}{\chi_{PM}} \tag{5.9}$$

To use the Helmholtz theory to estimate the capacitance exhibited by SH films, we account for the effective dielectric constant ($\varepsilon_{effective}$) and the effective thickness ($d_{effective}$) of the film through the introduction of a correction factor, ψ, and use the average measured thickness of the film and the dielectric constant of PM as references.

$$\frac{1}{C_{film}} = \frac{d_{effective}}{\varepsilon_0 \varepsilon_{effective}} = \frac{\psi d_{film}}{\varepsilon_0 \varepsilon_{PM}} = \frac{\psi}{C_{PM}} \tag{5.10}$$

where,

$$\psi = \psi\left(\varepsilon_{Air}, \varepsilon_{PM}, \omega_j, \chi_k\right) = \left(\frac{d_{effective}}{d_{film}}\right)\left(\frac{\varepsilon_{PM}}{\varepsilon_{effective}}\right) = 1 + \frac{\omega_i}{\chi_{PM}}\left(\frac{\varepsilon_{PM}}{\varepsilon_i} - \chi_{PM}\right) \geq 1 \tag{5.11}$$

To establish the deviations of $1/C_{film}$ for SH films from the $1/C_{PM}$ values predicted by the Helmholtz theory, Figure 5.6 correlates the experimental and theoretical

values of the SH films from Figure 5.4. These results show positive deviations for the SH PM films with respect to the theoretical values (dotted line) and yield a $\psi = 1.81$. In the case of these SH PM films, neglecting the presence of air at the polymer/solution interface when estimating the inverse of capacitance using the Helmholtz theory results in values about ~50% of the experimental $1/C_{film}$ value. After correlating the model in Equation 5.10 with the experimental observations in Figure 5.6, we consider ψ as a dimensionless composite factor resulting from the effects of the entrapped air at the polymer/solution interface. ψ accounts for both the effective separation distance between the electrolyte solution and the metal substrate, and the limited area of contact between the redox-probe solution and the SH film. This definition suggests that the capacitance of a SH PM film of thickness d is similar to that exhibited by either a smooth PM film ($\varepsilon_{PM} = 2.3$)[18,19] 80% thicker, or a smooth film of thickness d made of a material with an effective dielectric constant (ε) of ~1.3. This result supports the polymer/air composite assumption if we notice that $\varepsilon_{effective}$ decreases towards the dielectric constant of air ($\varepsilon_{Air} = 1$),[23] instead of increasing towards that of free water ($\varepsilon_{water} = 80$).[20-22,32]

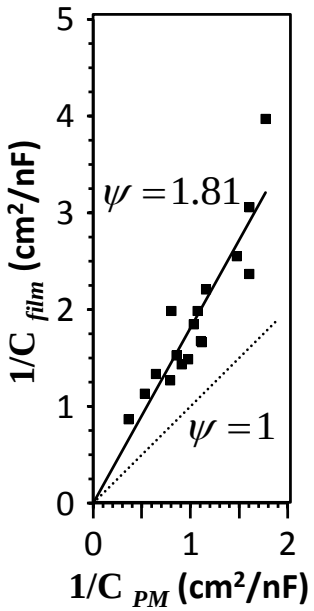

Figure 5.6. Deviations of the experimental values of $1/C_{film}$ for SH films from the $1/C_{PM}$ predicted from the Helmholtz theory assuming a ε of 2.3 ($\psi = 1$, dotted line). The solid line represents a least square fit of the data ($\psi = 1.81$).

To correlate the wetting and the barrier properties of the PM films studied here, Figure 5.7 shows the variation of the composite factor (ψ) calculated from each data point in Figure 5.4 as a function of its hysteresis parameter (H).[44,45] This figure clearly shows a region in which films with $\theta_A > 150°$ exhibit the dielectric properties of pure PM ($H > 0.14$) and another in which the films, also with $\theta_A > 150°$, present dielectric properties that are a combination of that exhibited by PM and air ($H > 0.08$). These distinct situations are delimited by a transitional region shown in gray. In the same way as the wetting properties differ depending whether the surface is in the SH or the NSH state, the dielectric properties of the film exhibit variations as well. This conclusion indicates that accounting for these deviations provides an additional property of the film

that allows the proper differentiation between the SH and the NSH states. In the literature,[37] the definition of the SH state has been arbitrarily set based on the wetting properties: advancing contact angles[4] greater than 150° and contact angle hysteresis ($\theta_A - \theta_R$) lower than 10°.[5] The latter requirement has been established from the compilation of experimental observations[5] since the underlying theory of hysteresis is still not fully understood.[4,51] However, in the case of SH PM films in this study, the correlation of ψ and H provides an additional characteristic of the film that signals the entrapment of air at the polymer/water interface. We do emphasize that the model is not suited for the prediction of the SH regime, but rather, it describes the effect of superhydrophobicity and the resulting interfacial air entrapment on the dielectric properties of a film

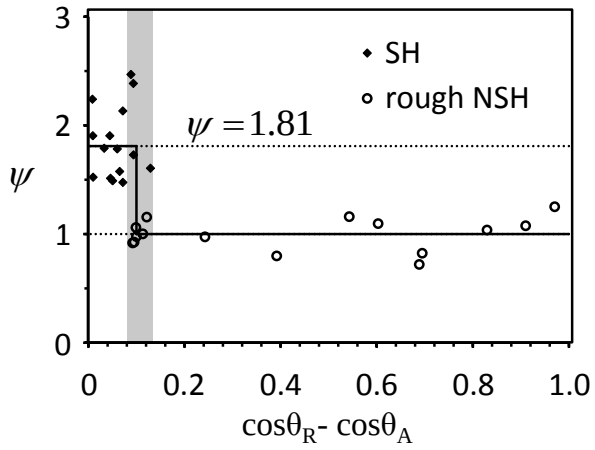

Figure 5.7. Correlation of the ψ values calculated from Figure 5.4 as a function of their hysteresis parameter ($H = \cos\theta_R - \cos\theta_A$). High ($H > 0.14$) and low ($H < 0.08$) values of *H* correspond to films exhibiting NSH and SH behavior, respectively. The intermediate region delimiting both behaviors is presented in gray.

Figure 5.8 shows the 3-D representation of the composite factor (ψ) as a function of both the area fraction of PM in contact with the solution (χ_{PM}) and the mass fraction of PM forming the composite interface (ω_i) using Equation 5.11. Based on Figure 5.8, to enhance the barrier properties of a polymer film $(\psi > 1)$, its surface should have both topographical features able to form a composite interface that entraps air when exposed to water $(\omega_i \neq 0)$, and limited contact with the solution $(\chi_{PM} << 1)$.

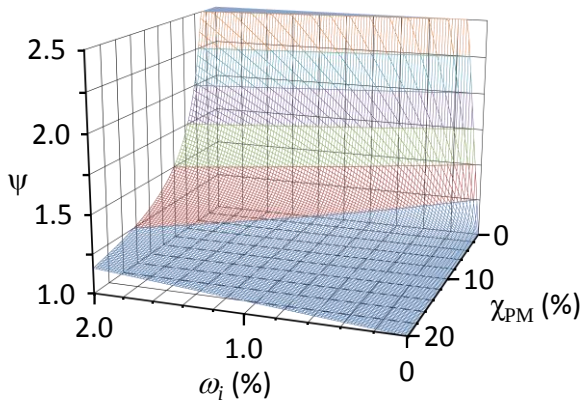

Figure 5.8. 3-D representation of the composite factor (ψ) as a function of both area fractions of PM in contact with the solution (χ_{PM}) and the mass of PM forming the composite interface (ω_i). Values of ψ were predicted using Equation 5.11.

To assess the relative importance of ω_i and χ_{PM} in Equation 5.11, we performed a sensitivity analysis using a model-free method to estimate the sensitivity indices S_{ω_i} and $S_{\chi_{PM}}$,[52] for both of these variables (See Appendix B). S_κ is a measure of the influence of the variable κ in the value of ψ, such that the greater the S_κ, the more influential the κ factor is.[52] To estimate the sensitivity indices, we first observe from

Figure 5.7 that for SH PM films (θ_A = 167°, θ_R = 165°, 2 ≤ χ_{PM} (%) ≤ 6, based on Equation 2.4) to have a composite factor 1 < ψ < 3 (Figure 5.6), the PM present at the polymer/solution interface and forming the micro-scale features should be 1 ≤ ω_i (%) ≤ 1.5 of the total PM of the film. Then, we randomly vary ω_i and χ_{PM} over their selected range of uncertainty, estimate ψ with Equation 5.11 (Figure B.1a, b), and calculate S_{ω_i} and S_{χ_p} using Equations B.1 to B.3. Sensitivity analysis results show that in the region of current experimental accessibility, χ_{PM} ($S_{\chi_{PM}} = 0.88$) has a greater influence on the value of ψ as compared to ω_i ($S_{\omega_i} = 0.077$), suggesting that the effect of having little area of contact between the redox-probe solution and the SH film has the greatest effect over the remarkable enhancement in the barrier properties. Finally, the model proposed in this study suggests that SH PM films exhibit an effective dielectric constant of 1.7 and a separation between the solution and the substrate ~40% higher as compared to NSH PM films.

Conclusions

We have shown that SH PM films synthesized through SIPM exhibit resistances against ion transfer that are over ~3 orders of magnitude higher than those provided by smoother NSH PM films. This remarkable enhancement in the barrier properties takes advantage of limited contact area between the aqueous solution and PM when air is entrapped at the interface of the film. To examine the effect of superhydrophobicity on the dielectric properties, we have assumed that the SH PM films behave as a dielectric in

a parallel plate capacitor, and we have used the Helmholtz theory to rationalize their electrochemical properties. The films exhibit positive deviations from the inverse capacitance exhibited by both rough NSH PM films and the predictions of the Helholtz theory using a $\varepsilon_{PM} = 2.3$ and the physical thickness of the film. To quantify the effect of this entrapped air, the PM/solution interface was modeled as a PM/air composite that contains a circuit of capacitors that account for the air, the PM micro-scale features at the interface, and the layer of PM covering the substrate. Collapse of the circuit into a single equivalent capacitor resulted in a mathematical model that enables a comparison of the capacitance exhibited by NSH ($d_{film}, \varepsilon_{PM}$) and SH ($d_{effective}, \varepsilon_{effective}$) PM films. Finally, correlation of the composite factor and the hyteresis parameter resulted in a convenient method to fully describe the conditions for superhydrophobicity. Tremendous enhancement of the barrier properties of SH films represents a powerful strategy for the protection of a diverse number of substrates in which the size and the geometry of the features decorating the surface would serve as design variables for potential optimization.

References

(1) Sorensen, P. A.; Kiil, S.; Dam-Johansen, K.; Weinell, C. E. *Journal of Coatings Technology and Research* **2009**, *6*, 135-176.

(2) Skale, S.; Dolecek, V.; Slemnik, M. *Progress in Organic Coatings* **2008**, *62*, 387-392.

(3) Sathyanarayana, M. N.; Yaseen, M. *Progress in Organic Coatings* **1995**, *26*, 275-313.

(4) Dorrer, C.; Ruhe, J. *Soft Matter* **2009**, *5*, 51-61.

(5) Callies, M.; Quere, D. *Soft Matter* **2005**, *1*, 55-61.

(6) Yin, Y. S.; Liu, T.; Chen, S. G.; Cheng, S. *Applied Surface Science* **2008**, *255*, 2978-2984.

(7) Liu, T.; Chen, S.; Cheng, S.; Tian, J.; Chang, X.; Yin, Y. *Electrochimica Acta* **2007**, *52*, 8003-8007.

(8) Liu, H. Q.; Szunerits, S.; Xu, W. G.; Boukherroub, R. *Acs Applied Materials & Interfaces* **2009**, *1*, 1150-1153.

(9) Wang, D. A.; Liu, Y.; Hu, H. Y.; Zeng, Z. X.; Zhou, F.; Liu, W. M. *Journal of Physical Chemistry C* **2008**, *112*, 16123-16129.

(10) Zhang, F. Z.; Zhao, L. L.; Chen, H. Y.; Xu, S. L.; Evans, D. G.; Duan, X. *Angewandte Chemie-International Edition* **2008**, *47*, 2466-2469.

(11) Chen, Y.; Chen, S. G.; Yu, F.; Sun, W. W.; Zhu, H. Y.; Yin, Y. S. *Surface and Interface Analysis* **2009**, *41*, 872-877.

(12) Cui, Z. H.; Zhang, F. Z.; Wang, L.; Xu, S. L.; Guo, X. X. *Langmuir* **2010**, *26*, 179-182.

(13) Roach, P.; Shirtcliffe, N. J.; Newton, M. I. *Soft Matter* **2008**, *4*, 224-240.

(14) Qian, T. C.; Li, Y. F.; Wu, Y. Z.; Zheng, B.; Ma, H. W. *Macromolecules* **2008**, *41*, 6641-6645.

(15) Zhu, L. B.; Xiu, Y. H.; Xu, J. W.; Tamirisa, P. A.; Hess, D. W.; Wong, C. P. *Langmuir* **2005**, *21*, 11208-11212.

(16) Lu, X. Y.; Tan, S. X.; Zhao, N.; Yang, S. G.; Xu, J. *Journal of Colloid and Interface Science* **2007**, *311*, 186-193.

(17) Lau, K. K. S.; Bico, J.; Teo, K. B. K.; Chhowalla, M.; Amaratunga, G. A. J.; Milne, W. I.; McKinley, G. H.; Gleason, K. K. *Nano Letters* **2003**, *3*, 1701-1705.

(18) Brandrup, J.; Immergut, E. H.; Grulke, E. A.; Abe, A.; Bloch, D. R. *Polymer Handbook*; 4th ed.; Wiley & Sons: New York, 1999.

(19) Lanza, V. L.; Herrmann, D. B. *Journal of Polymer Science* **1958**, *28*, 622-625.

(20) Martin, N. *The Journal of Chemical Physics* **1985**, *82*, 5663-5672.

(21) Uematsu, M.; Franck, E. *Journal of Physical and Chemical Reference Data* **1980**, *9*, 1291.

(22) Loveday, D.; Peterson, P.; Rodgers, B. *JCT CoatingsTech* **2004**.

(23) Hector, L. G.; Woernley, D. L. *Physical Review* **1946**, *69*, 101.

(24) Tuberquia, J. C.; Nizamidin, N.; Harl, R. R.; Albert, J.; Hunter, J.; Rogers, B. R.; Jennings, G. K. *Journal of the American Chemical Society* **2010**, *132*, 5725-5734.

(25) Seshadri, K.; Atre, S. V.; Tao, Y. T.; Lee, M. T.; Allara, D. L. *Journal of the American Chemical Society* **1997**, *119*, 4698-4711.

(26) Guo, W. F.; Jennings, G. K. *Langmuir* **2002**, *18*, 3123-3126.

(27) Guo, W. F.; Jennings, G. K. *Advanced Materials* **2003**, *15*, 588-591.

(28) Bico, J.; Marzolin, C.; Quere, D. *Europhysics Letters* **1999**, *47*, 220-226.

(29) Bai, D. S.; Ibrahim, Z.; Jennings, G. K. *Journal of Physical Chemistry C* **2007**, *111*, 461-466.

(30) Brantley, E. L.; Holmes, T. C.; Jennings, G. K. *Journal of Physical Chemistry B* **2004**, *108*, 16077-16084.

(31) Jennings, G. K.; Yong, T. H.; Munro, J. C.; Laibinis, P. E. *Journal of the American Chemical Society* **2003**, *125*, 2950-2957.

(32) Hartshorn, L.; Megson, N. J. L.; Rushton, E. *Journal of the Society of Chemical Industry* **1937**, *56*, 266-270.

(33) Porter, M. D.; Bright, T. B.; Allara, D. L.; Chidsey, C. E. D. *Journal of the American Chemical Society* **1987**, *109*, 3559-3568.

(34) Brasher, D. M.; Kingsbury, A. H. *Journal of Applied Chemistry* **1954**, *4*, 62-72.

(35) Mohammadi, R.; Wassink, J.; Amirfazli, A. *Langmuir* **2004**, *20*, 9657-9662.

(36) Ferrari, M.; Ravera, F.; Rao, S.; Liggieri, L. *Applied Physics Letters* **2006**, *89*.

(37) Nosonovsky, M.; Bhushan, B. *Current Opinion in Colloid & Interface Science* **2009**, *14*, 270-280.

(38) Molotskii, M.; Torchinsky, I.; Rosenman, G. *Physics Letters A* **2009**, *373*, 804-806.

(39) Manaka, T.; Ohta, H.; Iwamoto, M.; Fukuzawa, M. *Colloids and Surfaces A: Physicochemical and Engineering Aspects* **2005**, *257-258*, 287-290.

(40) Sorokin, A. V.; Bai, M.; Ducharme, S.; Poulsen, M. *Journal of Applied Physics* **2002**, *92*, 5977-5981.

(41) Sabatani, E.; Cohen-Boulakia, J.; Bruening, M.; Rubinstein, I. *Langmuir* **1993**, *9*, 2974-2981.

(42) Sorokin, A. V.; Mengjun, B.; Stephen, D.; Matt, P. *Journal of Applied Physics* **2002**, *92*, 5977-5981.

(43) Bard, A.; Faulkner, L. *Electrochemical Methods*; 2nd ed.; Jhon Wiley and sons, 2001.

(44) Chen, W.; Fadeev, A. Y.; Hsieh, M. C.; Oner, D.; Youngblood, J.; McCarthy, T. J. *Langmuir* **1999**, *15*, 3395-3399.

(45) Boulange-Petermann, L.; Gabet, C.; Baroux, B. *Journal of Adhesion Science and Technology* **2006**, *20*, 1463-1474.

(46) Doshi, D. A.; Shah, P. B.; Singh, S.; Branson, E. D.; Malanoski, A. P.; Watkins, E. B.; Majewski, J.; van Swol, F.; Brinker, C. J. *Langmuir* **2005**, *21*, 7805-7811.

(47) Asanuma, H.; Noguchi, H.; Uosaki, K.; Yu, H. Z. *Journal of Physical Chemistry C* **2009**, *113*, 21155-21161.

(48) Castela, A. S.; Simoes, A. M. *Corrosion Science* **2003**, *45*, 1631-1646.

(49) Conway, B. E.; Pell, W. G. *Journal of Power Sources* **2002**, *105*, 169-181.

(50) Kötz, R.; Carlen, M. *Electrochimica Acta* **2000**, *45*, 2483-2498.

(51) Bittoun, E.; Marmur, A. *Journal of Adhesion Science and Technology* **2009**, *23*, 401-411.

(52) Saltelli, A.; Tarantola, S.; Campolongo, F.; Ratto, M. *Sensitivity Analysis in Practice: A Guide to Assessing Scientific Models* John Wiley & Sons Inc., 2004.

CHAPTER VI

INVESTIGATING THE SUPERHYDROPHOBIC BEHAVIOR FOR UNDERWATER SURFACES USING IMPEDANCE-BASED METHODS

Introduction

The performance of coatings in applications such as corrosion protection, anti-icing,[1] and self cleaning,[2] among others, is greatly enhanced if the surface of the coating is superhydrophobic (SH) or in the Cassie state of wettability.[3] In this type of wetting state, the rough topography and the intrinsic hydrophobicity of the surface result in limited contact between the liquid phase and the film such that water interacts only at the top of the micron-scale features decorating the film. In the opposite case, the Wenzel state, water displaces the air present in the grooves of the film and completely wets the contours of the film. Note that these definitions are accepted and widely used from the perspective of CA measurements (See Chapter II). However, in the case of a surface immersed in water, we extrapolate and use these classifications based on their physical description. Based on these definitions, the design of superhydrophobic surfaces should account not only for the basic compositional and geometrical requirements[3] that impart such behavior, but also for those factors that favor their stability[4] and enhance their robustness. In the last ten years important research efforts have been made towards the optimization of the geometrical conditions (shapes, aspect ratios, spacing, roughness conditions),[3] fabrication methods[5-7] and materials[8,9] that impart superhydrophobicity. However, in terms of their stability, establishment of the conditions that drive the

transition from the Cassie to the Wenzel state as well as the mechanism in which this process occurs are precise details that still remain unclear.[4,10]

CA measurement is considered the traditional technique to understand the Cassie-Wenzel transition due to its facile implementation and interpretation.[11-13] However, analysis by CA focuses on the events occurring at the triple contact line[12,14] and is blind to those occurring beneath the body of liquid. To circumvent these limitations, transmission diffraction[15] or a combination of optical microscopy and CA[16] have been used to monitor changes beneath the liquid as the surface transitions from the Cassie to the Wenzel state. However, information provided by these techniques, although qualitatively valuable, does not consider the effect of the vertical position of the liquid-vapor interface, a vital piece of information in determining the activation energy required for the Cassie-Wenzel transition.[4]

To characterize the Cassie to Wenzel transition for SH films in underwater environments, we use electrochemical impedance spectroscopy (EIS). In this technique, the film/liquid interactions are measured in the form of a general resistance against the interaction of ions in solution with the underlying substrate, defined as impedance. With this picture in mind, the fundamental differences between the Cassie and the Wenzel wetting regimes are translated into major differences in impedance. In the case of the Wenzel state, lower impedances are exhibited since the liquid wets the contours of the features[17] decorating the film, resulting in both a lower separation between the liquid and the underlying substrate as well as a greater area of contact available for the diffusion of liquid. However, in the case of the Cassie state, two dependent mechanisms are responsible for the higher impedances. The first mechanism is based on the fact that the

liquid is sustained on the top of the micron-scale features[18] leading to a minimization of the liquid/film interaction.[18,19] This aspect has been widely studied for SH films since it is the basis for the CA measurements. The second mechanism responsible for the higher impedances, and one that cannot be completely addressed only by the use of CA measurements,[4] is related to the actual separation of the liquid from the underlying substrate. To exemplify this aspect, Oner and McCarthy[3] showed that SH surfaces with identical chemical composition and physical parameters, except for the height of the micron-scale features decorating the surface, exhibit similar solid/liquid interactions such that their CAs are identical. However, in the case of the impedance characterization, the measurement of a general resistance against the flow of current between the solution and the underlying substrate inherently accounts for both the wetting behavior and the height of the micron-scale features such that the film with the highest micron-scale features would exhibit the largest impedance. In this context, EIS is a powerful technique because it accounts with great sensitivity the surface-liquid interaction, meaning how water wets the surface as well as the effective separation between the liquid and the surface,[20,21] as demonstrated in Chapter V.[5,21]

In this chapter, we use SH polymethylene (PM) films grown from surface-initiated polymethylenation[5] to study the transition of immersed films from the Cassie to the more stable Wenzel state. To do this, instead of waiting on the natural kinetics of the system to accomplish such change, we direct the transition by gradually reducing the surface tension of the liquid in contact with film through discrete additions of ethanol (γ_{EtOH} =23 mN/m). To monitor possible changes at the solid/liquid interface upon ethanol addition, we use CAs to establish the implicit wetting behavior of a SH film when

the surface is in contact with aqueous solutions of specific ethanol concentrations, optical microscopy to visualize the form in which the Cassie to Wenzel transition occurs, and EIS measurements to monitor reductions in the effective separation between the liquid and the underlying substrate from changes in the impedance of the system.[21] Finally, we applied this strategy to determine the reversible character of SH PM films after loss of the Cassie state due to displacement of the air entrapped at the solid-liquid interface.

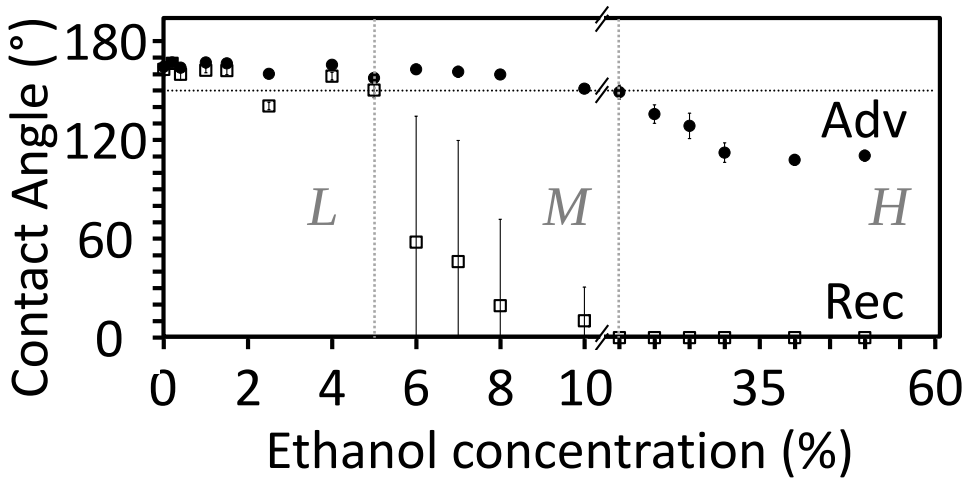

Figure 6.1. CA measurements as a function of the mass fraction of ethanol. CA behavior exhibits three distinctive regions depending on the ethanol concentration. In region *L* (0 to 5%) the film exhibits SH behavior; in region *M* (5 to 15%) the film exhibits both high advancing (>150°) and high hysteresis values ($\theta_A - \theta_R$ <10°); and in region *H*, (15 to 50%) the features decorating the film are completely wet.

Results and Discussion

Contact Angles

We used advancing and the receding CA measurements as indicators of the interactions that occur between a SH surface and ethanol-water solutions of different

surface tensions (γ_{sol}). Figure 6.1 shows that the CA behavior has three distinctive regions depending on the concentration of ethanol: region *L*, for small amounts of ethanol (0 to 5%) in which the film exhibits SH behavior (θ_A>150°, $\theta_A - \theta_R$<10°);[2,22] region *M* at intermediate concentrations of ethanol (5 to 15%) in which the film exhibits both high advancing (>150°) and high hysteresis values ($\theta_A - \theta_R$<10°); and region *H*, for high concentrations of ethanol (15 to 50%) in which the liquid completely wets the contours of the micron-scale features decorating the film. For more detailed information regarding the γ_{sol} behavior and the advantages of the water-ethanol system, please refer to Appendix C.

Figure 6.1 shows that the addition of ethanol to water results in substantial changes in the interaction between the liquid phase and the polymer surface. We observe that in region *L*, the advancing and receding CAs do not exhibit any measurable changes as γ_{sol} is reduced (57 mN/m < γ_{sol} < 71.3 mN/m), indicating that as the aqueous drop is placed on the surface, the Cassie regime is maintained. On the other hand, in region *H,* the reduction in γ_{sol} (44 mN/m <γ_{sol} < 28 mN/m) results in a limiting advancing CA of 110°. This value is close to that exhibited for smooth PM films in contact with water (~103º)[23] and could be interpreted as a reasonable value for the Wenzel state advancing CA since the values for the roughness ratio calculated from the Wenzel equation (1.52) and the polymer/water contact fraction that would render SH behavior from the Cassie equation (< 10%) are in agreement with values published in the literature for SH surfaces.[2,22,24] At these conditions, we envision that placement of the drop on the surface results in the instantaneous movement of the liquid phase from the top to the base of the

micron-scale features decorating the surface. Finally, the intermediate region *M* could be considered as a transition region in which a punctual description of the wetting behavior is not straightforward to define, except that the film is no longer SH for ethanol concentrations greater than 5%. Note that not exhibiting the SH behavior in this region does not necessarily imply that the film transitioned into the Wenzel state. CA results show that specific additions of ethanol to an aqueous solution allow for the tuning of the wetting behavior of the aqueous solution in contact with a SH surface.

Optical Microscopy

To visualize the Cassie to Wenzel transition, Figure 6.2 shows the images of a SH interface (162°/162°) immersed in an aqueous solution of various ethanol concentrations. To collect the images, the probe film is completely covered with a 13 mm column of water followed by discrete additions of ethanol to target specific concentrations without agitating the system. Figure 6.2a shows the interface when pure water sits on the top of the micron-scale features decorating the surface. In contrast to this behavior, Figure 6.2b is an image of the interface after the aqueous solution (13%) penetrates into the grooves and completely wets the contours of the surface. Using the visualization of these extreme cases, we observe in Figures 6.2c, d, and e various stages of the transition for this particular spot of the film in which the interface changes from primarily Cassie behavior to primarily Wenzel behavior when in contact with a 9% ethanolic solution. The images of Figures 6.2d and 3e were obtained 10 and 15 min, respectively, after Figure 6.2c was obtained. Visualization of the interface shows that the transition begins with the nucleation of the Wenzel state at relatively small and randomly located areas of the

interface. This event is followed not only by further creation of nucleation sites but also by the lateral expansion of the areas in the Wenzel state as a result of the lateral displacement of air and its subsequent accumulation to form individual air pockets (Figures 6.2f). The localized character of the transition does not allow us to determine the critical amount of ethanol that favored the transition since the monitored area is much smaller than the area of the film, meaning that the area under observation could remain in the Cassie state by the time that other parts of the film have already transitioned into the Wenzel state. However, visual observation of different areas of the film, as well as impedance results (vide infra), indicate that the amount of ethanol required for the transition is much smaller. Finally, these results show that the entire surface would eventually exhibit the Wenzel state if ethanol is further added into the system or the solution is agitated. Optical microscopy results show visual confirmation of the Cassie to Wenzel transition and also confirm the ability of our strategy to control the transition by varying the ethanol concentration.

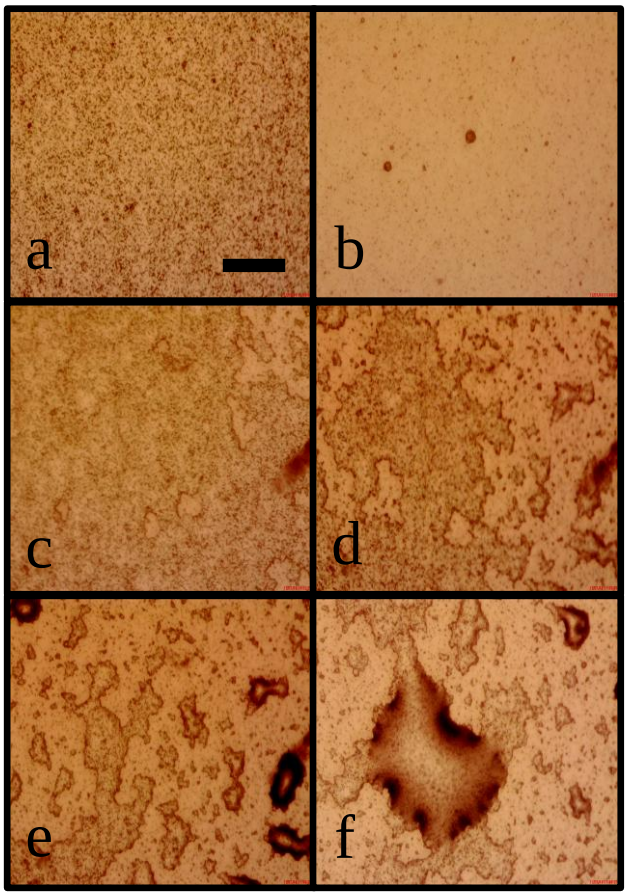

Figure 6.2. Optical microscopy images of the interface of a SH PM film in contact with water-ethanol solutions of various concentrations. (a) the interface is in the Cassie state when in contact with pure water, (b) the interface is in the Wenzel state when in contact with a 13% ethanolic solution, (c, d, e) the interface transitions from a primarily Cassie to a primarily Wenzel state when in contact to a 9% ethanolic solution (Timeframe of Figures d and e in relation to Figure c were 10 and 15 min, respectively), and (f) an air pocket that results from the expansion of the Wenzel state along the interface of the film (the film is in contact with a 13% ethanolic solution). The bar in panel (a) indicates a length of 100 μm.

Single Frequency EIS

Control over surface tension and ultimately over CA enable the controlled transition from the SH Cassie state to the non-SH Wenzel state for PM films. This level of control over the wetting transition will help to reveal specific details about the mechanism in which this process occurs and to enhance our understanding about the

design conditions that make the Cassie regime a more robust state. In this context, EIS not only depends on the surface-liquid interaction, meaning how the liquid probe wets the surface, but also, it accounts, with great sensitivity, for the effective separation between the liquid and the surface,[20,21] an aspect as important as the spacing and the contact area of the micron-scale features in determining the activation energy required for the Cassie-Wenzel transition.[4]

To understand the way superhydrophobicity can be addressed by EIS, it is important to recall that the values of impedance ($/Z/$) and phase angle (ϕ) reported by this technique describe the magnitude and direction of the impedance imaginary vector, respectively.[20] This convenient description of the impedance allows for the accounting of the capacitive

$$Z_{\mathrm{Im}} = \frac{1}{\omega C} \tag{6.1}$$

and resistive contributions of the film

$$Z_{\mathrm{Re}} = R \tag{6.2}$$

by using them as the imaginary and real components, respectively, of the impedance vector.

$$\overline{Z} = Z_{\mathrm{Re}} - jZ_{\mathrm{Im}} \tag{6.3}$$

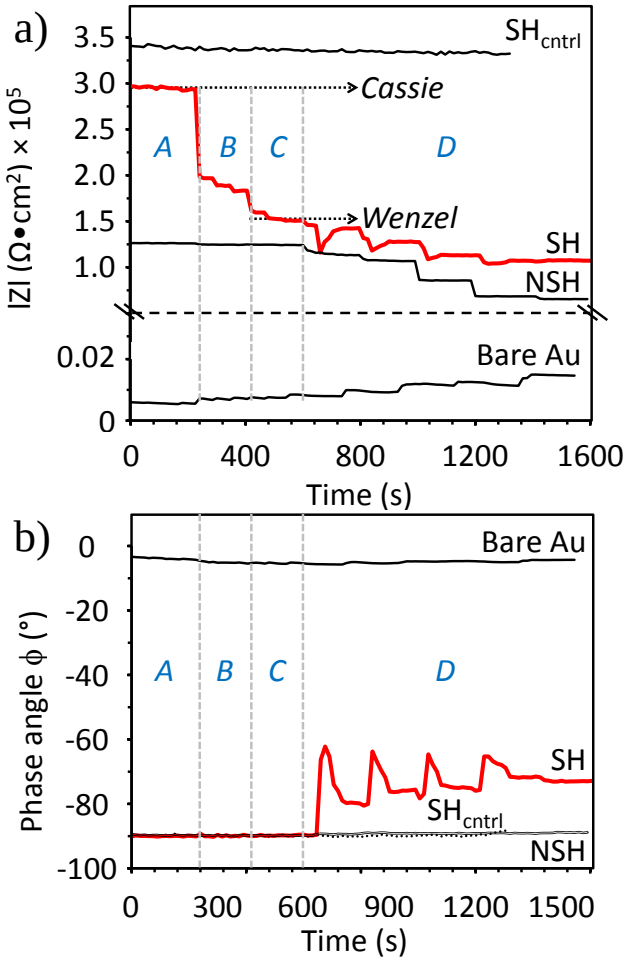

Figure 6.3. Impedance at 1 kHz (a) and phase angle (b) of a SH film (SH) upon additions of ethanol. For proper understanding of the transition process, we also determine the impedance behavior for a SH PM film exposed to pure water (SH_{cntrl}) and both a bare gold substrate (Bare Au) and a smooth PM film (NSH) that followed ethanol additions. Concentrations of the liquid phase targeted a $LiClO_4$ concentration of 0.05 M and specific ethanol concentrations in mass (%): A (0.6, 3, 8)×10^{-3}, B (0.02, 0.16, 0.5), C (0.9, 1.4, 2), and D (4, 9, 13, 17, 21). Ethanol additions were performed every 60 sec for regions A, B and C, whereas in region D every 200 seconds.

The phase angle can be understood as a relative indicator of both contributions, being zero for a purely resistive film in which the liquid and ions are transferring through, -90° for a purely capacitive film that acts as a dielectric to completely separate the liquid from the substrate, and any value in between for a combination of both states. At the SH

state, the film provides the largest separation between the aqueous phase and the substrate, resulting in large impedances with a completely capacitive ($\phi = -90°$) behavior. As the SH state begins to break down and transition into the Wenzel state, liquid and ion penetration into the grooves of the film reduces the capacitive impedance due to both air removal and lower separation between the solution and the substrate. Finally, subsequent penetration of the solution into the film itself leads to a more resistive response and a change in phase angle from the completely capacitive state ($\phi = -90°$).

To identify the impedance characteristics for both the Cassie and the Wenzel states, Figures 6.3a and 6.3b show the impedance and the phase angle behaviors, respectively, at a single frequency of 1 kHz for an initially SH PM film (165°/164°) after discrete additions of ethanol (SH). The single frequency of 1 kHz was selected because, according to complete impedance spectra (See Appendix D), the impedance at this frequency has a primarily capacitive behavior ($\phi \sim 90°$), thus allowing interpretation of the data using Helmholtz theory. In addition, single frequency EIS allows monitoring the impedance at a single frequency over a greater spectrum of concentrations, taking advantage of its in situ character and shorter acquisition time as compared to EIS to rapidly detect the onset of impedance change once the solution begins to displace the air interlayer. To break the SH behavior, we continually increased the ethanol concentration from 0% to 21% in mass according to the specific targets in each region: A (0.6, 3, 8 $\times 10^{-3}$ %), B (0.02, 0.16, 0.5 %), C (0.9, 1.4, 2 %), and D (4, 9, 13, 17, 21 %) while maintaining a constant $LiClO_4$ concentration (0.05 M). To collect the impedance measurements, the probe area (1 cm^2) was completely covered with a 16 ± 1 mm column of $LiClO_4$ (aq) and ethanol followed by agitation of the system in the specific case of

region D to evacuate any large air pockets that may form at the interface of the film. In regions A, B, and C, ethanol additions were performed every 60 seconds, whereas in region D, every 200 seconds.

For proper understanding of the transition process, we also determined the impedance behavior at 1 kHz for three different controls. As a first control, we exposed a SH PM film to a water and $LiClO_4$ solution (SH_{cntrl}) without ethanol and observed that its impedance behavior remains constant in the time window of the experiment, yielding a purely capacitive contribution ($\phi \sim 90°$). To determine the effect that ethanol additions have on the resistivity of the solution, we analyzed the impedance behavior of a bare gold substrate (bare Au) exposed to the same conditions as that of the SH surface. Upon addition of ethanol, changes in the transport properties of the solution affect the resistance of the solution as indicated by the low phase angle ($\phi < 5°$) in Figure 6.3. Finally, a smooth non-SH PM film (NSH) that was exposed to additions of ethanol as well serves as a reference to the SH surface. The behavior of the NSH film provides a scenario in which the impedance exclusively depends on the ethanol-PM interactions without any interference from the topography of the film, thus enabling determination of potential swelling of the film. For the topographic characterization of the SH and non-SH PM films, refer to Chapter V.[21] Experimental results show that the impedance of the NSH film remains constant up to ethanol concentrations of 4% and exhibits discrete reductions in its magnitude as the ethanol content increases while maintaining a primarily capacitive behavior ($\phi \sim -90°$) over the time window of the experiment. For the case of the SH film (denoted SH), the impedance decreases in a step-wise manner over the time window of the experiment. However, in contrast to the NSH film, the phase angle of SH

film exhibits a primarily capacitive component for ethanol concentrations up to 4% that progressively increases its resistive contribution up to a final value of $\sim -70°$.

Figure 6.3 establishes proper identification of the Cassie and the Wenzel states after determining the importance of three different aspects: swelling of the PM film, changes in the resistivity of the liquid phase after additions of ethanol, and variations in the impedance of the SH film as air is displaced from the liquid-solid interface. As the ethanol content increases, the ability of the aqueous solution to transport ions reduces,[25] thus resulting in higher impedances as illustrated by the behavior of the bare Au substrate. However, as evidenced in Figure 6.3a, the magnitude of the impedance for the bare Au substrate does not provide significant contribution to the impedance of the SH film. In terms of swelling, Figure 6.3b shows that the impedance for the NSH film exhibits primarily capacitive behavior, meaning that the PM film provides a complete separation between the liquid phase and the metal substrate. However, for ethanol concentrations greater than 4%, the impedance of the film does exhibit a reduction in its magnitude, which we attribute to swelling near the solid-liquid interface to provide a reduced distance of separation between the solution and the electrode. We emphasize that appreciable swelling that would result in ion transfer through the film is not occurring since the phase angle remains near $\sim -90°$. For the case of ethanol concentrations equal or lower than 4%, the impedance of the NSH film remains constant to indicate that no appreciable PM-ethanol interactions are present.

To identify the impedance behavior of the Cassie and the Wenzel states for a SH film, we first qualitatively assess the behavior of the SH film and identify each state according to its characteristics. In region A, since $\phi \sim -90°$ and the impedance modulus

exhibits the highest impedance magnitude over the time window, in agreement with the behavior of the SH_{cntrl} control, the film is in the Cassie state. For concentrations of ethanol greater than 0.02%, the impedance of the SH film undergoes a stepwise reduction in impedance as the ethanol concentration increases, suggesting that air is being displaced from the solid-liquid interface. To identify the Wenzel state, we emphasize that, besides its lower impedance compared to that of the Cassie state, the film should also offer a complete separation between the liquid phase and the substrate ($\phi \sim -90°$). According to these characteristics, we observe that regions B and C fulfill these requirements. However, since region C exhibits the lowest impedance, indicative of the smallest liquid-substrate separation, we assign the complete Wenzel state to this region. For the case of region B, the intermediate impedances of the SH film suggest that both the Cassie and the Wenzel states are present beneath the liquid phase, which is similar to the mixed Cassie-Wenzel regime shown in the images of Figures 6.2c-f. Finally, region D shows that further additions of ethanol slightly reduce the impedance of the film until ultimately remaining constant at a concentration of 17%. Impedance results in this region show the appearance of a resistive component ($0° < \phi < 90°$), inconsistent with either the Cassie or the Wenzel impedance behavior, that indicates the penetration of ions into the film due to the porous structure of the SH film[21] (Figure 5.1a). The absence of a resistive component in the behavior of the NSH film is the product of the compact and non-porous structure of this film[21] (Figure 5.1b) that completely isolates the substrate from the aqueous media.

Table 6.1. Electrochemical parameters of the Cassie and the Wenzel state calculated for a SH film that undergo discrete additions of ethanol.

Wetting state	ψ	$1/C_{Helmholtz}$ [a] (cm^2/nF)	$/Z/_{average}$ [b] at 1 kHz	$1/C_{Measured}$ [c] (cm^2/nF)
Wenzel	1	1.07	2.95×10^5	0.96
Cassie	1.8 ± 0.3	1.94	1.53×10^5	1.86

[a] the inverse capacitance calculated from the Helmholtz theory (Equation 5.10). [b] the average impedance of each state according to Z_{SH} in Figure 6.3. [c] the inverse capacitance calculated.

To quantitatively validate the Cassie and the Wenzel state assignments of the impedance curve for the SH surface, we compared the $1/C_{Helmholtz}$ predicted by the Helmholtz theory (Equation 5.10) with the $1/C_{Measured}$ that yields the impedances exhibited for both states at 1 kHz according to Figure 6.3a. For the case of the Helmholtz theory, we calculate the inverse of capacitance ($1/C_{Helmholtz}$) with Equation 5.10 (Table 6.1) using an average thickness of d_{film} = 2180 ± 180 nm, the dielectric constant (2.3) of PM, and the correction factor, ψ, to account for either the presence (1.8) or the absence (1) of air at the interface. To estimate the $1/C_{Measured}$ that results in the Cassie and the Wenzel impedances shown in Figure 6.3a, we use the analytical description of the electrochemical system in terms of the circuit model of a metal surface covered by a polymer film[21] and equate the expressions for the components of the impedance vector[20] to the average impedances for both states (See Appendix E). Experimental results of $1/C$ in Table 6.1 show that the experimental estimations, $1/C_{Measured}$, agree with the theoretical predictions, $1/C_{Helmholtz}$, thus indicating that the quantitative as well as qualitative descriptions enable valid assignments of both states.

To translate these differences in capacitance into different average heights between the aqueous phase and the metal surface when the film transitions from the Cassie to the Wenzel state, we use the mathematical description of ψ and the Cassie equation to estimate the effective thickness and the effective dielectric constant of the SH film.[21] These calculations indicate that at the SH state, the effective dielectric constant (1.7) is 26% lower than that of PM, and the effective thickness of the film is 43% higher than the average thickness of the film. The difference in thickness between the Cassie and Wenzel states is ~950 nm, which is consistent with the micron-scale nature of the features decorating the film shown in Chapter IV.[5] Finally, to determine the fraction of the interface that undergoes the Cassie to Wenzel transition at a given concentration, we investigate the impedance behavior of the SH surface at region B. For these calculations we assume that the film behaves as a circuit composed of two capacitances in parallel, one for film areas in the Cassie state and the other for areas in the Wenzel state.

$$C_{film} = C_C \varphi_C + C_W \varphi_W \tag{6.4}$$

where C_i and φ_i are the capacitance per unit area and the area fraction beneath the liquid phase for the component i, respectively. Using Equation 6.4 along with the capacitances of Table 6.1, we determine that these intermediate capacitances correspond to area fractions in the Wenzel state ranging from 50 to 65% before the ultimate transition into a complete Wenzel state. Thus, the rapid nucleation event that leads to the transition occurs at around half of the interfacial area and is responsible for 70% of the total

reduction in impedance, followed by stepwise propagation events until complete transition.

The critical concentrations of ethanol that break the SH behavior are significantly different for CA (5%) versus impedance measurements (0.02 – 2 %). We attribute these differences in the required ethanol concentration to the nature and characteristics of each technique. In the case of the CA measurements, we determine the characteristic behavior of the triple contact line that results from contacting a SH film with a droplet of a specific ethanol concentration. In other words, we focus on the behavior of an aqueous interface when primarily surrounded by air. However, in the case of EIS, we monitor the behavior of the liquid/film interface of a SH film in underwater conditions upon progressive changes in the nature of the liquid phase and in situ displacement of air. More specifically, we focus on the behavior of the micron-thick air layer that is entrapped between the polymer and the aqueous solution. Using the description of each technique, we observe that both the air interlayer in EIS and the aqueous droplet in the Cassie state tend to minimize the unfavorable interactions with the environment surrounding them by transitioning to a more stable configuration. In the case of EIS, the air interlayer transitions into sub-millimeter air pockets randomly distributed along the interface. For CA measurements, the droplet alters its shape as its base makes full contact with the film. The reductions in liquid/air interfacial area for these configurations indicate that the driving force towards the re-accommodation of the interface is much higher for SH films in immersed conditions compared to that of CA conditions, corresponding to the observation that smaller amounts of ethanol are required to favor the transition as shown in our experimental results. The higher susceptibility of SH films to transition into the

Wenzel state in underwater conditions, as well as the remarkable sensitivity of EIS to detect changes in the separation between the liquid and the underlying substrate make impedance a powerful technique to assess the SH properties of films for use in underwater conditions.

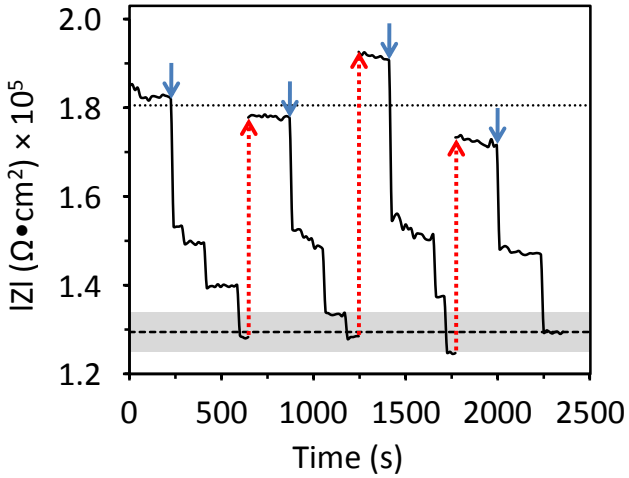

Figure 6.4. Reversible impedance behavior at 1 kHz exhibited by a SH film. In the Cassie state, the film is in contact with 0.05 M $LiClO_4$ (aq), that upon addition of ethanol in the same conditions as in Figure 6.3 up to a final concentration of 4% transitions into the Wenzel state. To reversibly recover the Cassie state, the film was dried with a stream of nitrogen for 1 min followed by drying at ambient conditions for 24 h.

Reversibility Test

We have applied the above strategy to assess the ability of SH PM films to reversibly transition back into the Cassie state after reaching the Wenzel state. To perform the reversibility test, we use single frequency EIS to measure the impedance at 1 kHz of an initially SH film in contact with 0.1 M $LiClO_4$ (aq) that transitioned into the Wenzel state after adding ethanol in the same conditions as in Figure 6.3 to a final concentration of 4%. As a first reconditioning strategy, we reduced the ethanol

concentration back below 0.02% after the film transitioned into the Wenzel state. However, impedance results (not shown) exhibited no increase in the impedance of the film, indicating that the in situ recovery of the Cassie state was not possible. In a second strategy, the films were reconditioned by first rinsing them with water and ethanol, and then drying the surface with a stream of nitrogen for 1 min followed by drying at ambient conditions for 24 h. Figure 6.4 shows the impedance of a SH PM film that reversibly varies its wetting behavior using a combination of additions of ethanol and drying for a total of 3 reconditioning procedures. Impedance results indicate the ability of the SH film to recover the Cassie state upon drying the liquid phase that transitioned into the grooves of the film. Figure 6.4 also shows that upon initiation of the transition, the propagation expands over large areas of the film in a step-wise manner until the entire film exhibits the Wenzel state. Each transition exhibits a different transient profile, suggesting subtle changes in the interface of the film during each reconditioning cycle. Nonetheless, the ability of the film to return to its pristine Cassie state by simply drying the surface in a thorough manner illustrates that these SH surfaces can be regenerated. This characteristic suggests that amphibious coatings such as those exposed to outdoor environments with random periods of moisture could remain in the metastable SH state indefinitely with proper engineering of the coating topography and composition.

Conclusion

Control over the Cassie to Wenzel transition by reducing surface tension allows the identification of both states for immersed SH coatings using impedance measurements. Imaging of the interface at different stages of the transition enables the

identification of three consecutive events in the process: 1) the nucleation of randomly distributed areas under the Wenzel state, 2) lateral propagation of the Wenzel domains, and 3) the collection of air to form air pockets that would subsequently separate from the surface. The characteristics of the Cassie and the Wenzel states were established using the ideal impedance characteristics of each state and quantified based on the predictions of the Helmholtz theory and the electrochemical description of the polymer film. Rationalization of the impedance behavior shows that the transition from the Cassie state results from the rapid nucleation of the Wenzel state over half of the solid-liquid interface as evidenced by the 70% impedance reduction of the system, followed by rapid stepwise propagation events until complete transition. Finally, we applied impedance characterization to establish that SH PM films recover their Cassie state after previous transition into the Wenzel state and thoroughly drying the liquid present at the grooves of the film. Experimental results demonstrate the ability of impedance methods to appropriately characterize immersed aqueous SH interfaces and distinguish important wetting states that govern the applications of these surfaces.

References

(1) Cao, L.; Jones, A. K.; Sikka, V. K.; Wu, J.; Gao, D. *Langmuir* **2009**, *25*, 12444-12448.

(2) Callies, M.; Quere, D. *Soft Matter* **2005**, *1*, 55-61.

(3) Oner, D.; McCarthy, T. J. *Langmuir* **2000**, *16*, 7777-7782.

(4) Noscinovsky, M.; Bhushan, B. *Langmuir* **2008**, *24*, 1525-1533.

(5) Tuberquia, J. C.; Nizamidin, N.; Harl, R. R.; Albert, J.; Hunter, J.; Rogers, B. R.; Jennings, G. K. *Journal of the American Chemical Society* **2010**, *132*, 5725-5734.

(6) Roach, P.; Shirtcliffe, N. J.; Newton, M. I. *Soft Matter* **2008**, *4*, 224-240.

(7) Lee, Y. W.; Park, S. H.; Kim, K. B.; Lee, J. K. *Advanced Materials* **2007**, *19*, 2330-2335.

(8) Qian, T. C.; Li, Y. F.; Wu, Y. Z.; Zheng, B.; Ma, H. W. *Macromolecules* **2008**, *41*, 6641-6645.

(9) Chen, W.; Fadeev, A. Y.; Hsieh, M. C.; Oner, D.; Youngblood, J.; McCarthy, T. J. *Langmuir* **1999**, *15*, 3395-3399.

(10) Patankar, N. A. *Langmuir* **2004**, *20*, 7097-7102.

(11) Ferrari, M.; Ravera, F.; Rao, S.; Liggieri, L. *Applied Physics Letters* **2006**, *89*.

(12) Boinovich, L.; Emelyanenko, A. M.; Pashinin, A. S. *Acs Applied Materials & Interfaces*, *2*, 1754-1758.

(13) Lapierre, F.; Thomy, V.; Coffinier, Y.; Blossey, R.; Boukherroub, R. *Langmuir* **2009**, *25*, 6551-6558.

(14) Gao, L.; McCarthy, T. J. *Langmuir* **2007**, *23*, 3762-3765.

(15) Lei, L.; Li, H.; Shi, J.; Chen, Y. *Langmuir*, *26*, 3666-3669.

(16) Colorado, R.; Lee, T. R. *Langmuir* **2003**, *19*, 3288-3296.

(17) Wenzel, R. N. *Industrial & Engineering Chemistry* **1936**, *28*, 988-994.

(18) Patankar, N. A. *Langmuir*, *26*, 8941-8945.

(19) Su, Y. W.; Ji, B. H.; Zhang, K.; Gao, H. J.; Huang, Y. G.; Hwang, K. *Langmuir*, *26*, 4984-4989.

(20) Bard, A.; Faulkner, L. *Electrochemical Methods*; 2nd ed.; Jhon Wiley and sons, 2001.

(21) Tuberquia, J. C.; Nizamidin, N.; Jennings, G. K. *Langmuir* **2010**, *26*, 14039-14046.

(22) Dorrer, C.; Ruhe, J. *Soft Matter* **2009**, *5*, 51-61.

(23) Seshadri, K.; Atre, S. V.; Tao, Y. T.; Lee, M. T.; Allara, D. L. *Journal of the American Chemical Society* **1997**, *119*, 4698-4711.

(24) Bico, J.; Marzolin, C.; Quere, D. *Europhysics Letters* **1999**, *47*, 220-226.

(25) Kay, R. L.; Broadwater, T. L. *Journal of Solution Chemistry* **1976**, *5*, 57-76.

CHAPTER VII

EXTENSION OF SIPM TO OLEFIN-CONTAINING SUBSTRATES

Introduction

The previous chapters of this thesis have addressed the development of the SIPM strategy for the growth of SH PM films from vinyl-terminated monolayers on silicon and gold. SIPM is a convenient method to create films with inherent SH properties and could be extended to surfaces of virtually any shape and size, as long as a vinyl-terminated monolayer could be deposited on the surface of interest. This characteristic of the technique provides some flexibility in the number of surfaces to which SH PM films could be grown, including a variety of metals, oxides, and semiconductor surfaces. However, despite the versatility of the technique, other important materials such as plastics, cements, fibers, and leather for which it would be important to extend these SH properties would not enable simple functionalization with vinyl moieties. This situation creates the necessity to establish a robust surface modification strategy that enables functionalizing a particular surface with olefin-containing films for their subsequent modification using SIPM to create stable SH films over these substrates.

To impart superhydrophobicity to a variety of substrates, this chapter focuses on the development of strategies that enable the extension of SIPM to surfaces that cannot be coated with vinyl-terminated monolayers through thiol or silane chemistry. To elucidate such a strategy, we take advantage of polymeric materials with olefin-groups incorporated into their structure that are susceptible to be either grown from or casted

onto various surfaces, such as the case of polynorbornene films grown from SI-ROMP[1] and some elastomers such as neoprene, polybutadiene and polyisoprene. Use of polymers as the olefin-containing material for the extension of SIPM has many possible advantages from the structural point of view because of their diversity in the structure and physical properties. However, among these aspects, the number of olefin groups per chain would be of special interest in this chapter since the higher this number, the more initiation sites on the surface, and the faster the growth rate of the film. Although, a higher growth rate of the film would not represent significant differences from the behavior observed from previous chapters, we would expect to observe interesting topographical properties if the initial olefin-containing surface is rough, as will be shown in this chapter.

This chapter examines the extension of SIPM from an olefin-rich surface made of polyisoprene (PIP) that can be deposited onto a diverse number of substrates. For this purpose, we first establish a protocol for the creation of PIP surfaces and characterization of the resultant interfaces using optical microscopy and CA to explore their topography and IR spectroscopy to determine their nature and structure. Dip-coating PIP onto methyl-terminated surfaces results in the formation of micron-scale clusters that, after SIPM, yields PM surfaces with unique morphologies as compared to films grown from 2-D vinyl-terminated monolayers. To explore this effect, the second part of this chapter focuses on the characterization of the various stages of the SIPM process when extended to PIP surfaces. IR characterization of this process reveals that the olefin groups of the PIP surface are hydroborated in agreement with the protocol shown in Chapter IV. However, optical microscopy, CA, and thickness results show that the PM films grown

here are very rough at shorter polymerization times and lower average thicknesses, converting the SIPM approach into a differentiated technology because of the remarkably short times of polymerization and the lower thicknesses required to impart superhydrophobicity.

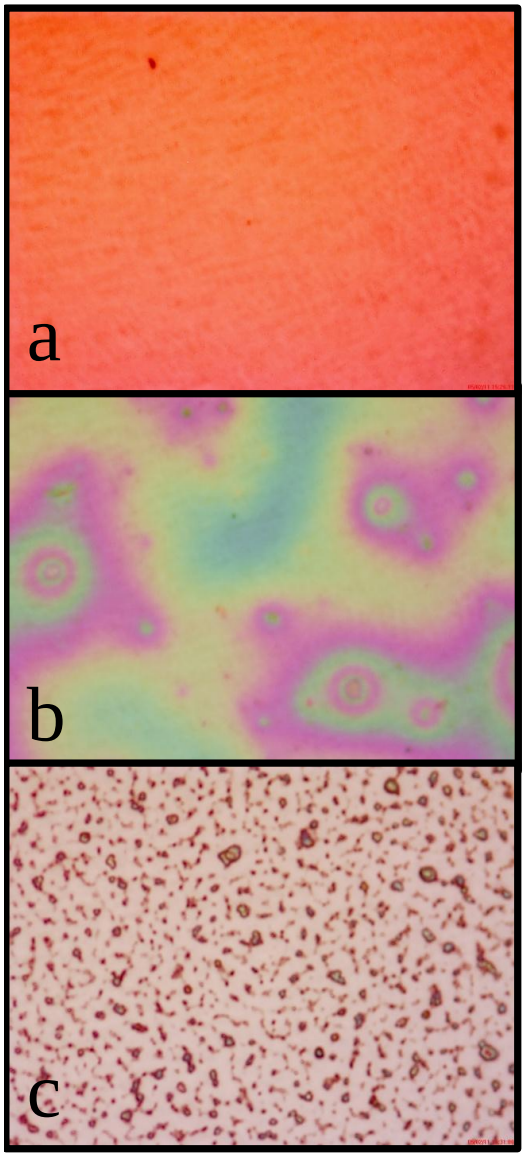

Figure 7.1. Surface topography of (a) a methyl-terminated surface on silicon, (b) a dip-coated PIP film (PIPnr), and (c) a PIPnr surface after rinsing in hexane to create PIP clusters that are robustly bound to the surface.

Results and Discussion

Formation and Characterization of Olefin-Rich Surfaces

With the purpose of extending SIPM to olefin-rich surfaces, we have evaluated two methods to prepare PIP-coated surfaces and chosen the protocol that renders the more stable surface. The first method consisted of dip-coating methyl-terminated films on silicon into a 1 mM solution of PIP in hexane at controlled velocities of immersion and emersion (PIPnr). The second method is an extension of the first one, in which we basically rinsed PIPnr surfaces in hexane to wash off the excess of polymer present at the surface (PIP). All the surfaces were prepared on silicon substrates, except for those characterized with IR spectroscopy that were prepared on gold.

To characterize the topography and the stability of the resulting PIP surfaces, we used optical microscopy (Figure 7.1) and referenced our observations to a silicon substrate terminated with a methyl-terminated monolayer. Figure 7.1 reveals that the initial methyl-terminated substrate is a smooth interface without major features, but after dip-coating in a PIP solution, the image shows the formation of a polymer layer with a liquid-like appearance. This PIPnr film has an unstable character since its exposure to various solvents such as water, ethanol, ether, THF, and hexane rinses the PIP in excess and results in the formation of micron-scale clusters dispersed throughout the surface. This situation is illustrated in Figure 7.1c for the specific case of a hexane rinse to yield surfaces that consist of PIP clusters distributed along the substrate. At these conditions the PIP is adhered to the substrate, and further exposure to the solvents mentioned above does not change the appearance the film. Based on the stability of the PIP film upon

exposure to solvents as compared to the PIPnr, we decide to use the former as the olefin-rich surface in which we will extend the SIPM process.

After establishing the PIP surface as the substrate of interest, we evaluated its thickness, CA and IR spectroscopy behavior. Table 7.1 shows both the advancing and the receding CAs as well as the thickness for a PIP surface and a methyl-terminated surface. Experimental results indicate that coating the methyl-terminated surface with PIP increases the advancing CA and reduces the receding CA because the PIP domains distributed along the surface have the net effect of increasing the surface roughness. The large CA hysteresis suggests that PIP exhibits a heterogeneous surface in agreement with the optical microscopy results.

Table 7.1. Thickness and CA characterization of the initial methyl-terminated surface, the PIP surface, and a hydroborated PIP surface after exposure to partially oxidizing conditions.

Surface	Thickness (nm)	θ_A	θ_R
CH_3-terminated film	2.2 ± 0.9	106 ± 1	96 ± 2
PIP	17.1 ± 1.1	117 ± 4	54 ± 6
HBO-PIP	15.2 ± 0.4	110 ± 1	65 ± 3

Table 7.1 also compares the thicknesses of the methyl-terminated and the PIP surfaces, which as expected, shows the thicker nature of the polymer-coated surface. However, the importance of this result resides in the ability to compare the number of potential initiation sites between the PIP surfaces used here and the vinyl-terminated monolayers used in the previous chapters. For this purpose, we estimate the average thickness of a continuous PIP film that would provide the same number of vinyl moieties

present in a silane monolayer, using the density of silane molecules per unit area (4.8×10^{14} molecules/cm^2)[2] as the number of vinyl moieties that could be activated when hydroborating a monolayer, as well as the molecular weight ($\overline{M_n}$ = 38000) and the density (0.98 g/cm^3) of PIP. After making the appropriate calculations, this average thickness is calculated as 0.51 nm, which is a factor of 30 smaller than the average thickness for the PIP surface reported here and illustrates the much higher potential of this polymer-coated surfaces to grow thicker PM films.

To complete the set of characterization techniques for the olefin-rich surface, we use IR spectroscopy to determine the composition and the structure of the PIP surface. Figure 7.2 and Table 7.2 show the IR spectra and a list of the characteristic modes present for this surface, respectively. For proper reference, Table 7.2 also lists the modes present for PIP in solution.[3] From these results, we first observe that the PIP-coated substrate exhibits the olefin, methyl, and methylene groups that indicate the presence of the polymer at the surface. Further comparison of the IR spectra exhibited by the PIP-coated surface with that for PIP in solution, indicates that confining the polymer on the surface results in differences in the packing and organization of the chains relative to liquid phase, in which the chains have a greater mobility. Higher crystallinity of the PIP surface is exemplified by the location of the CH_2 stretching modes in the PIP-coated surface at lower wave numbers compared to the liquid polymer (ν_{as} = 2926 $cm^{-1}\rightarrow$2919 cm^{-1}, ν_s = 2855 $cm^{-1}\rightarrow$2851 cm^{-1}). Other characteristics of the spectra that suggest differences in the organization of the polymer chains on the PIP surface relative to the liquid is the shift of the CH_3 modes (ν_{as} = 2964 $cm^{-1}\rightarrow$2967 cm^{-1}, ν_s = 2880 $cm^{-1}\rightarrow$2876 cm^{-1}) and the appearance of the in-phase C=C stretching mode at 1700 cm^{-1}.

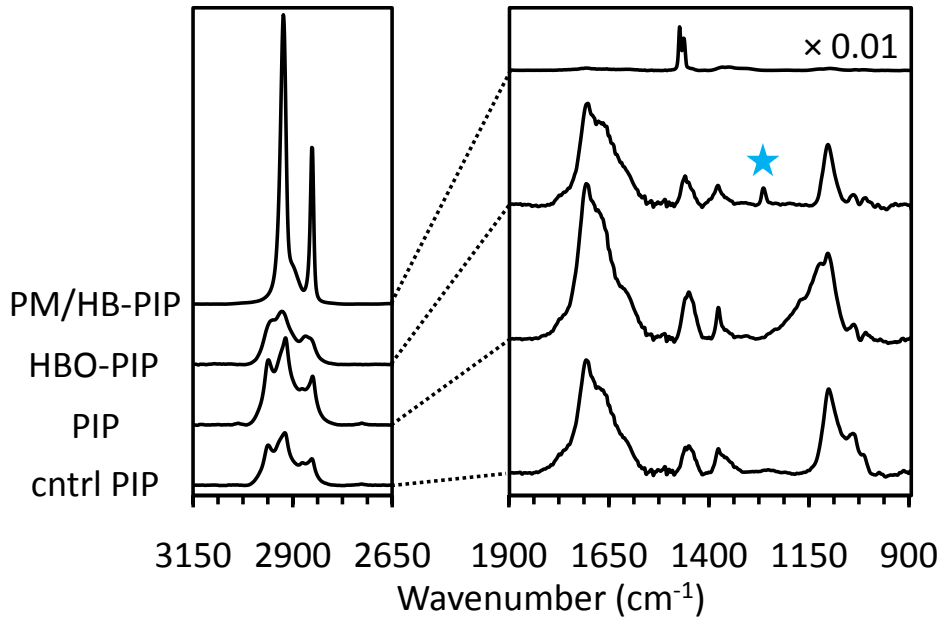

Figure 7.2. IR characterization of the surface at different stages in the SIPM process. The listed films refer to a PM film grown from a hydroborated PIP substrate after SIPM (PM/HB-PIP), a PIP surface on a methyl-terminated substrate (PIP), a PIP-coated substrate exposed to oxidizing conditions (cntrl PIP), and a hydroborated PIP film after going through a partial oxidation process (HBO-PIP). For proper comparison, the spectrum of the PM/HB-PIP film was multiplied by 0.01 and the 1900 – 900 cm^{-1} region was zoomed in for all the spectra. The star highlights the B-O stretching in the HBO-PIP spectrum.

Characterization of the SIPM Process from Olefin-rich Polymer Surfaces.

After establishing the nature and characteristics of the olefin-rich surface, we used PIP surfaces to extend the SIPM and investigate how the film structure, composition, and topography evolve as the SIPM proceeds. Figure 7.2 shows the IR spectra for a PIP surface after hydroboration and subsequent oxidation in an oxygen-saturated THF solution as described in Chapter IV (HBO-PIP) to determine if the hydroboration is indeed occurring, a PIP surface exposed to an oxygen-saturated THF solution (ctrl PIP) as a control to the HBO-PIP surface, and a PM film grown from a PIP substrate after 1 min of polymerization (PM/HB-PIP). The spectra and a list of modes for these surfaces

are included in Figure 7.2 and Table 7.2, respectively, for proper comparison with the initial PIP surface.

Table 7.2. IR modes present in each one of the spectra shown in Figure 7.2.

Liquid	PIP	Cntrl PIP	HBO-PIP	PM/HB-PIP	Mode
3040	3038				=CH stretching
2964	2967	2961	2950		CH_3 asymmetric stretching
2926	2919	2919	2925	2924	CH_2 asymmetric stretching
2880	2876	2875	2866		CH_3 symmetric stretching
2855	2851	2851	2854	2851	CH_2 symmetric stretching
	1705	1707	1702	1702	In-phase C=C stretching
1667	1675	1675	1669		Out-of-phase C=C stretching
				1473	CH_2 asymmetric bending
1451	1449	1449	1458	1462	CH_2 symmetric bending
1379	1374	1375	1376		CH_3 asymmetric bending
			1263		B-O stretching
1131	1121				C-C stretching
1095	1102	1101	1101		CH_2 twisting
1040	1038	1037	1038		CH_3 rocking
1007	1008	1008	1008		C-C stretching

IR results for the various PIP surfaces provide evidence of the successful hydroboration and subsequent polymerization to form PM films. Hydroboration of PIP has been demonstrated by Minoura and Ikeda in solution-phase conditions.[4] In their work, the hydroborated PIP was oxidized after exposing the solution to a water-ethanol solution in the presence of air and characterized with IR spectroscopy to reveal that the borane groups were partially oxidized to R-O-B groups as indicated by the 1340 cm^{-1} peak in their spectrum. Here, we partially oxidize the borane moieties of the PIP-coated surface to convert them into boronic acid groups by exposing the film to an oxygen-saturated THF solution and water.[5-9] This same strategy was used in Chapter IV to

demonstrate the hydroboration of vinyl-terminated monolayers and resulted in the appearance of a mode at a 1263 cm^{-1} attributed to symmetric B-O stretching.[10,11] In the case of the surfaces shown here, the oxidation of the initial borane moieties agrees with the formation of boronic acid groups as indicated by the 1263 cm^{-1} peak in the spectrum, thus suggesting that borane moieties in the polymer undergo a partial oxidation consistent with Scheme 7.1. However, the presence of the C=C stretching vibration of the internal double bonds in the HBO-PIP surface indicate that the polymer chains were partially hydroborated and olefin groups are still available at the surface. Besides the appearance of the B-O stretching mode, the HBO-PIP surface exhibits evident changes in its structure as indicated by the disappearance of the C-C stretching modes in the 1121-1250 cm^{-1} region and the dramatic differences in the CH_2 and CH_3 stretching modes when using the PIP-coated film as the reference. Here, the CH_2 modes shift toward positive values (ν_{as} = 2925 cm^{-1}, ν_s = 2854 cm^{-1}, close to the values exhibited by PIP chains in the liquid state) and the CH_3 modes shift toward even lower values (ν_{as} = 2950 cm^{-1}, ν_s = 2866 cm^{-1}), suggesting a more liquid-like film after hydroboration.

To guarantee that the changes in the HBO-PIP surface resulted from the oxidation of the borane groups, we exposed a non-hydroborated PIP film to the same oxidizing conditions (cntrl PIP) and collected its IR spectrum. Figure 7.2 shows that the C=C stretching vibration at 1675 cm^{-1} is intact, and the mode attributed to the hydroboration of the olefin groups (1263 cm^{-1}) is absent after exposure of the PIP film to oxidizing conditions, supporting our assignments and demonstrating the successful hydroboration of the surface. Immersion of the PIP film in THF and subsequent exposure to water only resulted in slight changes in the structure of the film as evidenced by differences in the C-

C modes that are weaker in the 1121 cm^{-1} region but stronger in the 1008 cm^{-1} region as compared to the PIP-coated surface. This reorganization may be caused by the rapid change in the structure when going from a relaxed (surface immersed in THF) to a collapsed state (surface immersed in water).

Scheme 7.1. Hydroboration and subsequent partial oxidation of PIP films

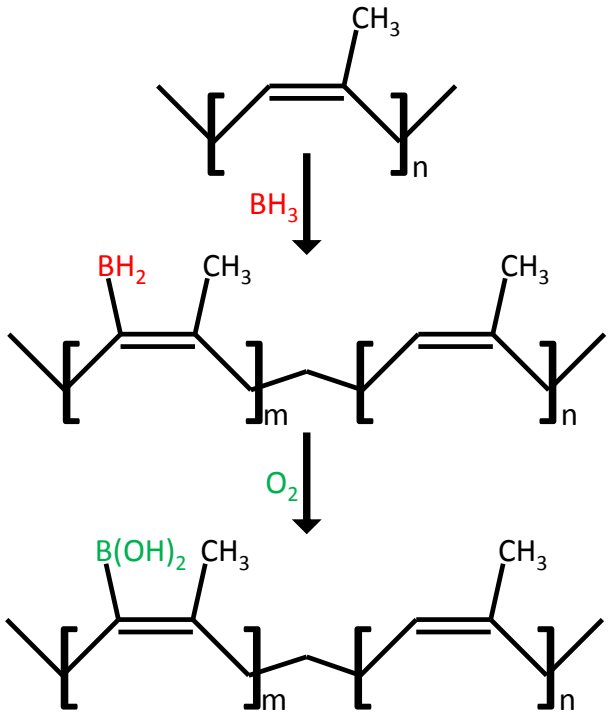

Finally, IR characterization of a PM film grown from a hydroborated PIP film (PM/HB-PIP) indicates the growth of PM chains, as evidenced by CH_2 stretching and bending modes consistently found in linear PM as previously indicated in Chapter IV. However, compared to the PM films grown from vinyl-terminated monolayers, the crystallinity of PM/HB-PIP films is significantly lower as evidence by the shift of the CH_2 stretching modes toward higher values in wavelength (ν_{as} = 2924 cm^{-1}, ν_s = 2851 cm^{-}

[1]). Lower crystallinity of the films grown here could result from the differences in the distribution of the active borane sites within the PIP film. As indicated by optical microscopy, the PIP films consist of clusters distributed along the surface that, after hydroboration, could create specific regions with a high concentration of initiator, thereby favoring the growth of PM chains from discrete locations on the surface and distorting their packing when compared to films grown from substrates with uniformly distributed active sites. In summary, IR characterization of the surface indicates that sufficient olefin groups present in the PIP film are hydroborated to enable the growth of PM films after exposure of the activated surfaces to DM. This result indicates the ability to use olefin-containing polymers to extend SIPM and opens the door for the application of this technique onto a variety of substrates.

The ability to partially oxidize the PIP surface suggests the possibility of quantifying the extent of oxidation using arguments based on XPS data or the Cassie equation as shown in Chapter IV. Especially after observing that hydroboration and oxidation of the PIP surface (HBO-PIP) results in a slight reduction in the advancing CA (Table 7.1) due to the incorporation of oxidized moieties. However, these are not valid approaches because the PIP forms domains and not a contiguous film over the CH_3-terminated film, and therefore, we can only infer a low extent of hydroboration based on the small variations in both CA and IR intensity for the C=C mode.

To further characterize the PM films grown from olefin-rich surfaces, we determined the CA and thickness behavior as a function of time. Table 7.3 shows the evolution of the advancing and the receding CAs as the PM/HB-PIP film grows and compares it to the behavior of a PIP surface. From this table, we observe that only 1 s of

polymerization is sufficient to provide remarkable differences between the PM/HB-PIP and the PIP surfaces. We also observe that the advancing CA is immediately boosted as the polymerization occurs and rapidly reaches a maximum value of 165º ± 1º within 10 s, consistent with the 167º obtained for PM films grown from vinyl-terminated monolayers in Chapter IV, that denote as PM/SAM for the rest of this chapter. However, the impressive aspect about the PM grown from PIP surfaces is the fact that the receding CA reaches a maximum value of 159 ± 2º after 1 min of reaction, meaning not only that this CA is higher, but also that the times to achieve SH behavior is much shorter than that of PM/SAM films, which were 24 h and 72 h in the case of monolayers on gold and silicon, respectively.

Table 7.3. Thicknesses and advancing and receding CA at various times in the SIPM process. The 0 s data point represents a PIP surface.

t (sec)	Thickness (nm)			θ_A			θ_R		
0	17.1	±	1.1	117	±	4	54	±	6
1	210	+/-	60	159	+/-	1	91	+/-	1
10	410	+/-	12	165	+/-	2	98	+/-	5
60	635	+/-	75	166	+/-	1	156	+/-	1
600	3740	+/-	625	165	+/-	1	160	+/-	2
6000	7220	+/-	1640	165	+/-	1	159	+/-	2

To determine the potential topographical aspects of the PM/HB-PIP films that enhance their SH properties relative to the PM/SAM films, we compare optical microscopy images of PM/HB-PIP films at various polymerization times and an image of a PM/SAM film in Figure 7.3. Figures 7.3b, c, and d show images of the PM/HB-PIP surface after 1 s, 10 s, and 10 min of SIPM. From these images we observe that as soon

as the activated surface is in contact with the monomer solution, PM starts growing exclusively at the PIP micro-clusters distributed along the surface as indicated by the decreased separation between the different polymer domains decorating the surface and the absence of growth at various regions along the surface that do not contain such domains. As the reaction proceeds and the domains grow, the PM film spreads along the surface and after 10 s of reaction, the PM has nearly complete coverage of the surface as uncovered silicon areas are barely observed. At these conditions, PM clusters start accumulating and forming larger polymer aggregates along the surface. Finally, after 10 min of polymerization, the surface is completely covered, and we observe the extremely rough appearance of the polymer surface grown here when compared to PM/SAM films (Figures 7.3e).

Finally, to establish the control over thickness of the PM films grown from PIP clusters, we measured the thickness as a function of the polymerization time (Figure 7.4). By comparing CA and thickness results, we conclude that PM/HB-PIP films achieve SH behavior after 1 min of reaction at a film thickness close to 600 nm, contrasting the 24 h of reaction and the 3 μm film thickness required to achieve superhydrophobicity when SIPM is performed from vinyl-terminated monolayers on gold. Experimental results also indicate that both SIPM films exhibit a fast growth rate that slows as the reaction proceeds, suggesting possible occlusion of monomers to the active borane sites. Under these conditions, the PM/HB-PIP films exhibits a higher growth rate as compared to PM/SAM films due to the greater number of borane sites that result from the internal moieties distributed along every other carbon of the PIP chains when compared to a 2-D

surface. Growth of the PM/HB-PIP films indicates the control over the polymerization and the ability to tailor the thickness of the film depending on its final application.

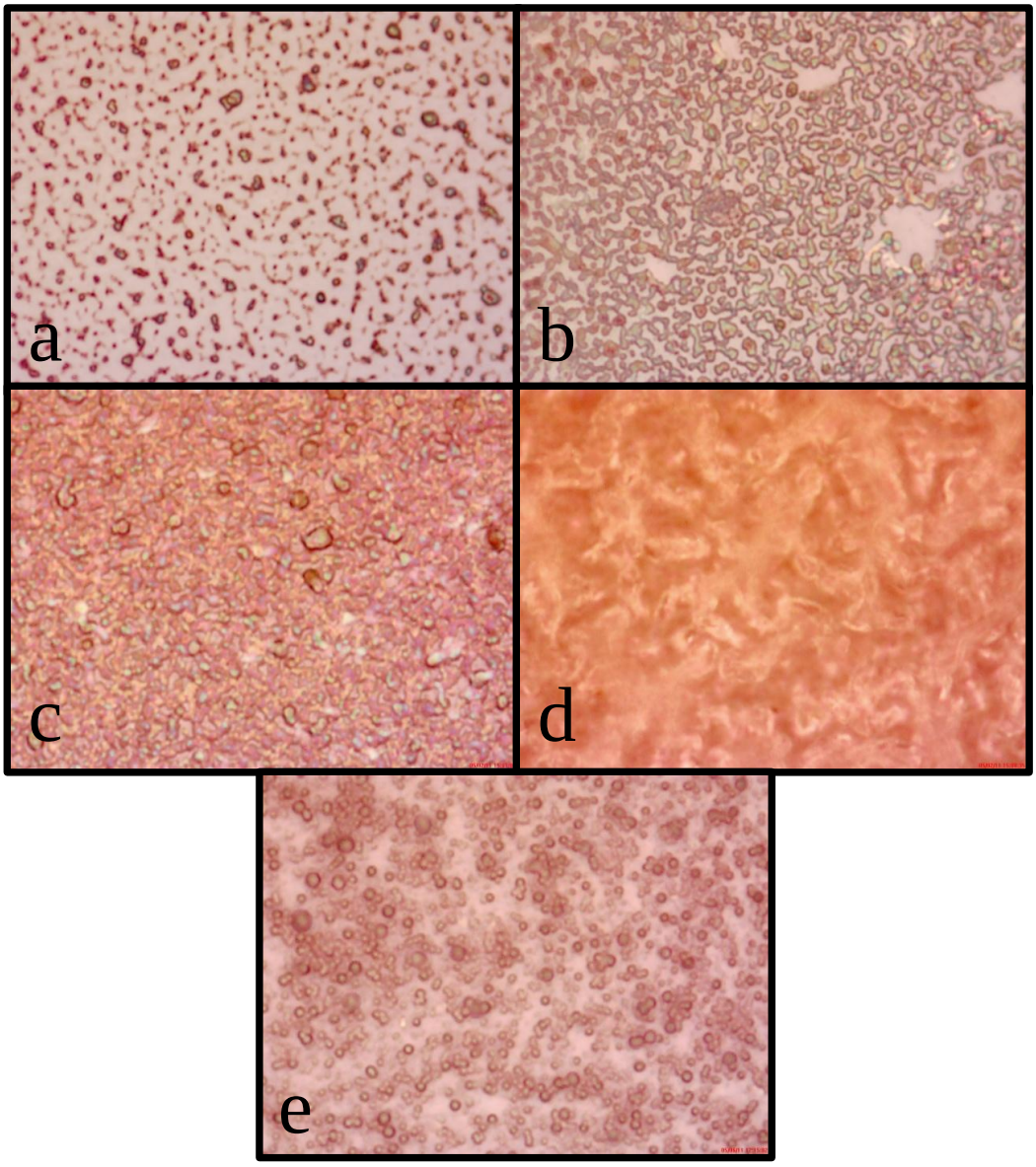

Figure 7.3. Surface topography of (a) a PIP surface and various PM/HB-PIP films after (b) 1 sec, (c) 10 sec and (d) 10 min of polymerization, and (e) a SH PM film grown from a vinyl-terminated monolayer (PM/SAM) after 24 h of polymerization.

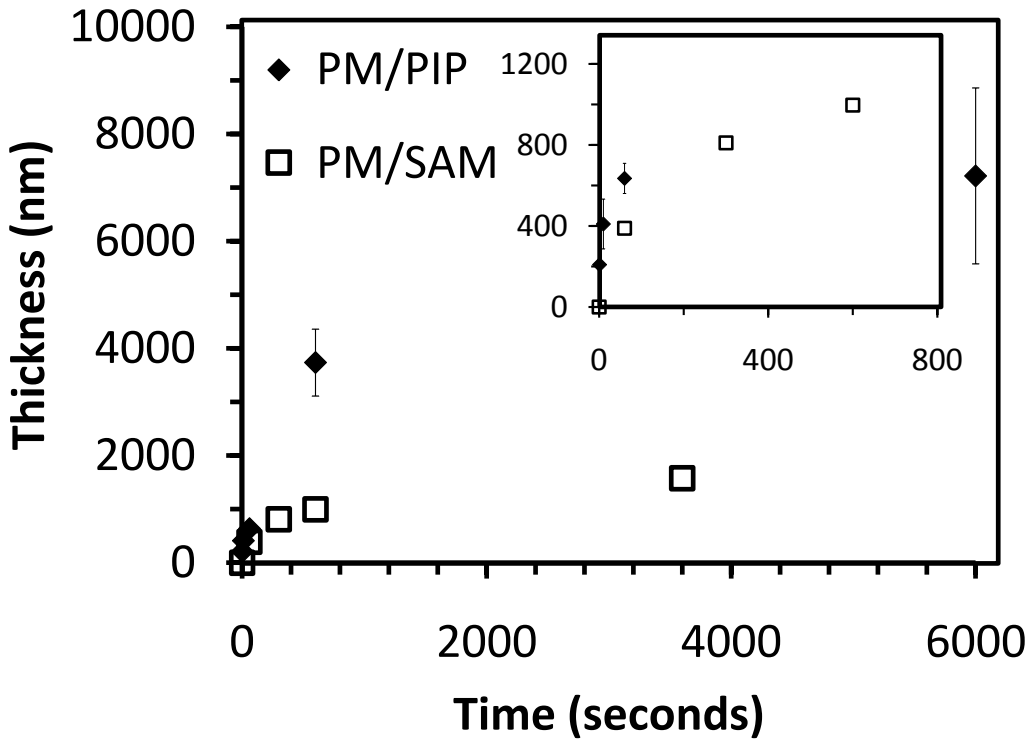

Figure 7.4. Time dependence of thickness for PM films grown from a PIP surface (PM/HB-PIP) and a vinyl-terminated monolayer (PM/SAM).

Conclusions

In this chapter, we have established the successful extension of the SIPM strategy to polymeric substrates containing internal olefin groups. The protocol developed here uses liquid PIP to create PIP clusters along the substrate that provide the high density olefin layer required to extend SIPM to a variety of surfaces that allow PIP adherence. Thickness and CA measurements have indicated that PM/HB-PIP films exhibit faster polymerization rates and require much shorter polymerization times to achieve SH behavior. These outstanding characteristics of the SIPM process using olefin-containing elastomers constitute a promising strategy to modify surface properties and achieve

superhydrophobicity over a variety of substrates in a controllable manner using polymerization times as short as 1 min.

References

(1) Berron, B. J.; Payne, P. A.; Jennings, G. K. *Industrial & Engineering Chemistry Research* **2008**, *47*, 7707-7714.

(2) Wasserman, S. R.; Tao, Y. T.; Whitesides, G. M. *Langmuir* **1989**, *5*, 1074-1087.

(3) Nallasamy, P.; Mohan, S. *Arabian Journal for Science and Engineering* **2004**, *29*, 17-26.

(4) Minoura, Y.; Ikeda, H. *Journal of Applied Polymer Science* **1971**, *15*, 2219-2236.

(5) Onak, T. *Organoborane Chemistry*; Academic Press: New York, 1975.

(6) Brown, H. *Boranes in Organic Chemistry*; Cornell University Press: Ithaca, 1972.

(7) Brown, H. C.; Midland, M. M. *Tetrahedron* **1987**, *43*, 4059-4070.

(8) Davies, A. G. *Journal of Chemical Research-S* **2008**, 361-375.

(9) Tuberquia, J. C.; Nizamidin, N.; Harl, R. R.; Albert, J.; Hunter, J.; Rogers, B. R.; Jennings, G. K. *Journal of the American Chemical Society* **2010**, *132*, 5725-5734.

(10) Shurvell, H. F.; Faniran, J. A. *Canadian Journal of Chemistry* **1968**, *46*, 2082.

(11) Faniran, J. A.; Shurvell, H. F. *Canadian Journal of Chemistry* **1968**, *46*, 2089-&.

CHAPTER VIII

CONCLUSIONS AND FUTURE WORK

Conclusions

The research herein has addressed the development of new approaches and methods for the preparation and characterization of superhydrophobic (SH) surfaces, which have been generally expensive to prepare and tend to gradually lose their SH property via a mechanism that has been poorly understood. Here, we show that ultrathin films of the world's simplest and most common polymer, polymethylene (PM) (or the chemically equivalent polyethylene), exhibit dramatically large resistances against the penetration of aqueous ions if their topology is sufficiently rough on both micro- and nano-scales to merit superhydrophobic behavior.

To achieve these rough, yet thin, PM films, we have developed of a new synthetic platform known as surface-initiated polymethylenation (SIPM) in which immobilized borane moieties serve as active centers for the reaction with diazomethane to grow PM chains one methylene group at a time from a variety of substrates, including gold and silicon. Surface characterization revealed that SIPM enables the rapid growth of PM films in relation to other surface-initiated reactions, producing films thicker than 500 nm after 2 min of reaction and 3 μm after 24 h of reaction, and results in the formation of micro- and nanoscale features that enable the entrapment of air when exposed to water. Consistent with this result, these films exhibit advancing water contact angles greater than 160°, dramatically different than 103° measured for smoother PM films, and

hysteresis values ranging from 2° to 40°, depending on the substrate and polymerization time. However, probably the most interesting property that resulted from the entrapment of air at the polymer/solution interface of these films is their ability to provide remarkable resistances greater than 10^{10} $\Omega \cdot cm^2$ against the transport of aqueous redox probes and behave as a "perfect" capacitor.

This thesis has explored the effect of superhydrophobicity on the dielectric properties of the film based on impedance measurements and the rationalization of such measurements using the Helmholtz theory. Using this approach, we have established that SH PM films exhibit resistances against ion transfer that are over ~3 orders of magnitude higher than those provided by smoother NSH PM films. Rationalization of these results in the context of the Helmholtz theory reveals that the imaginary impedance or inverse capacitance of SH PM films exhibits positive deviations from that predicted by Helmholtz theory for smooth PM films. For this purpose, we model the capacitance behavior of a SH film as a PM/air composite that acts as a circuit of capacitors. The resulting mathematical model of this analysis enables correlation of the effective dielectric properties of the film ($d_{effective}$, $\varepsilon_{effective}$) to measurable properties such as thickness (d_{film}) and the dielectric constant (ε_{PM}) of the PM film, and indicates that SH PM films exhibit an effective dielectric constant of 1.7 and a separation between the solution and the substrate ~40% higher as compared to NSH PM films. Finally, a sensitivity analysis shows that the limited contact area between the aqueous solution and PM in SH films is the primary reason for the enhancement in the barrier properties of the film.

Experimental results shown in this work have demonstrated the remarkable sensitivity of impedance-based methods to assess the SH behavior of films in underwater conditions. This potential motivated the establishment of the principles and the theoretical concepts that could allow the identification of the Cassie and the Wenzel states under these conditions. To accomplish this purpose, we first established the mechanism of the transition by imaging the interface of the film and identifying three distinct events of this process: a nucleation event in which small areas beneath the liquid phase transition into the Wenzel state, a propagation event characterized by the enlargement of the Wenzel domains and the lateral displacement of air, and a final event in which the air at the interface is collected to form air pockets. Using this visualization of the transition, we characterized the impedance at a frequency of 1 kHz for an initially SH film that changes its wetting behavior upon reduction of the surface tension of the liquid phase and established the Cassie and the Wenzel state characteristics based on impedance measurements. To conclude, we have explored how SH surfaces recover their initial Cassie state after transitioning into the Wenzel state and drying the liquid present in the grooves, establishing the applicability of these SH films in outdoor environments with occasional periodic submersion in water.

Finally, we have discussed the extension of the SIPM approach to virtually any substrate that has incorporated olefin groups; more specifically, we have explored the characteristics and the protocol to grow SH films from liquid polymer substrates to introduce the concept of a SH veneer atop a NSH surface. This approach exploits the adhesive properties of some liquid polymers such as polyisoprene to basically create olefin-containing base surfaces on a variety of substrates. Using this scenario, the SIPM

approach could be extended to surfaces in which olefin groups could not be created, such as polymeric and inorganic materials to modify their surface properties.

Future Work

The developments addressed in this thesis demonstrate the abilities (1) to prepare SH polymer films from an initially smooth surface by exploiting our new borane-initiated SIP, (2) to measure the dramatic effect that the air interlayer provides on the barrier and dielectric properties of these films, and (3) to develop a new electrochemical technique to investigate the transition of immersed SH films to the non-SH Wenzel state (and beyond). From this foundation, One can explore the development of new polymer film compositions to improve the intrinsic hydrophobicity of SH interfaces for enhanced stability in the Cassie state as well as new strategies for layered, multifunctional barrier coatings containing a SH veneer to reduce any water/surface interactions, as well a dense base layer to provide a high resistance against the penetration of water vapor or other reagents. These approaches will provide the requisite versatility of tools to explore the replication of natural SH surfaces as coatings and veneers on initially smooth substrates.

Develop New Polymer and Copolymer Compositions

The contact angle under SH conditions depends on the low surface energy of the film and the limited water/polymer area of contact as shown in the Cassie equation. To accentuate both parameters and enhance the SH condition, one can investigate the effect of various precursors for the SIP such as diazoethane (DE)[1] and 1,1,1-trifluorodiazoethane[2] to produce polymers with compositions and structures different

from that obtained with DM as the precursor. One can also investigate the copolymerization of each of these monomers with DM since their steric bulk may lead to reduced rates of polymerization. Given the $–CH_3$ and $–(CH_3)_3$ functionality of these precursors that will likely become enriched at the surface of the resulting polymer, we would expect intrinsic contact angles of 115 - 125°, far exceeding that of ~100° for PM, and surfaces with greater oleophobicity. When polymerized into a film with multi-scale roughness, these films should result in higher contact angles than those of ~165º we have reported for PM. Thus, aside from diversifying the compositions that can be grown from borane-initiated SIP, we would expect these films to improve the stability of the all-important SH (Cassie) state.

Develop SH Polymer Films as Veneers atop Smooth Polymer Films

The ability to impart SH or superoleophobic (SO) properties to initially smooth polymer surfaces could impact applications ranging from water-repellant coatings to protect internal electronics, layered anti-corrosion systems with combined water and O_2 resistance, and (finger) oil-repellant coatings for cell phones, just to note a few. To prepare these types of films, one can explore the preparation of SH and SO coatings atop smooth polymer films by using a SIP approach. To extend this polymerization strategy to smooth polymer films, one can initially employ SI-ROMP to grow films containing fluorocarbon-modified polyhedral oligomeric silsesquioxane cubes, denoted as fluoroPOSS. FluoroPOSS has been blended in polymers by Cohen and coworkers[3] to achieve rough superoleophobic surfaces where the fluorocarbon chains dominate the polymer/air interface and we envision that these types of materials could become a

standard component in oleophobic or low dielectric materials. For this purpose, one could take advantage of the surface initiated approach to grow fluoroPOSS containing films and investigate the effect of the fluorocarbon chain length on the film's surface and dielectric properties.

SIP Replication of SH Coatings in Nature onto Solid Substrates

To replicate Nature's engineered, microscopically rough, and highly functional surfaces, one could strategize the use of SIP to create films made of low energy materials that imitate the topographic characteristics found in nature. While methods do exist to replicate various surfaces, including those of plants,[4,5] the end product is a polymer that one can hold and perform experiments on, *but it is not a coating that is bound to a solid surface*. To create coatings that mimic the topographic characteristics of successful SH systems found in nature, one could create molds of these systems and use them to confine the SIP of low surface energy materials. This strategy could be based on SI-ROMP using a variety of monomers from the norbornene family, including NBFn, NBHn, and even NB-fluoroPOSS.

References

(1) Buckley, G. D.; Cross, L. H.; Ray, N. H. *J. Chem. Soc.* **1950**, *1950*, 2714-2718.

(2) Gilman, H.; Jones, R. G. *J. Am. Chem. Soc.* **1943**, *65*, 1458-1460.

(3) Tuteja, A.; Choi, W.; Ma, M.; Mabry, J.; Mazzella, S.; Rutledge, G. C.; McKinley, G.; Cohen, R. E. *Science* **2007**, *318*.

(4) Feng, J.; Huang, M.; Qian, X. *Macromol. Mater. Eng.* **2009**, *294*, 295-300.

(5) Furstner, R.; Barthlott, W.; Neinhuis, C.; Walzel, P. *Langmuir* **2005**, *21*, 956-961.

APPENDIX A

MODELING THE EFFECT OF SUPERHYDROPHOBICITY ON THE DIELECTRIC PROPERTIES OF THE FILM

To rationalize the deviations exhibited by SH films from the theoretical values shown in Figure 5.4, we account for the trapped air at the polymer/water interface and for the presence of micron-scale topographical features on SH films that could influence the effective separation as well as the effective dielectric constant of the medium between the solution and the substrate. To address the role of superhydrophobicity on the capacitance, we envision the surface as a heterogeneous PM/air composite interface and describe it as a circuit of capacitive elements. See Figure 5.5 in the main text. We first note that the mass of PM (m) forming the film is related to its volume (V_{film}) and the density of PM (ρ_{PM}) by

$$m = V_{film}\rho_{PM} \tag{A.1}$$

Then, we divide the film into a bulk (C_b) capacitor and an interfacial (C_i) capacitor in series, using a mass fraction (ω_j) to reference the total mass per unit area of polymer in each component.

$$\omega_i + \omega_b = 1 \tag{A.2}$$

To vary the roughness of the film, we allow the interfacial region of PM (C_i) to acquire different configurations, thus, varying the topography of the film and enabling the formation of the air/PM composite at the interface. For illustrative purposes, Figure 5.5

shows the specific example in which the C_i is remodeled to form square-shaped posts. This reorganization divides C_i into two different circuit components in parallel, one component accounting for the micron-scale features of polymer at the interface (C_{PM}) and the other, for the air trapped between the solution and C_b (C_{Air}), which in terms of the Helmholtz theory results in:

$$C_i = C_{PM} + C_{Air} \tag{A.3}$$

$$\frac{\varepsilon_i \varepsilon_0 A}{d_i} = \frac{\varepsilon_{PM} \varepsilon_0 A_{PM}}{d_i} + \frac{\varepsilon_{Air} \varepsilon_0 A_{Air}}{d_i} \tag{A.4}$$

where A is the total area of the film, ε_j is the dielectric constant of the component *j*, A_j is its area, and d_j is its thickness. The geometrical configuration of PM and air at the interface is defined using a volume fraction that reduces into an area fraction of air (χ_{Air}) and PM (χ_{PM}).

$$V_i = V_{PM} + V_{Air} \tag{A.5}$$

$$1 = \chi_{PM} + \chi_{Air} \tag{A.6}$$

Substitution of this relationship in Equation A.4 and after some mathematical rearrangement, we obtain the equivalent dielectric constant of the interface:

$$\varepsilon_i = \varepsilon_{PM} \chi_{PM} + \varepsilon_{Air} \chi_{Air} \tag{A.7}$$

To obtain an expression for the equivalent dielectric constant of the superhydrophobic film, we take the film as an equivalent circuit with C_i and C_b represented in series.

$$\frac{1}{C_{film}} = \frac{1}{C_i} + \frac{1}{C_b} \tag{A.8}$$

and relate the effective thickness of the film ($d_{effective}$) to the thickness of both capacitive components using:

$$d_{effective} = d_i + d_b \tag{A.9}$$

Rearrangement of Equation A.8 in terms of the Helmholtz theory and using Equation A.9, we obtain the following expression:

$$\frac{d_i + d_b}{\varepsilon_{effective}} = \frac{d_i}{\varepsilon_i} + \frac{d_b}{\varepsilon_{PM}} \tag{A.10}$$

To relate $d_{effective}$ with the average thickness of the rough PM film (d_{film}), we define d_{film} in terms of an edge (d_e) and a bulk (d_b) part.

$$d_{film} = d_b + d_e \tag{A.11}$$

Since the average thickness implies a smooth topography, the mass of polymer in the edge part rearranges to form the topographical features present in the SH film. This geometrical definition of the film allow relating d_i and d_u.

$$d_i = \frac{d_e}{\chi_{PM}} \tag{A.12}$$

Substituting Equation A.12 into Equation A.8, we obtain an expression for the dielectric constant of the film.

$$\frac{1}{\varepsilon_{effective}} = f_i\left(\frac{1}{\varepsilon_i}\right) + f_b\left(\frac{1}{\varepsilon_{PM}}\right) \tag{A.13}$$

$$f_i = \frac{\omega_i}{\omega_i + \omega_b \chi_{PM}} \tag{A.14}$$

$$f_i + f_b = 1 \tag{A.15}$$

Using the previous set of equations, we are able to relate the effective parameters of the film ($d_{effective}, \varepsilon_{effective}$) to the d_{film} and ε_{PM} parameters, using the dimensionless composite factor ψ.

$$\frac{1}{C_{film}} = \frac{d_{effective}}{\varepsilon_0 \varepsilon_{effective}} = \frac{\psi d_{film}}{\varepsilon_0 \varepsilon_{PM}} = \frac{\psi}{C_{PM}} \tag{A.16}$$

$$\psi = \left(\frac{d_{effective}}{d_{film}}\right)\left(\frac{\varepsilon_{PM}}{\varepsilon_{effective}}\right) \tag{A.17}$$

Dividing Equation A.9 by d_{film} and rearranging using Equation A.12, we obtain the $\frac{d_{effective}}{d_{film}}$ ratio:

$$\frac{d_{effective}}{d_{film}} = \omega_b + \frac{\omega_i}{\chi_{PM}} \tag{A.18}$$

After multiplying Equation A.13 by ε_{PM}, we obtain the $\frac{\varepsilon_{PM}}{\varepsilon_{effective}}$ ratio:

$$\left(\frac{\varepsilon_{PM}}{\varepsilon_{effective}}\right)=\left[\frac{\varepsilon_{PM}\omega_i}{\varepsilon_i\chi_{PM}}+\omega_b\right]\left[\frac{1}{\omega_b+\frac{\omega_i}{\chi_{PM}}}\right] \tag{A.19}$$

Replacing Equations A.18 and A.19 in Equation A.17 yields the expression for ψ

$$\psi=\psi\left(\varepsilon_{Air},\varepsilon_{PM},\omega_j,\chi_k\right)=1+\frac{\omega_i}{\chi_{PM}}\left(\frac{\varepsilon_{PM}}{\varepsilon_i}-\chi_{PM}\right)\geq 1 \tag{A.20}$$

APPENDIX B

SENSITIVITY ANALYSIS OF THE DIELECTRIC MODEL FOR SUPERHYDROPHOBIC FILMS

To assess the relative importance of ω_i and χ_{PM} in Equation A.20, we performed a sensitivity analysis using a model-free method to estimate the sensitivity index S_{ω_i} and $S_{\chi_{PM}}$,[1] for both of these variables.

$$S_{\omega_i} = \frac{V\left(E\left(\psi|\omega_i\right)\right)}{V_\psi} \tag{B.1}$$

$$S_{\chi_{PM}} = \frac{V\left(E\left(\psi|\chi_{PM}\right)\right)}{V_\psi} \tag{B.2}$$

Table B.1 Range of uncertainty for the variables ψ, ω_i, and χ_{PM} in Equation A.20 selected from Figure 5.6 and Figure 5.7.

Variable	Range
χ_{PM}	$2 \leq \chi_{PM}(\%) \leq 6$
ψ	$1 < \psi < 3$
ω_i	$1 \leq \omega_i(\%) \leq 1.5$

where V_ψ is the variance of ψ, and $V\left(E(\psi|\kappa)\right)$ is the *main* effect of the variable κ ($\kappa = \omega_i, \chi_{PM}$) on ψ, defined as the variance of $E\left(\psi|\kappa = \Phi\right)$ over all possible values of κ

, and $E\left(\psi|\kappa=\Phi\right)$ is the average of ψ when the input variable κ is at a fixed value of Φ. To estimate S_κ, we use the following relationship:

$$S_\kappa = \frac{V\left(E\left(\psi|\kappa\right)\right)}{V_\psi} = 1 - \frac{E\left(V\left(\psi|\kappa\right)\right)}{V_\psi} \tag{B.3}$$

where $E\left(V\left(\psi|\kappa\right)\right)$ is the average of $V\left(\psi|\kappa=\Phi\right)$ over all possible values of κ, and $V\left(\psi|\kappa=\Phi\right)$ is defined as the variance of ψ when the input variable κ is at a fixed value of Φ. S_κ is a measure of the influence of κ in the value of ψ, such that the greater the S_κ, the more influential the κ factor is.[1] To estimate the sensitivity indices, we define the region of interest for each one of the variables using Figure 5.6 and Figure 5.8 (Table B.1) and randomly vary ω_i and χ_{PM} over their selected range of uncertainty, estimate ψ with Equation A.20 (Figure B.1a, b), and calculate S_{ω_i} and S_{χ_p} using Equations B.1 to B.3. Sensitivity analysis results show that in the region of current experimental accessibility, χ_{PM} $\left(S_{\chi_{PM}} = 0.88\right)$ has a greater influence on the value of ψ as compared to ω_i $\left(S_{\omega_i} = 0.077\right)$, suggesting that the effect of having little area of contact between the redox-probe solution and the superhydrophobic film has the greatest effect over the remarkable enhancement in the barrier properties.

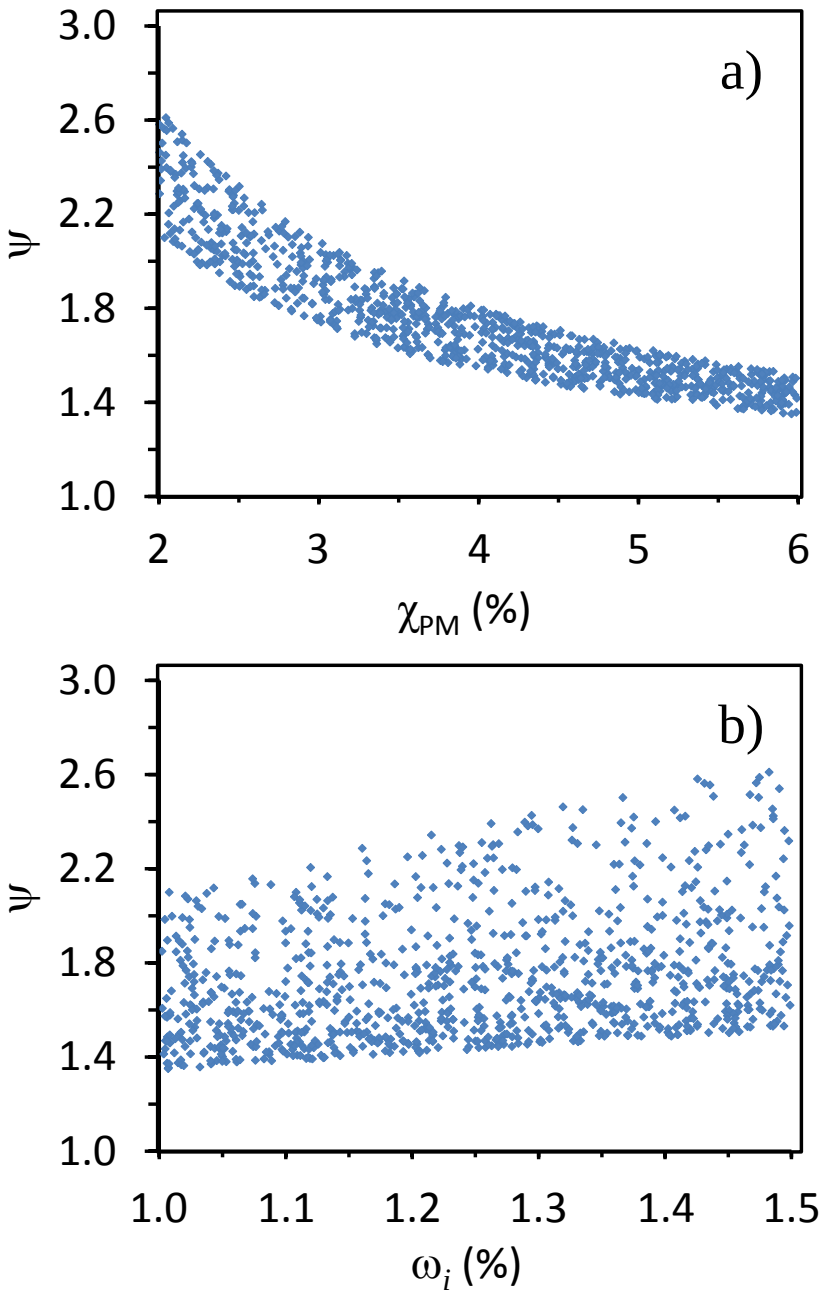

Figure B.1 Composite factor (ψ) as a function of both ω_i and χ_{PM}. Graphical representation shows the values of ψ estimated with Equation A.19 and random values of ω_i and χ_{PM} over their selected range of uncertainty.

References

(1) Saltelli, A.; Tarantola, S.; Campolongo, F.; Ratto, M. *Sensitivity Analysis in Practice: a Guide to assessing scientific models* John Wiley & Sons Ltd., 2004.

APPENDIX C

SURFACE TENSION OF ETHANOL-WATER SOLUTIONS AT VARIOUS CONCENTRATIONS

To properly direct the Cassie-Wenzel transition using variations in the surface tension of the aqueous solution (γ_{sol}) in contact with the SH film, we first established the behavior of γ_{sol} at various mass fractions of ethanol (Figure C.1). The surface tension of the liquid was as high as 71.3 mN/m for pure water (γ_{water}) and as low as 21.7 mN/m for pure ethanol (γ_{EtOH}), and continuous additions of ethanol to the aqueous solution resulted in a monotonic reduction of γ_{sol}. The results show that large reductions in the surface tension of the liquid phase are achieved at low concentrations of ethanol, i.e. concentrations of ethanol of only 5% result in reductions in γ_{sol} as large as 30%. This important characteristic of the system allows the variation of γ_{sol} using small amounts of ethanol while maintaining the conductivity of the liquid and reducing possible swelling of the film as shown in Chapter 6. Using ethanol also has the advantage of being easier to separate from the surface as compared to other substances that could be used to reduce the surface tension of water, as in the case of surfactants. This aspect is important when studying the ability of the superhydrophobic films to recover their initial Cassie state after transitioning into the Wenzel state since any traces of the surface tension modifier will irremediably favor the latter state. These facts make ethanol a highly suitable candidate for tailoring the surface tension of the liquid in contact with a SH film and controlling the rate at which the Cassie-Wenzel transition occurs.

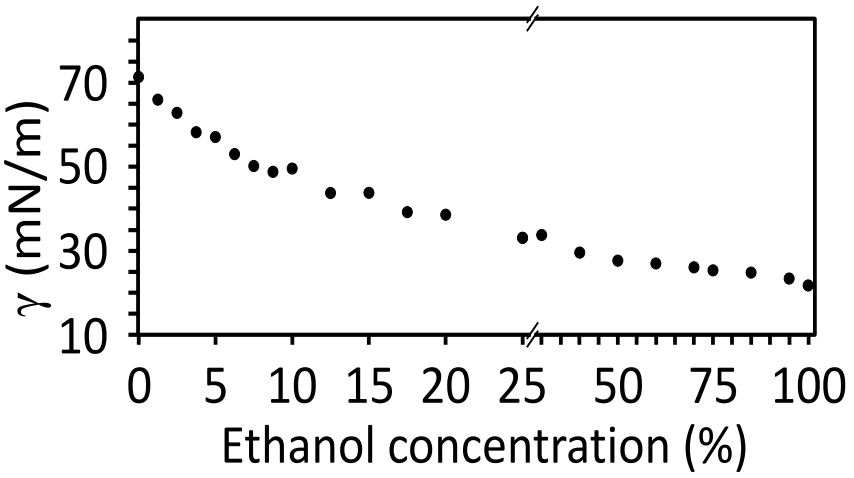

Figure C.1. Surface tension of ethanol-water mixtures as a function of the mass percentage of ethanol.

APPENDIX D

EIS BEHAVIOR OF SUPERHYDROPHOBIC FILMS IN THE PRESENCE OF ETHANOL

To explore the impedance behavior of a SH surface at various wetting conditions, Figure D.1 shows the impedance spectra and the phase angle for a SH (165°/164°) PM film when exposed to aqueous solutions of various ethanol concentrations and using $LiClO_4$ (0.05 M) as the supporting electrolyte. EIS spectra were collected only over a frequency window of one order of magnitude to minimize the immersion time that could favor the possible Cassie to Wenzel transition at these reduced surface tensions. To collect the impedance measurements, the probe area (1 cm^2) is completely covered with a 16 ± 1 mm column of $LiClO_4$ (aq) and ethanol followed by agitation of the system to evacuate any large air pockets that may form at the interface of the film. The figure shows that the presence of ethanol results in three distinct magnitudes for the impedance that could be classified in two types of phase angle behaviors. In the presence of pure water (0%), the film exhibits the highest value of impedance as well as purely capacitive behavior ($\phi \sim -90°$). For concentrations of ethanol from 2-6%, the presence of ethanol results in a moderate reduction in impedance while the phase angle remains constant and close to $-90°$. Finally, for concentrations of ethanol of 8 and 10%, the impedance is one order of magnitude lower than that exhibited by the film in the SH state, and the phase angle shows the presence of a resistive component, indicating the diffusion of the liquid solution through the film. Table D.1 lists the capacitances exhibited by the film after

fitting the experimental data of Figure D.1 to the circuit model of a metal surface covered by a polymer film.[1]

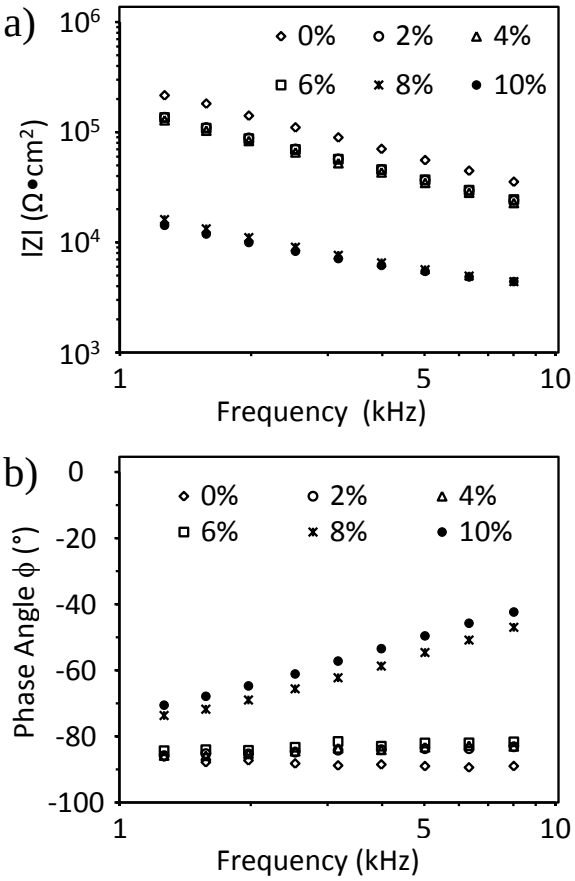

Figure D.1 Impedance spectra (a) and phase angle (b) of an initially SH film in contact with aqueous solutions containing ethanol (0 - 10% w/w) and $LiClO_4$ (0.05 M).

Table D.1 Capacitance values exhibited by a SH PM film in contact with ethanol-water solutions of various concentrations of ethanol. Calculated values resulted from fitting the impedance spectra to the circuit model of a metal surface covered by a polymer film.[1]

Ethanol concentration (%)	Capacitance (nF)
0	0.57
2 – 6%	0.91 ± 0.03
8 - 10%	7.95 ± 0.730

Results from Figure D.1 and Table D.1 indicate the capability of impedance measurements to detect wetting changes occurring at the solid-liquid interface. In the case of ethanol concentrations greater than 2%, we observe that the impedances of the film are lower than that exhibited at the SH state (0%), which suggests that at these conditions, the complete Cassie regime is no longer maintained. Results show that the impedances of the film as a function of frequency follow the circuit model of a metal surface covered by a polymer film[1] and exhibit characteristic reductions in their magnitudes as the concentration of ethanol increases (2-6% and 8-10%). From Table D.1, we also notice that the ratio of the inverse of capacitance at 0% to the average at the 2-6% range is 1.6, in agreement with the correction factor, ψ, that is applied to describe the effect of the associated air entrapment on the dielectric properties of the film (see Chapter V). This behavior suggests that, if at 0%, the film is initially in the Cassie state, then the film begins to transition into the Wenzel state at some concentration below 2% until reaching what could be a complete transition for concentrations from 2-6%. In the case of ethanol concentrations greater than 8%, further reduction in the impedance and appearance of a resistive component according to ϕ suggest that the liquid phase is not

only completely wetting the contours of the surface but also diffusing into the film. Experimental information of Figure D.1 shows that the differences in impedance at particular concentrations of ethanol could enable the identification of the Cassie and the Wenzel states. However, to distinctively identify these states, instead of collecting the complete spectrum, we monitor the impedance at a single frequency over a greater spectrum of concentrations, taking advantage of its in situ character and shorter acquisition time as compared to EIS to rapidly detect the onset of impedance change once the solution begins to displace the air interlayer.

References

(1) Tuberquia, J. C.; Nizamidin, N.; Jennings, G. K. *Langmuir* **2010**, *26*, 14039-14046.

APPENDIX E

MATHEMATICAL EXPRESSIONS FOR THE REAL AND THE IMAGINARY COMPONENTS OF THE IMPEDANCE VECTOR

To quantitatively validate the Cassie and the Wenzel state assignments for the impedance curve of the SH film, we compared the $1/C_{Helmholtz}$ predicted by the Helmholtz theory (Equation 1) with the $1/C_{Measured}$ that yields the impedances exhibited for both states at 1 kHz according to Figure 6.3a. We calculated the inverse of capacitance ($1/C_{Helmholtz}$) with Equation 5.10 (Table 6.1) using an average thickness of d_{film} = 2180 ± 180 nm and the dielectric constant (2.3) of PM. To estimate the $1/C_{Measured}$ that results in the Cassie and the Wenzel impedances shown in Figure 3a, we used the analytical description of the electrochemical system in terms of the circuit model of a metal surface covered by a polymer film.[1] In these calculations, we estimated the magnitude of the impedance based on the expressions for the real and the imaginary components of the vector[2]:

$$Z_{\mathrm{Re}} = R_{\Omega} + \frac{R_{film}}{1+(\omega C R_{film})^2} \qquad \text{(E.1)}$$

and

$$Z_{\mathrm{Im}} = \frac{\omega C R_{film}^2}{1+(\omega C R_{film})^2} \qquad \text{(E.2)}$$

where ω is the angular frequency, R_{Ω} is the resistance of the solution, and R_{film} is the resistance due to the interfacial air and polymer film. Due to the completely capacitive

character of both states, the values of R_{Ω} and R_{film} have no influence on the impedance magnitude at 1 kHz; thus, we used values for these parameters based on a complete impedance spectra ($R_{\Omega} = 30\ \Omega\bullet cm^2$ and $R_{film} > 5\times10^9\ \Omega\bullet cm^2$). Using these parameters as well as the average impedances for the Cassie and Wenzel states from Figure 6.3a, we calculated $1/C_{Measured}$ for both states using equations E.1 and E.2. Experimental results of $1/C$ in Table 6.1 show that the experimental estimations, $1/C_{Measured}$, agree with the theoretical predictions, $1/C_{Helmholtz}$, thus indicating that the quantitative as well as qualitative descriptions enable valid designation of both the Cassie and the Wenzel states.

References

(1) Tuberquia, J. C.; Nizamidin, N.; Jennings, G. K. *Langmuir* **2010**, *26*, 14039-14046.

(2) Bard, A.; Faulkner, L. *Electrochemical Methods*; 2nd ed.; Jhon Wiley and sons, 2001.